FORMING OF TAILOR-WELDED BLANKS

Dissertation

Presented in Partial Fulfillment of the Requirements for the Degree Doctorate of Philosophy in the Graduate School of the Ohio State University

by

Frederick I. Saunders, B.S., M.S.

* * * * *

The Ohio State University

1994

Dissertation Committee:

Robert H. Wagoner
Glenn S. Daehn
Peter M. Anderson

Approved by:

R H Wagoner

Adviser, Department of Materials Science and Engineering

Dedicated to the loving memory of my grandfather

Irvin James Bandelier

May 21st, 1901 - May 6th, 1994

ACKNOWLEDGMENT

I would like to deeply thank my adviser Professor Robert H. Wagoner for his technical guidance, direction, advice and opportunities to work with industry over my four years at Ohio State. I would also like to thank Dr. Glenn S. Daehn and Dr. Peter M. Anderson for providing technical advice throughout my stay at Ohio State and for being members of the examination committee. I would also specially thank Dr. Dajun Zhou for his superb guidance and patience in teaching me how to effectively use the finite element method. Also, I would like to thank the following for providing an excellent working atmosphere and plenty of technical support: Mike Miles, Yuji Hishida, Wei Wang, Hongyan Zhang, Dr. Yeong Sung Suh, Dr. Narasimhan Krishnaiyengar, Mark Stasik and Sriram Sadagopan. Bud Farrar, Gary Dodge and Lloyd Barnhardt are all gratefully acknowledged for their help with departmental equipment which made this project a whole lot easier.

Professor Taylan Altan is thanked for providing financial support of my research for the past four years. Also, the industrial partners are gratefully acknowledged for their assistance: Kumar Bhatt, Gary Neiheisel, Bob van Otteren, Tim Webber, Tom Stoughton and Peter Sun.

And, of course, I cannot forget the people who listened to me complain and whine throughout this entire project and provided unbelievable support: my parents, Mike & Amy Breslin, my second family at King Avenue United Methodist and the Lord Jesus Christ, who made all of this possible.

VITA

March 18th, 1968.....Born - Jackson, Michigan

May, 1990.....B.S. Metallurgical Engineering
Michigan Technological University

December, 1993.....M.S. Materials Science and Engineering
The Ohio State University

September, 1990 - present.....Graduate Research Associate
Dept. of Materials Science and Engineering, The Ohio State University

PUBLICATIONS

F. I. Saunders and R. H. Wagoner, *Finite Element Modeling of a New Formability Test*, Computer Applications in Shaping and Forming of Materials, eds. M. Demeri, Symposium at 1993 TMS Annual Meeting, Denver, Co.

F. I. Saunders, M. P. Miles, J. L. Siles and R. H. Wagoner, *A Better Sheet Formability Test*, MetalForming, Nov. 1993, pp. 31-35

FIELDS OF STUDY

Major Field: Materials Science and Engineering

Studies in Mechanical Behavior of Materials

Drs. P. M. Anderson, G. S. Daehn and R. H. Wagoner

Studies in Physical Metallurgy

Drs. S. Dregia, H. L. Fraser, and P. G. Shewmon

Studies in Chemical Metallurgy

Drs. S. Akbar, R. A. Rapp, and G. R. St. Pierre

Studies in Electron Microscopy and X-Ray Diffraction

Dr. W. A. T. Clark

Studies in Solid State Physics

Dr. R. Sooryakumar

TABLE OF CONTENTS

LIST OF TABLES

LIST OF FIGURES

CHAPTER I

INTRODUCTION

In current automotive stamping technology, there are two basic paths that can be followed to arrive at the final panel [1]. The first method is part disintegration or part separation. In this technique, each different section of the blank is stamped separately and then spot welded together in the shape of the final part. This method has numerous advantages such as the ability to select the specific properties, i.e. the strength, thickness, corrosion resistance, etc. of each area of the blank. This method also gives a higher yield ratio of material used [1]. However, this method does have its share of disadvantages. The major problem is the large number of different forming operations that is required for the disintegration method, which translates to high tooling costs. Also, assembly costs would increase (more joining required) and there is a possibility of fittability problems between the different stampings [2]. The other possible method is the integration method. In the integration method, the part is stamped out of a single blank. This reduces the number of tools needed, the assembly cost, and eliminates any fittibility problem. However, the design engineer is forced to work with same grade, thickness, and corrosion resistance throughout the entire part. Since the most demanding of all these conditions must be satisfied for the entire blank, this would increase the cost and weight of the part significantly.

A solution to the problems listed above is the utilization of tailor-welded blanks. A tailor-welded blank is a blank that is comprised of two separate pieces of sheet metal that has been welded together previous to stamping. Tailor-welded blanks allow the welding of the different grades, different thickness or different corrosion coatings together in order give the properties needed in different areas, without increasing the number of tools needed to form the part and eliminating the fittability concerns. They also allow a high degree of flexibility in designing parts and large blanks can be formed from much smaller sheets [3]. In fact, it would allow forming of parts larger than the original coil width.

With the changing attitude of society toward the environment, the use of laser welded blanks could be very beneficial to the automotive industry. Industries around the world are being forced to meet more stringent requirements in order to meet the growing concern of preserving the environment. This includes reducing scrap from manufacturing and making their products more energy efficient. The automotive industry is not immune to this world-wide revolution. However, the need to reduce scrap is not only an environmental issue. Increasing the amount of scrap reclamation could increase profits significantly. It is estimated that 30 to 50 % of the sheet metal purchased by certain stamping plants ends up as waste [4], primarily the result of large openings in the stamping (i.e. door windows).

Along with the reduction of scrap, the automotive industry is subject to more and more stringent government regulation for fuel efficiency. There is currently a large interest in developing lightweight alloys that can be used in an automobile to replace heavier steel parts, resulting in weight reductions of the vehicle without sacrificing strength. Metallic materials such as aluminum and

magnesium, carbon-carbon composites as well as a number of novel metallic-ceramic composites are all under investigation in terms of viability and practicality for use in a high production automobile.

This is where the advantage of the tailor-welded blanks comes into play. Using tailor-welded blanks, the scrap rate would decrease. In an example cited by Toyota [1], the material yield ratio for an integrated part was 40%, while using the separation technique, which would be about the same as a tailor-welded blank, the yield ratio is closer to 65%. Also, tailor-welded blank technology allows utilization of scrap by welding scrap pieces together that can be used later.

The use of tailor-welded blanks would reduce the weight of the car. Having the ability to selectively place different thickness of material would result in weight reductions. An example of this used in production is the door inner panel. The only strength requirements on a door inner is in the region where the hinges attach to the panel. Previous to welded blanks, the entire door inner must be made of the same thickness that is required for the strength requirement of the hinge area, resulting in adding unnecessary mass to the vehicle. Alternately, additional brackets and shifters could be added after forming, thus increasing costs and perhaps reducing consistency. A tailor-welded blank requires only the front fraction that requires the strength to be of the heavier gage, while the remainder of the panel would be of a lesser thickness.

The welding technology has advanced to the level that joining two pieces of sheet steel is not a serious problem. In fact, the weld material is usually stronger than the base material. There are three different welding processes that are being considered for tailor-welded blanks; laser, mash seam and induction. Traditionally, laser welding was considered the best process for tailor-welded

blanks. However, mash seam welding is also considered because according to some controversial statistics, it has about 30% less processing cost than the laser. More recently, induction welding has emerged as yet another competing process. Unfortunately, there is no published data comparing the formability of each welding process. All three types are being used in production in Europe, however [6].

This leads into the main scope and objective of this research. The welding technology for tailor-welded blanks is well established. What is not understood is the forming characteristics of the tailor-welded blank. The problem is the prediction of how the location of welds will influence the formability and if there is a significant difference in the formability between the different types of welds. In this project we measured the formability of different types of welds using laboratory sheet forming tests. Through this testing we were able to compare the formability of the different weld types, as well as analyze the different testing methods. Further investigation included testing using the scale die fender (a scaled down geometry that represents an automotive front fender) that is used with the *Hydraulic Forming Simulator* at the Ohio State University. Using this geometry we were able to study how the tailor-welded blank performs in an actual forming operation. With this geometry we investigated not only the influence of the different weld types, but the weld position and orientation, friction and other processing parameters such as boundary forces. The third phase of this project uses the Finite Element Modeling (FEM) to see if a model can be developed to predict the actual forming behavior of a tailor-welded blank. The investigation included modeling the *OSU Formability Test*, the Limiting Dome Height Test (LDH) and the Scale Fender Die. It has been observed that the movement of the weld line has a strong influence on formability, so the main

focus of the modeling was to try to predict this phenomena and compare it to the experimental results.

CHAPTER II

LITERATURE REVIEW

1. Tailor-welded Blanks

There is very little published research in the area of forming tailor-welded blanks. From the author's experience, the majority of the studies in this area have been carried out by the industry and the results have been kept private. The majority of the articles published about tailor-welded blanks have been mostly information discussing general characteristics of tailor-welded blanks, while there has been a scattered few that are more technically related.

1.1 Welding Development for Tailor-welded Blanks

1.1.1 Laser Welding

As described by Baysore [7], laser welding is a process where a monochromatic light beam is focused on a butt seam of two sheets. The listed advantages of tailor-welded blanks are there is no need for filler material, the weld bead is narrow and the heat input is low. Disadvantages of laser welding cited by Baysore [7] are the tight tolerances on edge preparation and the equipment is much more sophisticated than the more conventional welding methods (i.e. resistance).

Radylmayr and Szinyur [8] investigated many aspects of laser welded blanks, including the laser welding process itself and what factors have the strongest influence on the resulting welds. Four welding parameters were investigated; the influence of gap width, process gases, beam position and the surface condition of the sheet.

To investigate the influence of gap width, welds were made with a gap varying from 0 mm to 0.14 mm with varying weld speed. A small gap with a low weld speed resulted in a weld bead that sagged, while a small gap at a high speed resulted in incomplete penetration of the laser beam. A large gap always produced excessive concavity of the weld. For a CO_2 laser with a 200 mm focal length and 2.6 kW power, the optimum speed was 3-4 m/min with a gap of about 0.10 to 0.12 mm. However, these variables are a strong function of the focal length and power.

It is believed that the best process gases to use are high purity argon and helium. A combination of 75% Ar/25% He was found to give nearly the same quality weld as the pure gases. As the helium percentage increased, the quality of weld decreased.

The alignment of the beam was offset by increments of 0.05 mm up to 0.4 mm, and it was found that the weld is adequate for misalignments up to 0.2 mm.

A number of blanks with different coatings were welded (oil, metallic coating, phosphates). A slight increase in porosity was observed, but most likely the amount of porosity was insignificant in terms of influencing the strength of the weld.

Yang et. al. [3] addressed the fact that thermal behavior of the laser weld processing will have a strong influence on the microstructure of the weld, and hence the mechanical properties. The overall objective of their work was to

develop a simplified finite element calculation to predict the thermal cycles in laser blank welding. They did not do experimental verification of the thermal cycling behavior of laser welding of a thin sheet; instead the model was verified using measured thermal cycles of much larger laser welds and the weld and heat affected zone size of the thin blanks. The results found Yang et al.'s simulation to match experimental weld zone sizes, cooling and heating rates in a general sense, but their simplified calculation did induce some error. In general, they found the heating and cooling rates in laser blank welding to be very rapid. It was noted that this rapid rate would probably not influence the structure of low carbon steels, but would have a larger effect on the resulting weld structure in high strength low alloy and other sophisticated steels.

1.1.2 Mash Seam Welding

Baysore [7] describes mash seam welding as a welding process where two copper wheel electrodes are rolled over two overlapping sheets [7]. The sheets are forced together with a 5 kN load and a current of 20 kA is passed between the electrodes. The pressure and the resistance heating results in a bond at the overlap. For uncoated materials, weld speeds of 300-600 in/min can be achieved. However, coated materials need to be welded at much lower speeds [7] because of variations in coating thickness could cause variation in weld quality. A major advantage of mash seam welding over laser welding is the tolerances on edge preparations are not as tight as those required for laser welding.

Because a mash seam weld can be up to 1.5 times thicker than the base materials, a process referred to as planishing may be required for mash seam welds. Planishing is a process where the weld is reduced in thickness by running the weld through two wheels with high pressure after the welding. This is done because U.S. automotive manufacturers wish to see no more than a 10% increase

in thickness at the weld bead [7]. European automakers are less concerned with this increase in thickness, which means planishing is not needed. This in turn makes the mash seam welding process much cheaper and hence much more attractive to Europeans.

Schmidt [9] also listed a number of advantages of the mash seam process for tailor-welded blanks over other processes such as laser, plasma and TIG welding. Along with the advantage of low tolerance on edge straightness, quality and parallelism, mash seam welding does not require extensive alignment of equipment. Also, there is no undercut in a mash seam weld, which decreases the strength of the weld region. The weld process itself does not produce harmful vapors as does other processes, and the capital investment is much smaller than for other welding processes [9]. The disadvantage mentioned is that a mash seam weld should not be used in applications where the weld is visible, because of its size and shape.

Van Otteren et. al. [10] observed that the planished mash seam weld was too hard and brittle to withstand further processing. Therefore, Newcor Bay City developed a "hot planishing" process as a stress relieving operation to make the planished weld more useful. They investigated hot planishing of welds with two objectives in mind: to verify and quantify any reduction in weld zone hardness from the hot planishing as opposed to the cold planishing, and to develop hardness profiles throughout mash seam welds, characterizing properties at different positions throughout the weld [10]. Three material combinations were welded: 0.8 mm cold rolled steel (CRS) to 0.8 mm CRS, 1.0 mm galvanized to 1.0 mm bare CRS, and 0.8 mm to 1.8 mm galvanized CRS. Hardness profiles were taken from different sections at different locations along the length of the weld, as well as at the top, middle, and bottom of the weld. Van Otteren et. al. found

that hardness profiles were consistent at the different locations along the weld line as well as different positions in the cross section of the weld. The peak hardness for the hot planished weld was much lower than the cold planished, and the peak hardness for the as welded was about the same as the hot planished.

1.2 Forming of Tailor-welded Blanks

The most published literature in the forming of tailor-welded blanks is from Toyota Motor Company [1,11,12]. In these papers, the Toyota engineers studied the forming behavior of laser welded blanks at all levels, from small scale laboratory tests to full scale experiments supported by finite element analysis. The chose laser welding because they identified the following characteristics of the laser weld as necessary for the actual forming [1]:

1.) Thermal strain on the weld bead should be low.

2.) Characteristics of the weld bead should not change much after welding.

3.) The weld bead should be narrow.

4.) Welding productivity should be high.

Based on these conditions, CO_2 laser welding was chosen as the welding process that fit these conditions [1], although there was a change in hardness and microstructure in the weld bead region.

In their initial study conducted by Azuma et. al. [11], they investigated three fundamental forming operations: projection, stretch flangeability and deep drawability. For projection, they used the Erichsen [13] punch stretch test with a variety of blank widths and the weld oriented both parallel and normal to the major stretching direction. It was found that the presence of the weld parallel to the stretch axis reduced the failure height 30% of the projection height of the base

material, regardless of base material combinations. The crack always propagated in the weld normal to the stretching direction. Therefore, it was assumed that the limited ductility of the weld bead was the cause of the failure. When the weld was oriented normal to the stretching direction, the mere presence of the weld only decreased the projection height approximately 10%, but the height decreased as a function of strain ratio. At strength ratios greater than 1.5 the failure height is invariant to strength ratio, because the plastic strain in the stronger substrate is zero for ratios greater that 1.5.

The strain in the weld region was measured for forming a blank width with the weld parallel to the major stretch axis. They found the strain state in the weld region varied as a function of blank width. It is assumed in other work [2] that the deformation is all uniaxial tension because the weld is much stronger than the base. However, the results in this study prove otherwise.

The hole expansion test was used to measure the stretch flangebility of the welded blank. It was found that the presence of the weld reduced the extension flange ratio by 25 - 30% because the stronger weld bead resists the shrinking deformation. It was also observed that using substrates with different strengths reduced the extension flange ratio further.

For the deep drawing analysis, the Swift Cup test was used. Specimens were used to meet drawing ratios of 1.8 to 2.2. Blankholder forces were varied between 1000 and 10000 kg to determine the Limiting Drawing Ratio (LDR). It was found that LDR was not significantly affected by the presence of the weld. For same substrates, the LDR did not change at all, while the LDR was the average of the two base substrates when different substrates were used. It was observed that the weld moved significantly toward the stronger substrate, and the weld movement was more severe with increasing LDR.

In practical forming, a problem area was in the area of stretch flanging at a corner. Therefore, they designed a model stretch flange die similar to that used in production. The weld line was placed at different distances away from the corner, and the deformation height at each position was compared to the deformation height of the base material. The critical position of the weld was determined to be 10 mm away from the corner. Therefore Toyota had developed a design criteria for locating weld lines in a stretch flange operation.

Although a large amount of experimental data was gathered, it was clear that it was impossible to gather enough data to be able to predict the forming behavior of all forming operations. Therefore, Nakagawa et. al. [1] and Iwata et. al. [12] developed a finite element approach that would predict a larger spectrum of forming operations. They used an elastic-plastic commercial code "JNIKE3D" and achieved high accuracy by accounting for planar anisotropy by implementing Gotoh's biquadratic yield function [14] and considering the initial pressure distribution on the blankholder. The pressure distribution on the blankholder was determined by stamping a blank with a pressure detecting film on the binder to determine the variation in force as a result of random variation in thickness in the tools. The pressure distribution was represented in the model as a variation in position on the blankholder surface.

The part modeled was the experimental stretch flanging die that was developed and originally presented by Azuma et. al. [11]. The blank materials were modeled using shell elements, and the weld line was modeled using beam elements. The plastic behavior of the weld line was assumed to be at a flow stress 1.5 times higher than that of the strongest base material. The JNIKE3D simulated strains had the same characteristics as the experimentally measured strains for a blank with a strength ratio of 1.6.

The experimental failure height occurred in two different positions depending on the weld line location; if the weld line was closer to the corner, there was great strain localization in the weaker material next to the weld in the weaker material. When the weld was further from the corner, the failure occurred in the corner of the stretch flange, just as in the base material. Both of these failures were predicted by the finite element model.

Toyota also analyzed shrink flanging on an experimental shrink flange die. For welded blanks of the same base material, there was no influence of weld position at all on forming height. For combinations of different thickness, it was found the maximum failure height was always higher than that of the higher strength material. An optimum position actually resulted in a failure height greater than that of either base materials. However, wrinkling was observed in the weaker material as it is being pulled by the stronger material. Preliminary finite element modeling of this shrink flange geometry found the stronger material pulls the weaker material on the flange surface, resulting in locally increased strain in the weaker material.

In work done by other groups, Shi et. al. [2] evaluated the mechanical properties of the welds and addressed some basic formability issues of tailor-welded blanks. In this study, they investigated both laser welded and mash seam welded blanks. Results of laser and mash seam welds tested in uniaxial tension with standard and subsize tensile specimens found that the yield stress of the subsize ones was significantly higher and the n value and total elongations were less than the standard specimens. It was assumed that subsized tensile specimens were better for testing the mechanical behavior of the weld than the full size specimens because the deformation region had a smaller fraction of base material.

Shi et. al. assumed that the plastic deformation was all in the direction of weld. The hardness of the weld is much higher, so all the deformation in transverse loading is by the base materials, and there would be no deformation in the weld.

The Marciniak Cup Test was used for punch stretch testing. The laser weld had a limit strain of about 14% while the mash seam weld had a limit strain of 20%, and these limit strains were invariant to the strain state of the base materials.

In order to improve the formability of a tailor-welded blank, a number of guidelines were proposed. First, it was mentioned that weld line placement would improve formability as much or more than changing welding parameters. Since the weld material itself has a significantly lower ductility than the base material, the weld should be oriented normal to the major stretch axis. However, in the case when the blank contains different thickness or different strength base materials joined together, the stronger material will not deform, forcing the weld to move in the direction of the stronger material, resulting in high strains in the weaker material. This high strain localization could be reduced by either reducing the strength/thickness ratio or by reducing the boundary force pulling in that direction.

Based on these guidelines, the weld on a 0.8 mm/1.8 mm AKDQ blank for the LDH test was offset by 9.5 mm to account for the weld movement, which resulted in a significant improvement in the overall formability of the blank. This same guideline was used for forming a door inner using a mash seam blank. In forming the original part, the blank tore parallel to the weld, next to the weld, in the weaker material as a result of weld movement. The drawbeads were opened up to allow material to flow into the die, which resulted in a good part.

However, this produced unacceptable wrinkling. Further modifications were made in the tool that resulted in less wrinkling and still lowered the boundary forces. These conditions successfully suppressed weld movement and resulted in a good part.

Radlymayr and Szinyur [8] performed the Nakazima Test (100 mm hemispherical dome stretch test) on a number of different combinations of laser welded blanks in the plane strain conditions. The weld line was located both horizontal and vertical to the major stretch axis in these tests. Generally, it was found that when two materials of the same grade were welded together, the weld always decreased the failure height. On the other hand, when a drawing quality steel was welded to a high strength steel, the failure height was generally between the failure height of the high strength steel and the drawing quality steel. The welding speed had a large effect on the formability of the welds. Lower weld speeds corresponded to a lower failure height.

Radlymayr and Szinyur also tested the welded sheets in uniaixial tension. In testing standard tensile bars, it was found that the presence of the weld increased the strength over that of the base materials. They also measured the exact mechanical properties of the laser weld by making tensile specimens with 1 mm wide deformation regions by wire eroding the base material away. The yield strength of the weld bead was found to be between 450 and 570 MPa, while the UTS was between 590 and 640 MPa. The total elongation was found to be between 4 and 7.5 %.

Wang et. al. [15] investigated the crashworthiness of tailor-welded blanks, but as a side issue investigated is the mechanical properties inside the weld bead. Wang et. al. tested subsized specimens of both laser and mash seam welds that joined a 1.0 mm high strength steel to a 1.8 mm mild CRS. The stress at a given

strain in the weld bead was found by using a simple force balance for the test specimen, and knowing the tensile properties of the base materials surrounding the weld. They found the laser welds were much stronger than the base materials, while the mash seam weld had identical properties to the high strength material. Galvanized coating adversely affected the laser weld strength, while it slightly enhanced the strength of the mash seam weld. The addition of a high strength steel increased the strength of both types of welds. It was also found that welding two materials of different thickness together resulted in a weaker weld than a weld of similar material of the same thickness.

1.3 Applications of Tailor-welded Blanks

Baysore [7] discussed advantages and applications of tailor-welded blanks. Since the advantages of tailor-welded blanks is outlined in the introduction, in this section we will focus on the applications.

The first application discussed by Baysore is a motor compartment rail. The 1992 Cadillac motor compartment rail was made using a tailor-welded blank. It was a 0.8 mm blank laser welded to a 2.0 mm blank. This resulted in a 7.6 lbs weight savings in purchased steel and net 2.9 lb. weight savings to the entire vehicle. Mash seam welded rails that run the full length of the car are being used by VW in Europe [7]. Because the mash seam welds are much stiffer than spot welds, there is a significant improvement in crash rating, resulting in a much safer car.

Another common application that Baysore mentioned is the door inner. A big advantage of this application is part reduction. Previous to tailor-welded blank technology, there were reinforcements for door hinges and mirrors that were required. Now, the door inner is made of 1.8 mm gage blank welded to 0.8

mm material. The 1.8 mm material provides more stiffness, hence eliminating the need for the reinforcements. This results in a reduction in processing costs.

By using a tailor-welded body side ring, Toyota Lexus was able to improve the aesthetics of their product. Previously, the spot welds were visible when the door was open. Now, using a tailor-welded blank, the flush laser weld is not as visible as a spot weld. Therefore, the laser welded side ring was not only stiffer, eliminated reinforcements, provided weight savings and improved safety, but it was also aesthetically pleasing.

Wang et. al. [15] addressed the crashworthiness of a tailor-welded blank. They compared the laser and mash seam welded sheets to a straight spot weld. They used a statistical design of experiments in an attempt to optimize the important parameters to produce the maximum resistance to impact loading. The parameters that were investigated were material yield strength, thickness, surface conditions and welding technologies. The testing method used was impact testing; samples were tested in both the axial and bending condition. In these impact tests, the maximum crush energy, maximum crush load, maximum crush distance and average crush load were all measured. The results showed that the laser and mash seam welded blanks all performed satisfactorily. In the four variables measured in the testing, only the average crush force was different between the two, with the mash seam welded blanks having a higher force. It was found that the spot welded blanks performed reasonably well, but the spot welds did periodically fail, while there was never a failure in the mash seam or the laser welds. It was also found that the thickness of the blank showed significant increase in energy absorption, while increase in yield strength did not. Also, the galvanized coating had very little effect on the crashworthiness performance of the test.

The fatigue and corrosion properties of a laser welded blank were studied by Radlymayr and Szinyur [8]. The fatigue results showed very little difference between the fatigue strength of the base materials and the tailor-welded blanks. In corrosion testing, the laser weld performed very well for a number of different surface conditions (uncoated, metallic coated, painted, phosphate) and in some conditions performed better than the base materials. The presence of a laser weld seems to have no detrimental effects on the corrosion or fatigue properties of the material.

2. Formability Testing

Two common punch stretching tests are the Erichsen/Olsen Cup Test [13] and the Limiting Dome Height Test [16,17]. Through independent studies, the Limiting Dome Height (LDH) test was shown to show better correlation to press performance than the Olsen Cup Test [18], so it gained popularity in the late 1970's and the early 1980's. However, the LDH test suffered from a lack of reproducibility, both day-to-day and lab-to-lab [19,20], for a number of reasons cited in other work [21]. A long, drawn out procedure was developed to try to improve the performance of the LDH [20], but the scatter was still unacceptable. Therefore, the LDH did show some promise because of observed press performance, but was plagued with poor reproducibility and long testing times. For these reasons the LDH's popularity throughout industry decreased rapidly.

In order to improve on the current LDH test, the *OSU Formability Test* was proposed [22]. The design of the *OSU Formability Test* was based on the LDH geometry in order to retain its press performance. At the same time, the new test would hopefully eliminate some of the problems of the LDH, such as irreproducibility and long testing times. The *OSU Formability Test* was designed to promote stable plane-strain conditions in the failure region for various

materials and processing conditions. The plane strain condition is the most important to test because it is estimated that nearly 85% of failures in automotive sheet stampings occur near this strain state [18].

Originally three cylindrical type geometries were proposed for the new test. Initial studies showed that a flat-elliptical type geometry produced the strain state at failure closest to plane strain, so this geometry was used for verification of the new test. Preliminary experimental work [22,23] has shown scatter on the data of the new test to be about half, on average, of the Limiting Dome Height test and about 5 to 10 times faster to perform. Also of importance was the correlation of the data from the *OSU Formability Test* to the final punch height of the LDH test [22]. Because of this correlation, the data generated from the new test can be related back to databases based on LDH data. Also, the strain state at failure has been near plane-strain (experimental minor strain no greater than 2.5%) and has exhibited a strain path much more proportional than that of the LDH test [22,23].

Even with good preliminary results, it is felt that the *OSU Formability Test* could be improved by optimization of the tools. Optimization of the new test geometry provided a geometry that produced plane-strain behavior for a broad range of material and processing conditions that affect the strain state in the unsupported region. Since it is impossible to independently vary some material properties in experimental studies, computational techniques were employed. The finite element method (FEM) is a technique that is popular for analyzing sheet forming operations, and was ideal for this problem. The FEM model was used to determine the influence of material and processing parameters on the performance of the test.

Saunders and Wagoner [24] performed extensive FEM analysis of the three originally proposed geometries for the *OSU Formability Test.* Through this modeling it was found that the flat-elliptical punch had the strain state in the failure region closest to plane strain which correlated to the experimental results. It was also found that the strain state in the failure region was very sensitive to the material and processing parameters. After an extensive sensitivity analysis, Hill's stress exponent M, the normal anisotropy parameter r and coefficient of friction were the three variables that were found to have the strongest influence on the strain state.

Based on these results, Suh and Wagoner [25] proposed to optimize the OSU Test geometry such that the test would feature a stable plane strain state regardless of material properties or processing conditions. In order to assume the worst possible conditions for plane strain, simulations we run with the coefficient of friction equal to 0.15, Hill's stress exponent equal to 2.0, and the normal anisotropy parameter equal to 2.0. The simulations were carried out with SHEET-3 [27], an in house OSU code that features membrane formulation. The punch shape and radius, the die radius, the blank width and the gap between the tools were varied systematically until a stable plane strain state was established. The geometry was then modeled using solid elements with the ABAQUS commercial code [26] to check for any influence of bending the sheet on the failure mode. The optimum geometry was found to be a cylindrical punch with a radius of 12.7 mm, die radius of 9.5 mm, and a gap size of 2 mm.

3. 3-D FEM at The Ohio State University (SHEET-3)

SHEET-3 [27] is a three dimensional finite element code developed at The Ohio State University and is optimized for sheet forming operations. SHEET-3 features triangular elements that are used with a membrane approximation, and

a rate sensitive anisotropic hardening law based on Hill's 1979 criterion. The simplifying assumptions (membrane approximation, rigid plastic) were implemented in order to reduce the computational time. Initially, the program was used to simulate simple geometries such as hemispherical and square punch stretching [27]. Later, Knibloe and Wagoner [28] used SHEET-3 to simulate hemispherical punch stretching and compared the results to experimental strains. SHEET-3 showed a reasonable comparison to the experimental strains, and found the predicted strain distribution to be heavily dependent upon the friction coefficient and Hill's M value. In this study, it was observed that using the Hill's M value calculated from experimental plane strain tensile tests required unrealistic friction conditions for agreement with experiment. Wang and Wagoner [29] simulated the square punch forming using SHEET-3 for both fully clamped sheets and strips. The FEM simulations were reasonable when the radius of thickness to curvature ratio, r/t, was greater that 5 at the punch corner, which is the proposed limit for the accuracy of membrane theory [30]. However, as the r/t ratio decreased, the deviation between simulation and experiment increased. Therefore, the membrane approximation is reliable for a large number of forming operations that feature a gentle radius of curvature of the tools relative to sheet thickness.

For a description of the tool surface, smooth surfaces and smooth spatial derivatives are required. This is very difficult to accomplish, and many times these descriptions can be computationally inefficient [31]. For tool surface descriptions, SHEET-3 was implemented with a mesh-normal formulation, where the spatial derivatives are dependent upon the mesh and not the tool surface [31]. This method was found to be computationally efficient, with only a 10% penalty compared to an analytical surface description.

Up to this point, only stretch forming operations could be simulated using SHEET-3. There were two major developments in SHEET-3 which made the modeling of stretch-draw conditions possible. First was the development of the **C**onsistent **F**ull **S**et (CFS) algorithm [32]. Previously, the formulation of SHEET-3 required first solving the material equilibrium problem, and then going back and solving the contact condition. This required many iterations and made convergence very difficult. The CFS algorithm put both the material equilibrium and the contact condition into the same solution step, hence solving both at the same time. This resulted in greater CPU efficiency and better numerical stability. With the old formulation, deep drawing was impossible. With the CFS method, 2-D drawing problems could now be modeled [32].

A further improvement of the code was the N-CFS algorithm [33]. The original CFS algorithm minimized contact error in the z (vertical) direction only. This was sufficient for areas of gentle curvature, but when a vertical die wall in a deep draw was encountered, the nodes in the unsupported region had no tool to come into contact with. Therefore, SHEET-3 was modified such that the node would project to the surface along the mesh normal direction. This made convergence for draw conditions even better, especially for vertical die walls.

With the advances made in the SHEET-3 program, it was able to model very complex geometries. Recently, the code was used in two international benchmarks. The first was the 1991 VDI benchmark [34], which featured the forming of an Audi deck lid. This was real part for an Audi automobile, and featured a complex tool description and stretch-draw conditions. SHEET-3 was able to form the part to a full 48 mm, and the strain distributions were in reasonable agreement with other programs entered in the benchmark.

In 1993, another international benchmark was held in conjunction with Numisheet '96 [35]. There were three benchmarks in this conference; deep drawing of a square cup, drawing of a u-channel to measure springback, and forming of an actual front fender from a Nissan automobile. SHEET-3 successfully modeled the square cup and the front fender geometries, while the u-channel was not done because springback could not be measured with SHEET-3's rigid plastic formulation. The results of the front fender simulation did not match the experimental results very well, but it was determined at the conference the lack of knowledge of the experimental boundary conditions induced a lot of error.

The key point from the VDI and Numisheet benchmarks is that FEM of sheet metal forming has advanced to the point where real, complex geometries can be modeled by a number of programs worldwide. Therefore, as we look to develop a predictive ability for the forming of tailor-welded blanks using FEM, it is noted that the ability to model most any part already exists, and the effort should not be in trying new programs or new geometries. Instead, the focus should be on what variables and parameters make a tailor-welded blank different from a homogeneous blank, and which of these variables have a strong influence on the behavior.

CHAPTER III

MATERIALS AND METHODS

1. Blank Combinations

In this study, the combination of base materials for the welded blanks was a 1.8 mm AKDQ material joined to a 2.14 mm high strength low alloy steel (HSLA) and a 0.8 mm AKDQ joined to a 1.8 mm AKDQ. This combination was chosen specifically because it is a proposed combination for an engine compartment rail and the 0.8/1.8 combination was chosen because it is a common combination for the door inner.

2. Weld Processes

As mentioned before, there were two major welding processes in this study: laser and mash seam. We are comparing two types of laser welding processes, the CO_2 gas and solid state Nd:YAG laser. The CO_2 laser welding was performed by Armco Research and Technology [36] and the Nd:YAG laser welding was performed by Hobart Laser Products [37]. For mash seam, we investigated a basic mash seam weld, as well as a mash seam weld that has been planished and hot planished, which will be described in greater detail in section 2.2. The mash seam welding was performed by Newcor Bay City [38]. The laser has been considered the superior welding process because of the lower heat input into the material, but there is no quantitative data comparing the two in terms of formability. The mash seam process has been reported to be

approximately 30% less expensive than the laser process [5], which makes it attractive to the automotive industry.

2.1 CO_2 and Solid State (Nd:YAG) Laser Welding

Since we are not studying the welding of the blanks in this investigation, much of the detail about the physics of lasers will be omitted, as they can be found in great detail in other published literature relating more to this topic. A laser (**L**ight **A**mplification by **S**timulated **E**mission of **R**adiation) is a beam of light that is monochromatic; all radiation has the same wavelength, and it is in phase in space and time. These are generated by exciting atoms so they emit radiation. The atoms can be excited by placing high voltage in a gas (CO_2, for example) or by exposing a crystal (Nd:YAG) to a flash discharge, and the reflected light in the crystal would excite atoms that would emit radiation.

The monochromatic beam can be focused to a point, resulting in a high energy per unit area. If this is focused on steel, it would raise the temperature of the steel to above the melting point. This is the basis for laser welding. For laser welding, the edges of two sheets are butted together. The laser is focused on the joint, resulting in a pool of molten metal at the interface. When the laser moves away from the point, the material solidifies quickly, resulting in solid joint. It is excellent for welding because of the small heat affected area, but it can be difficult to perform because of the tight tolerances on the edge conditions.

The CO_2 lasers can generate much more power than the solid state laser. However, since in tailor blank welding the thickest material that will be encountered is approximately 2.5 mm, either laser should be acceptable.

The welding parameters for the CO_2 and the solid state laser welding used in this study are shown in Table 1.

2.2 Resistance Mash Seam Welding

Mash seam welding is based on the same principles as spot welding. The two sheets to be welded are lapped over. The overlap is passed through two electrically charged rotating wheels. This passes a current through the material to be welded, and the resistance of the material heats the material at the interface into a liquid zone. When the liquid zone solidifies, the bond is created. The difference between a resistance seam weld and a resistance mash seam weld is that in a mash seam weld the material at the weld is "mashed", or reduced in thickness, while in a resistance seam weld there is no significant reduction in thickness. Even so, the mash seam weld is still usually about 1.4 times thicker than the base material, which could cause problems in some applications. Therefore, the weld be can be planished, which is simply running the welded joint through two rollers after the welding process that flattens the weld. This reduces the thickness of the weld sufficiently, but induces cold work in the weld, which destroys the tensile ductility of the weld bead. In response to this problem, Newcor Bay City developed a process called 'hot planishing'. Hot planishing is a heat treatment of the weld zone after planishing, in an attempt to reduce the cold work and recover the tensile ductility.

3. Base Materials

As mentioned before, the three base materials used in this study are a 0.8 mm AKDQ, 1.8 mm AKDQ steel and a 2.14 mm HSLA steel. Each material was provided by the National Steel Product Application Center [39]. Both materials have a hot dipped galvanized zinc coating. The chemical compositions and

Table 1. Welding parameters for CO_2 and solid state laser [36].

Combination	Power (Watts)	Speed (m/min)	Process Gas	Lens at focus (mm)
AK0.8/AK1.8	2000	5	He @ 35 SCFH	125
AK1.8/HS2.1	2000	2.5	He @ 35 SCFH	125

Table 2. Chemical Compositions of Base Materials

Material	C	Mn	P	S	Si	Cu	Ni	Cr	Mo	Sn	Al
0.8 AKDQ	0.031	0.22	0.008	0.018	0.005	0.015	0.010	0.036	0.005	0.005	0.034
1.8 AKDQ	0.029	0.24	0.009	0.015	0.005	0.013	0.010	0.024	0.004	0.005	0.067
2.1 HSLA	0.06	0.40	0.010	0.007	0.017	0.012	0.010	0.035	0.008	0.007	0.067

Table 3. Mechanical Properties of Base Materials Provided by National Steel [39]

Material	Yield Strength (ksi)	Tensile Strength (ksi)	Total Elong. (%)	YP Elong (%)	n Value	Δr	$\bar{r}$
0.8 AKDQ	23.0	43.9	44.4	0.0	0.219	0.565	1.70
1.8 AKDQ	25.1	42.2	44.4	0.0	0.201	0.279	1.34
2.1 HSLA	60.0	70.1	27.5	4.9	0.164	0.405	1.45

mechanical properties of each alloy as provided by National Steel are listed in Tables 2 and 3, respectively. Uniaxial tensile tests were run on the base materials at the Ohio State University to determine the constitutive laws that govern the hardening behavior of the material. This procedure and results are discussed in more detail in Chapter 5.

4. Punch Stretch Sheet Formability Testing

4.1 The *OSU Formability Test* vs. Limiting Dome Height Test

In these tests, we measured the punch height at which failure occurs in the plane strain state, which is strain state that produces the worst formability. The *OSU Formability Test* (Figure 1) was designed to ensure a stable plane strain deformation independent of blank width and friction [22], while the LDH test is dependent upon both blank size and punch conditions. The comparison and contrast between the two tests has been covered previously in detail [22] and will not be discussed further here. Figures 2 and 3 show the tooling for the optimized OSU and LDH tests.

For studying the formability of the weld, the optimized *OSU Formability Test* was used. As discussed previously [25], the OSU Test was redesigned to provide a stable plane strain state that was invariant to material anisotropy parameters and friction conditions. Therefore, it would provide a better plane strain condition than the original geometry. Also, the optimized geometry was designed to test heavier gage blanks. The original test only featured a die radius of 6.35 mm, which would result in a ratio of the tool radius (6.35 mm) to the deforming workpiece (2.1 mm) of 3, which would possibly result in a bending failure. The new test featured a more gentle die radius to handle thicker blanks, which would reduce bending-dominated failures.

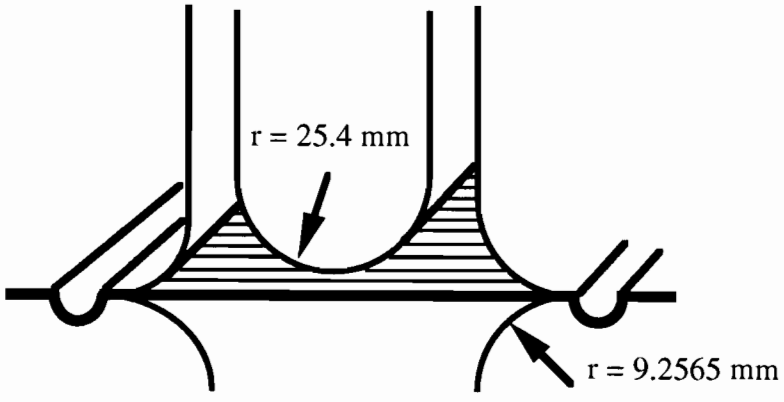

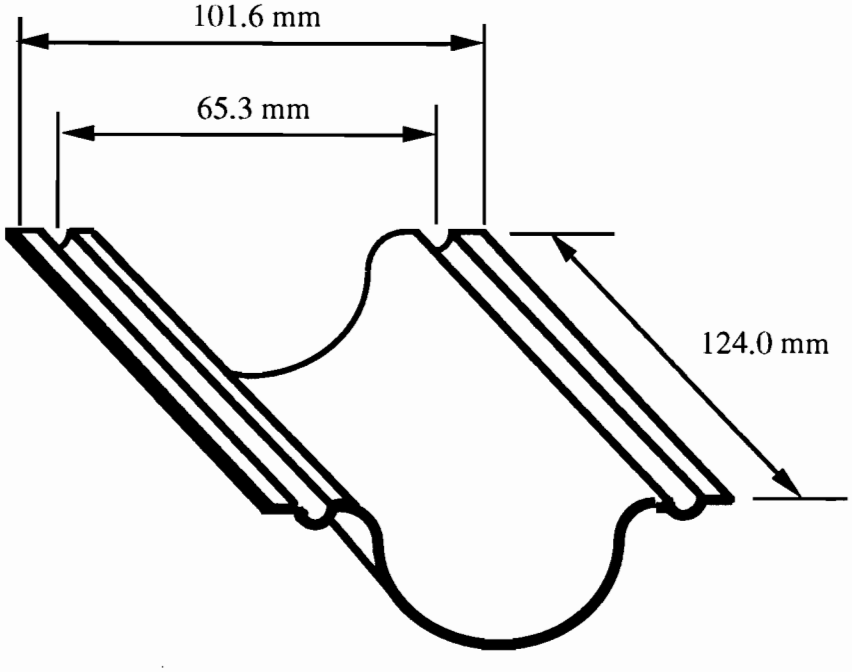

Figure 1. Schematic of the optimized *OSU Formability Test.*

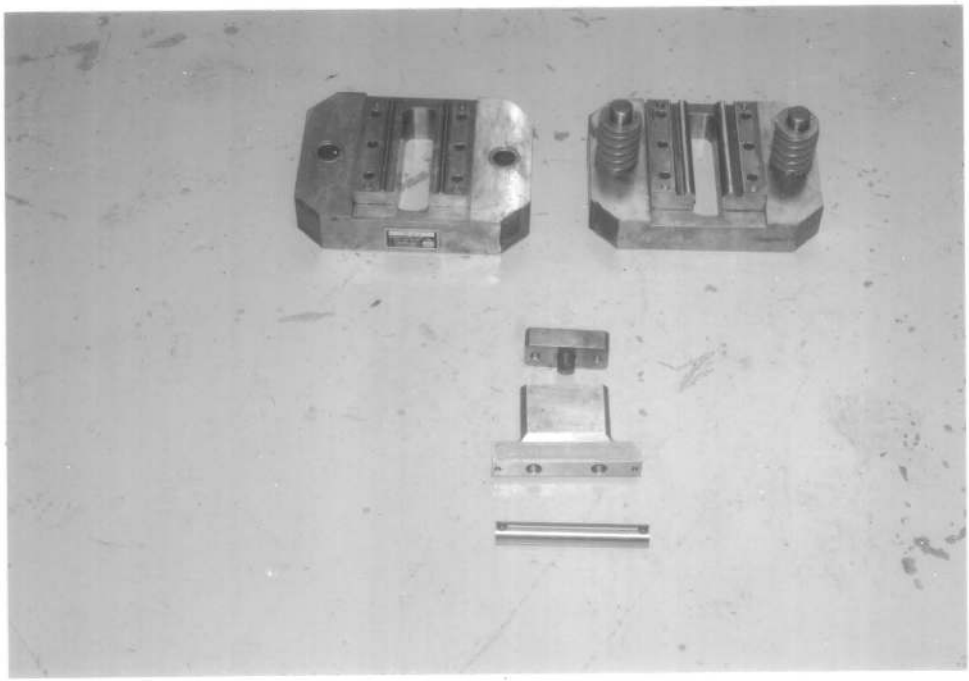

Figure 2. The tool set for the optimized *OSU Formability Test*

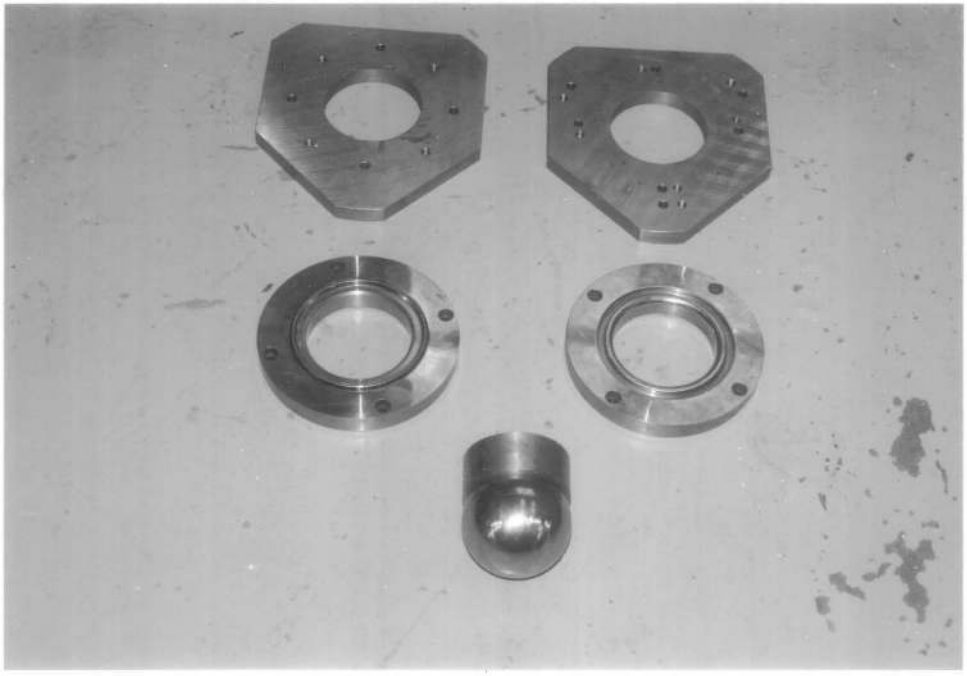

Figure 3. Tool set for the Limiting Dome Height test.

4.2 Experimental Procedures

The *OSU Formability Test* and the LDH Test experimental procedures are almost identical. Either set of tools (Figures 2 and 3) can be installed on a hydraulic double-action press at The Ohio State University [40] which has a maximum clamping force of 110,000 lbs (Figure 4). The blankholder pressure is usually held between 5500 and 5700 psi, which ensured a pure stretching condition. The sample is aligned carefully by eye on the lower die, such that the sample were set so they are parallel to the edges of the punch. During the test, the analog signals from the LVDT and the load cell are converted to digital data using a Data Translation [41] data acquisition system connected with an IBM XT personal computer. The data was collected at a rate of 500 points per second. The failure height is defined as the punch displacement at which the load on the ram starts to decrease. Each reported failure height for each test for a given condition is the average of 10 tests.

The dimensions of the optimized *OSU Formability Test* test blanks were 4.5" by 5", where the 4.5" dimension was parallel to the major stretch axis. The LDH test blanks were 5.25" by 7", with the 7" dimension being parallel to the major stretch axis. However, it was found for the welded blanks that the boundary conditions on the LDH could not be enforced (especially mash seam), so 7" by 7" blanks were employed for a full dome stretch. This is discussed in more detail in Chapter 4.

Figure 4. The double action hydraulic press at the Ohio State University.

5. The Uniaxial Tensile Test

5.1 Base Material vs. Weld Bead

The uniaxial tensile test was used in this study to determine two things:

1.) The constitutive law that governed the hardening behavior of the base material and the weld bead, and

2.) the uniform and total elongation of the weld material.

In this section, the experimental testing procedure for the uniaxial tensile test will be discussed, while the analytical procedures for determining hardening laws will be left for discussion in Chapter 5.

5.2 Experimental Procedures

Two types of tensile bars were used; the ASTM [42] standard 2" gage length tensile specimen for sheet testing and a 1" gage length subsize specimen. The standard 2" specimen was used for the base material, while the welded samples were tested with both 1" and 2" specimens. The 1" samples feature a smaller deforming area, which increases the fraction of the specimen that is weld bead material. The 2" gage welded samples were tested to compare overall elongation between the different size gages. Schematics of subsize and standard specimens are shown in Figures 5 and 6, respectively.

The tests for both specimens were run on an Instron [43] 1332 tensile frame that is controlled by an Interlaken 3200 controller [44] (Figure 7). The original area of the deforming region was measured previous to testing using a micrometer. Each sample was tested at an engineering strain rate of $5.0 \times 10^4\ s^{-1}$. The load was recorded from the load cell on the actuator and the displacement of the deforming region was recorded using a 1" extensometer for both samples. The data was recorded by the Interlaken controller and

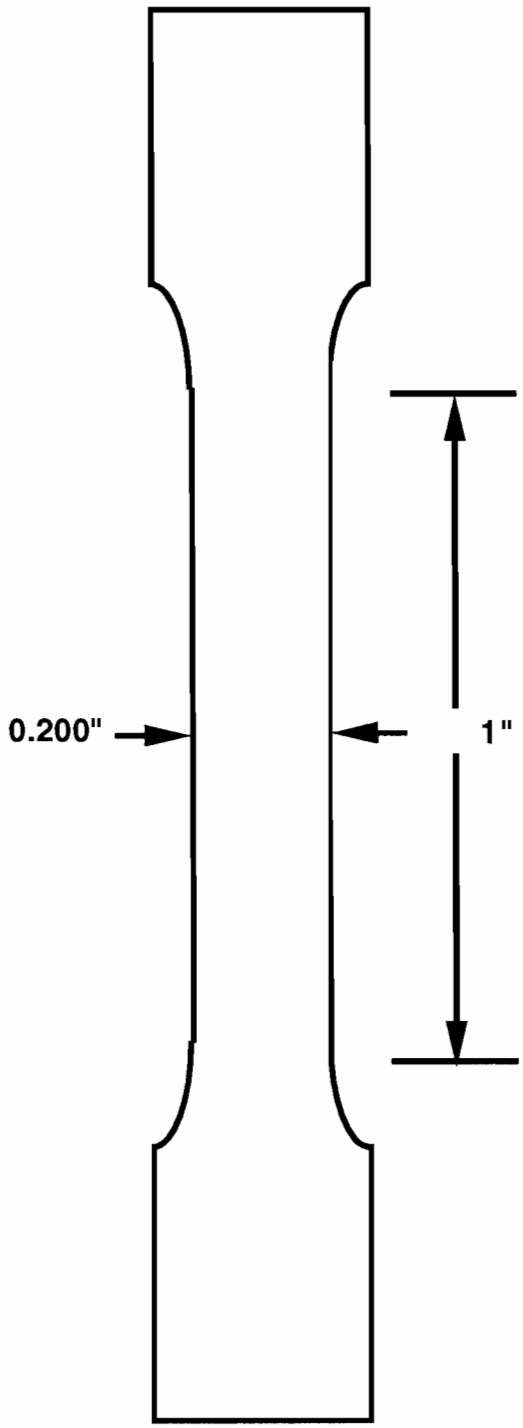

Figure 5. Schematic of the subsize tensile specimen.

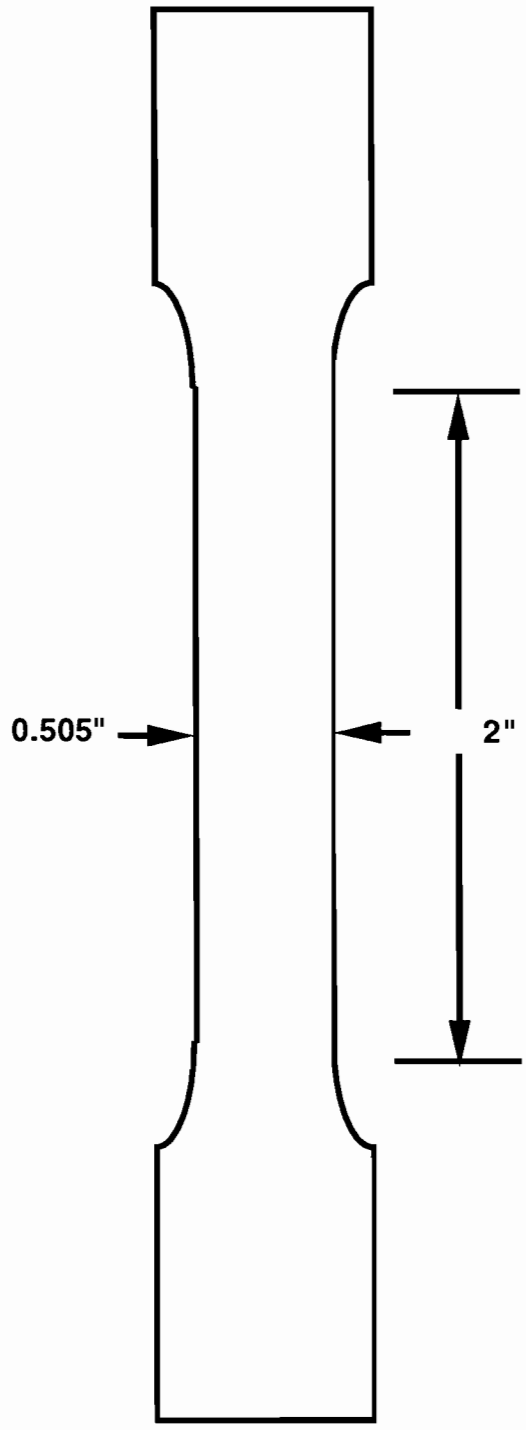

Figure 6. Schematic of the standard tensile specimen.

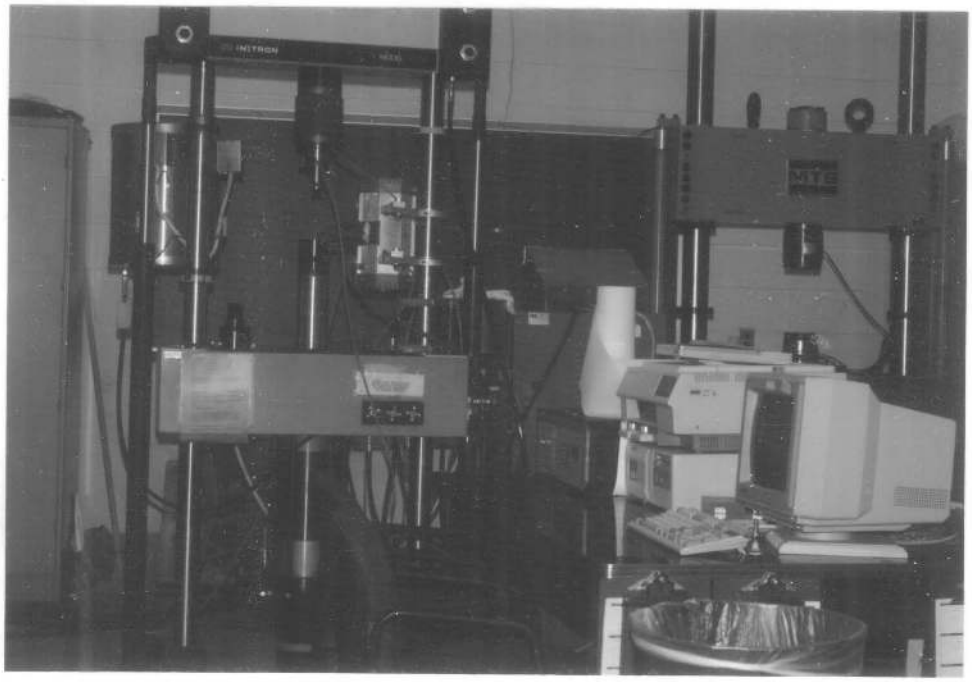

Figure 7. The Interlaken 3200 controller and the Instron 1332 mechanical testing frame.

saved as digital data to a file. This data was then converted to true stress-strain data using a program written by Wei Wang. This curves were used for the determination of the coefficients of the constitutive hardening law, which will be discussed in more detail in Chapter 5.

6. Forming Analysis using the *Hydraulic Forming Simulator*

6.1 Equipment Background

In order to observe the influence of weld location and weld type on the overall formability of a non-axisymmetric, three dimensional part, the scale fender die that is used on the *Hydraulic Forming Simulator* at the Ohio State University was used for the analysis. This geometry was designed by Yuji Hishida as a scaled down automotive front fender for laboratory investigation of the influence of a variable blank holder force on the wrinkling behavior of the workpiece. This study is described in detail elsewhere [45] and provides more detail on the design of the geometry. An actual photograph of the die set is shown in Figure 8.

The *Hydraulic Forming Simulator* is a double-action hydraulic press built by Interlaken Technology Corp. [44] especially for sheet forming research at the Ohio State University. What sets the *Simulator* apart is the fact that the loads and displacements of both the clamp and punch actuator are precisely controlled by an Interlaken 4000 controller [44]. This allows accurate measurement of the punch travel and exact control over the blank holder force, which will provide an accurate forming analysis. The press is described in more detail elsewhere [46]. A photograph of the *Hydraulic Forming Simulator* is shown in Figure 9.

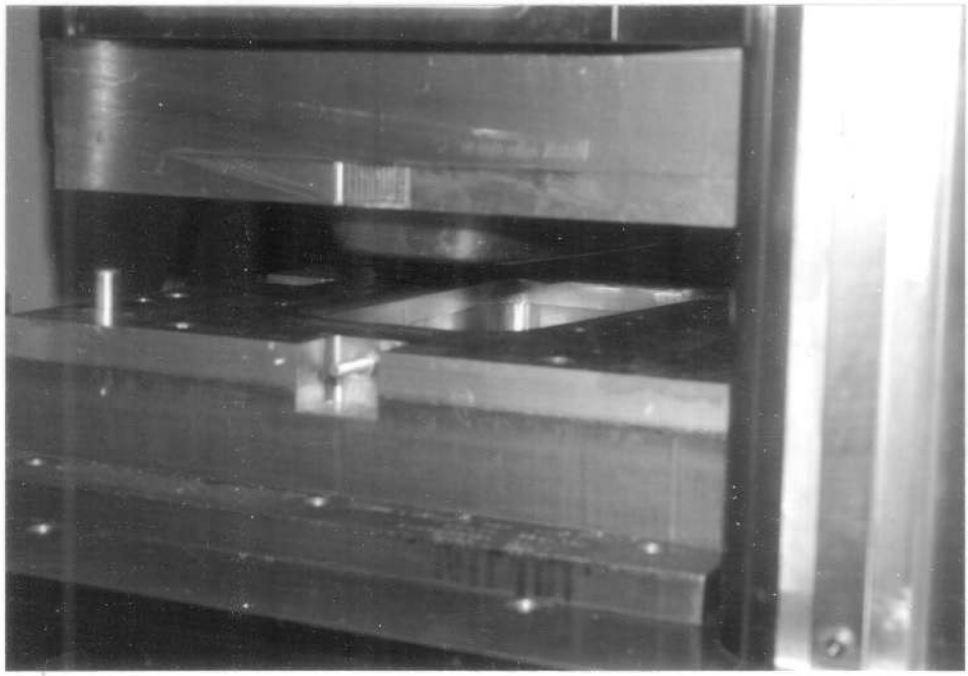

Figure 8. Photograph of the scale fender die tools on the *Hydraulic Forming Simulator* at the Ohio State University.

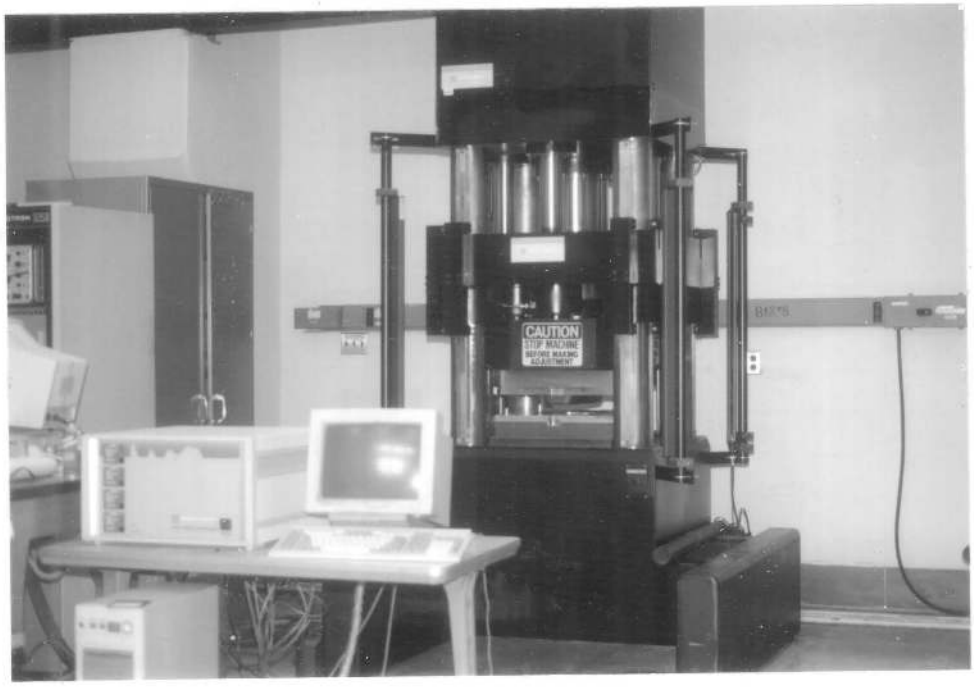

Figure 9. The *Hydraulic Forming Simulator.*

6.2 Experimental Procedure

The test specimens for the scale fender die were 14" by 17". Before testing, the blank is placed on the lower die plate. The actual test pattern is written in a program in the UTP [44] controller software. Therefore, once the program is activated, the computer controls the clamp displacement and load along with the punch displacement without human intervention. The HSLA/AKDQ blanks required 10 tons clamping force. This force was chosen because it was the blank holder force (BHF) that allowed the forming of the 1.8 mm AKDQ to 60 mm without wrinkling. The appropriate force was held constant while the punch deformed the blank at a rate of 0.63 in/min to a prescribed punch travel indicated in the program.

7. Finite Element Codes

Two finite element codes were used for the analytical investigation in this study, SHEET-3 and ABAQUS. The two programs will be described in this section.

7.1 SHEET-3

SHEET-3 [27] is a three dimensional finite element code that was developed at the Ohio State University. SHEET-3 features a rigid viscoplastic formulation, which is considerably more CPU efficient that elastic-plastic formulation. One drawback of a rigid plastic formulation is that springback is not accounted for. Springback is not a major issue in this investigation, but for future studies it will be important. SHEET-3 features membrane elements, which means there is no strain gradient in the through thickness direction. This again provides a more CPU efficient formulation, but does not account for the forces required to bend the material around a tool. For large tool radii, this is not a problem, but when the ratio of the radius of the tool to the thickness of the blank

(r/t) is less than 6, the bending of the material should be accounted for [30]. Also, in complex 3-D draw forming, wrinkling in the side walls is a major concern. SHEET-3 cannot predict wrinkling because of its membrane formulation.

SHEET-3 has the advantage of being able to account for the material anisotropy. It has been developed so Hill's 1948 [47] and 1979 [48] yield criteria can be accounted for, as well as Hosford's [49] yield function. It has been shown in previous work that the yield criterion used can have a large effect on the resulting strain distribution of a simulated part [28, 24], so it is important to account for anisotropy.

In this study, the code was internally modified to account for the different properties or thicknesses of the blanks. The code was changed so each element would either have a certain material property or thickness. However, the code was not modified to allow for different friction conditions for different regions.

7.2 ABAQUS

ABAQUS is a commercial multi-purpose finite element code that was developed by Hibbet, Karlsson and Sorenson, Inc. [26]. ABAQUS was used mainly in this study because it was a code used by both Ohio State and the industrial partners involved in this study, thus allowing the free exchange of input files and data. ABAQUS had other advantages, however. First, ABAQUS is an elastic-plastic formulation, which allows for the measurement of springback and any other elastic deformation. Also, ABAQUS features a finite strain shell element, which allows a stress gradient in the through thickness direction. Therefore, the bending stresses in the sheet can be accounted for. This will show the effect of bending when the r/t ratio is small and will also show the wrinkling behavior when applicable.

One disadvantage of ABAQUS compared to SHEET-3 is the lack of description of the plastic anisotropy of the material. The plasticity theory used by ABAQUS is the classic von Mises yield function, which has no material anisotropy. This would result in some error in the strain prediction, especially the minor strain.

One major advantage of ABAQUS over SHEET-3 is the ease of varying the element properties within a blank. Instead of modifying the code internally, the input file can define different element sets, and the properties of each element set can be defined separately. This also allows for the variation of friction from element set to element set, which is important in the simulation of the mash seam blank because the weld bead itself in a mash seam welded blank may have different friction properties.

CHAPTER IV

LABORATORY FORMABILITY RESULTS

1. Introduction

One of the crucial issues that needs to be addressed in the use of tailor-welded blanks is what tests (if any) can be used in the laboratory to give some sort of a prediction of how the blank will perform in the actual forming of a part. In this chapter we are looking three laboratory scale forming tests: The Limiting Dome Height Test, The *OSU Formability Test*, and the standard uniaxial tension test. The uniaxial tension test provides the tensile ductility information, the OSU Test evaluates the weld in a stable plane strain state, while the LDH Test examines the forming behavior of the weld under a complex loading scheme (hemispherical punch). These three tests represent a wide range of forming conditions and allow us to look at the behavior of a tailor-welded blank under these different conditions.

It will be noted here that the HSLA/AKDQ blanks performed identically to the 0.8/1.8 AKDQ combination in terms of deformation mechanisms. Therefore, for simplicity, the remainder of the report will be focused on the HSLA/AKDQ combinations. The finite element work was carried out completely on the HSLA/AKDQ blanks. The absolute numbers were slightly different for the formability results between the two combinations, and this data is listed in Table 6.

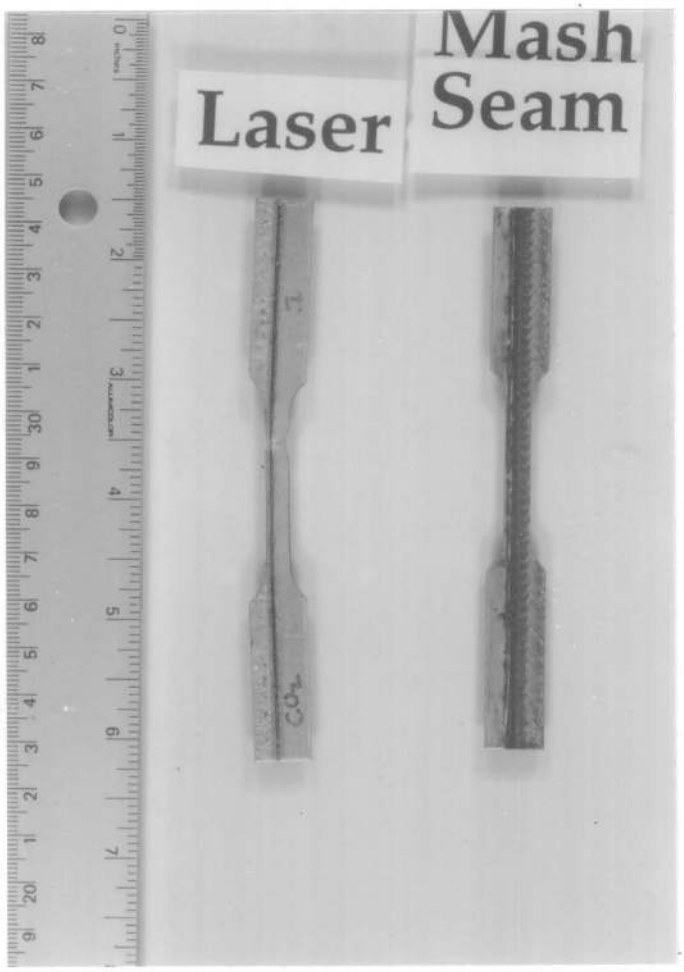

Figure 10. Photograph of the subsized tensile specimens for both laser and mash seam.

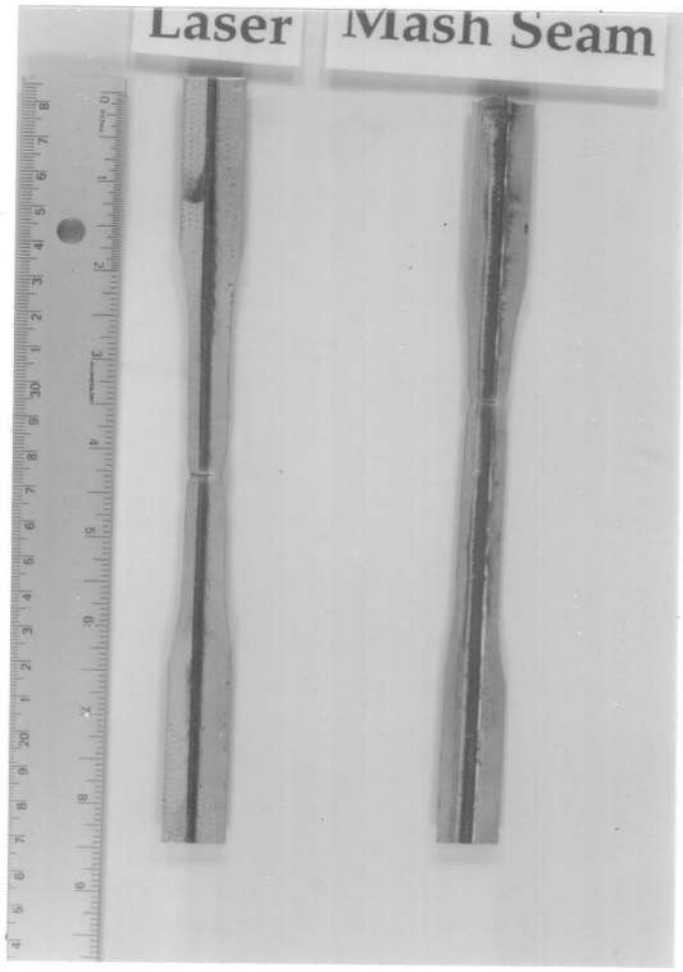

Figure 11. Photograph of the standard sized tensile specimens for both laser and mash seam.

2. Uniaxial Tensile Data

As mentioned earlier, an ASTM E-8 [42] standard specimen and a subsize specimen was used. The subsized specimen had a 1" gage length and deformation region that was 0.2" wide. Figure 10 and 11 shows the subsize and standard size tensile bars, respectively, for both weld types. The mash seam weld bead was large enough that the entire deformation region of the subsize specimen was weld bead. Therefore, the load displacement curve of the subsize mash seam samples is the actual hardening behavior of the weld.

The uniform elongation for the subsize and full size bars for all weld types are shown in Table 4. The data in this table is the average of three tests run for each condition. For the standard size specimens, there is no difference in uniform elongation between the two types of laser beads. This is not terribly suprising since the only difference is the source of the beam while the interaction between the beam and material is unchanged. Comparing this data to the base material data in Table 4, one finds the uniform elongation for the welded samples is about the same as the base HSLA. Hence, the presence of the weld did not decrease the ductility at all. For the mash seam beads, the mash seam weld without any planishing had similar tensile ductility to the laser beads. Cold planishing reduced uniform elongation by about 1/3. However, hot planishing brought the total elongation back up significantly, but not quite to the level of the original weld. The hot planishing was successful in elimination the majority of the cold work, as was the original purpose of hot planishing.

One of the most interesting and significant points of this data is the difference between of the standard size specimens to the subsized specimens. The subsized specimens showed significantly less ductility for the laser welds

Table 4. Uniaxial tensile data for the different welds of HSLA/AKDQ blanks using standard and subsized samples.

	Standard	Subsized
1.8 mm AKDQ (Base)	22%±0.7%	22%±0.7%
2.1 mm HSLA (Base)	18%±0.5%	18%±0.7%
CO_2 Laser	18%±0.6%	11%±1.2%
YAG Laser	18%±0.5%	15%±1.1%
Unplanished Mash Seam	18%±1.0%	13%±0.7%
Cold Planished Mash Seam	5%±0.2%	4%±0.2%
Hot Planished Mash Seam	15%±1.8%	15%±1.1%

and the unplanished mash seam weld. The ductility dropped 5%, nearly 1/3 of the total value. The explanation of this behavior is the subsized specimens test a material that is more representative of the weld bead. For the laser welded samples, the weld bead makes up a much more significant fraction of the total specimen in a subsized sample than a standard specimen. Therefore it would be expected that the elongations of the weld material is much less than that of the base materials. As reported in the literature review, other studies [8] have evaluated the mechanical properties of the laser weld bead alone and found the tensile ductility of a weld bead to be in the range of 4-7.5%.

Appendix A outlines the microstructural and microhardness of each weld bead observed in this study. In this appendix, it is observed that the

microhardness of the laser weld bead is much higher for the weld bead itself than it is of the base material (Figures 74 through 77). Also, the microstructure is martensitic from the rapid cooling in a laser weld (Figures 84 through 87). Therefore, one would expect much lower ductility from a laser weld bead.

The same phenomena is observed for the mash seam weld. In the subsized samples, only weld bead was actually tested, so the 13% total elongation is the actual value for the mash seam weld material. The increased ductility of the standard specimen was a result of the base material surrounding the weld bead. The affected region in an unplanished mash seam weld in approximately 7 mm (Figures 78 and 79, Appendix A). Therefore, the addition of the base material to the tensile bar would add a more ductile material to the tensile bar, thus increasing the ductility of the standard size bar. It is not suprising that there was little change for the planished and hot planished welds. Both processes produce a much larger affected zone in the base materials than in the weld without any planishing (Figures 80 through 83, Appendix A). In both cases the affected zone ranges somewhere between 10 and 14 mm, which would be the entire size of a standard specimen as well. Therefore, the structure and properties are nearly the same throughout the cross section of the both the subsized and the standard sized sample, resulting in nearly the same tensile ductility for both sizes.

All this raises one important question: which (if any) of the tensile test geometries can be used to try to measure the actual formability of a tailor-welded blank? The subsize bars tests the true weld properties, but in a real forming operation the weld would obviously be surrounded by some sort of base material, resulting in a higher ductility, as shown with the standard size specimen. However, would the ductility increase even more if the gage

dimensions were 1" by 4", or 2" by 8"? The uniaxial tensile test cannot predict the forming limit of a tailor-welded blank. The tensile test can only provide a direct comparison between welds with a bead of similar geometry, i.e. a CO_2 laser and a Nd:YAG laser. Even comparing a laser to a mash seam weld cannot be considered a direct comparison, as the fraction of the base material surrounding the weld beads are not the same.

3. Formability Test Data

Table 5 shows the comparison of the total elongation of the standard size specimens, the failure heights of the optimized *OSU Formability Test*, and the failure height of the full dome stretch test. The tensile test data is again the average of three tests, while the dome and OSU data is the average of 10 tests. In the following sections, the data of this table will be compared and discussed and it's usefulness to actual forming will be addressed.

3.1 Uniaxial tensile data vs. *OSU Formability Test*

Figure 12 correlates the results of the *OSU Formability Test* to the elongation to failure of the different weld types. The OSU test ranks the welds in the same way as the tensile test. This is not suprising; the deformation modes of the OSU Test and the uniaxial tension test are very similar. In the OSU Test, the weld is stretched unidirectionally, as in the tensile test. All of the loading is parallel to the weld, just as in the tensile test. The OSU Test is plane strain, and the deformation is out-of-plane, which is different from a uniaxial tensile test. However, there is no loading normal to the weld, so all of the stretching of the weld is in the same direction.

What is interesting, however, is the relative difference between the tensile results (weld-to-weld) and the OSU Test data. The cold planished tensile ductility is half of the mash seam weld without planishing, but there is only a

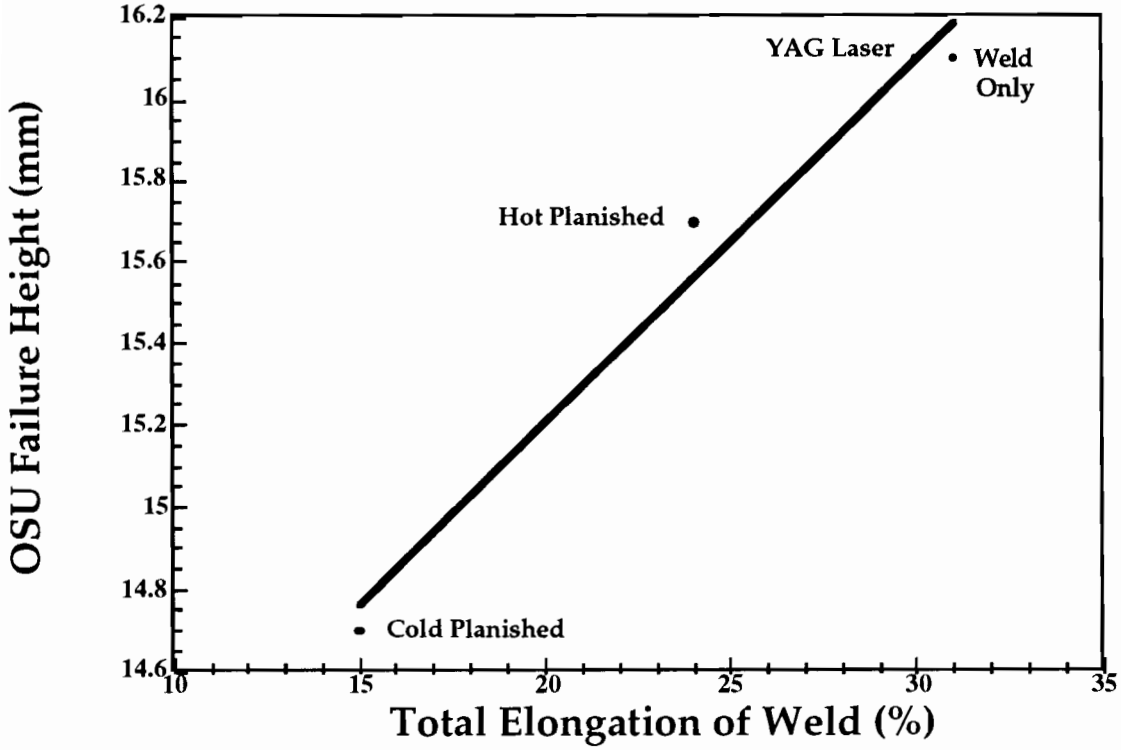

Figure 12. Correlation of the failure of the *OSU Formability Test* to the total elongation of the weld in uniaxial tension.

Table 5. The total elongations of the welds for HSLA/AKDQ blanks in a uniaxial tensile test, the failure height of the OSU Test and the full dome stretch.

	Total Elongation	OSU Test (mm)	Full Dome (mm)
2.1 mm HSLA (Base)	39.8%±0.4%	17.7±0.2	32.7±0.6
1.8 mm AKDQ (Base)	44.4%±0.6%	19.0±0.1	35.8±0.6
CO_2 Laser	29%±0.6%	16.0±0.3	24.6±0.5
YAG Laser	30%±0.7%	16.0±0.3	23.6±0.5
Unplanished Mash Seam	30%±1.0%	16.0±0.7	27.0±0.7
Hot Planished Mash Seam	24%±0.4%	15.5±0.7	24.4±0.7
Cold Planished Mash Seam	15%±2.2%	14.5±0.2	25.7±1.0

Table 6. The total elongations of the welds for AK0.8/AK1.8 blanks in a uniaxial tensile test, the failure height of the OSU Test and the full dome stretch.

	Uniform Elong. (Sub.)	Uniform Elong. (stand.)	Total Elong. (sub.)	Total Elong. (stand.)	OSU Test (mm)	Full Dome (mm)
0.8 mm AKDQ (Base)	21%±0.5	24%±0.5	40%±0.5	44%±0.4	17.7±0.2	32.7±0.5
1.8 mm AKDQ (Base)	22%±0.6	22%±0.4	41%±0.3	44%±0.6	19.0±0.1	35.8±0.7
CO_2 Laser	22%±0.7	22%±1.0	34%±0.8	35%±0.8	19.2±0.3	19.8±0.5
YAG Laser	18%±1.0	19%±1.1	27%±0.9	27%±0.4	18.7±0.4	19.6±0.4
Unplanished Mash Seam	14%±0.6	18%±1.2	23%±0.8	35%±0.6	18.8±0.2	21.5±0.5
Cold Planished Mash Seam	6%±0.8	8%±1.3	15%±0.7	21%±0.5	17.3±0.5	21.0±0.3
Hot Planished Mash Seam	12%±0.2	14%±0.7	22%±0.1	30%±0.2	18.1±0.5	20.9±0.5

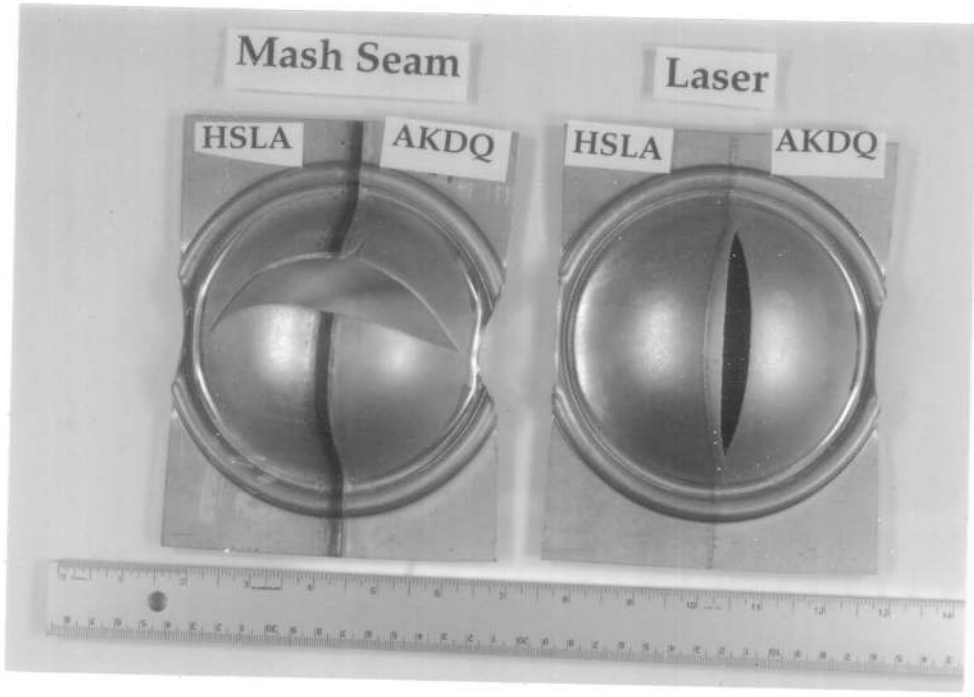

Figure 13. The two different failure modes observed for the laser and the mash seam HSLA/AKDQ blank in the Limiting Dome Height test. The HSLA material is always on the left side of the blank. The mash seam blank is also on the left.

difference of 1.5 mm in the OSU Test data, with a scatter of 0.5 mm. Therefore, the OSU Test may rank the weld types in the same way as the tensile test, but the absolute difference in the ranking appears to be quite a bit different. In overall formability, the difference between welds in the OSU Test to be very small.

3.2 Uniform Elongation vs. The Dome Test

3.2.1 The Limiting Dome Height Test

Failure heights of the full dome stretch are also featured in Table 5. Originally, the plane strain LDH was to be used, but the LDH data was invalid. The test worked fine for laser welded blanks, but for mash seam blanks the boundary conditions could not be enforced. An LDH blank is not fully clamped on the edges. The larger mass of material in a mash seam bead sufficiently increased the punch force required to deform the sample, resulting in a higher punch force that caused the blank to pull out of the die. Therefore, the failure height was much higher for a mash seam blank than it was for a laser welded blank. Also, the failure modes were very different between the two weld types. For the laser welded blank, the weld was pulled in the direction of the stronger material, resulting in higher strains in the transverse direction in the weaker material close to the weld, until the base material failure strain is exceeded. Since the boundary condition was not being enforced at the edge of the blank for the mash seam weld, the weaker material did not stretch as much. Instead, it pulled out of the die. Therefore, the strain in the transverse direction resulting from the weld movement was much smaller and didn't cause failure. Instead, the punch travel was large enough to stretch the weld to the point of failure in the weld. The different failure modes are shown in Figure 13. The movement of the laser weld can be seen, showing the failure of the base material. The mash seam, on

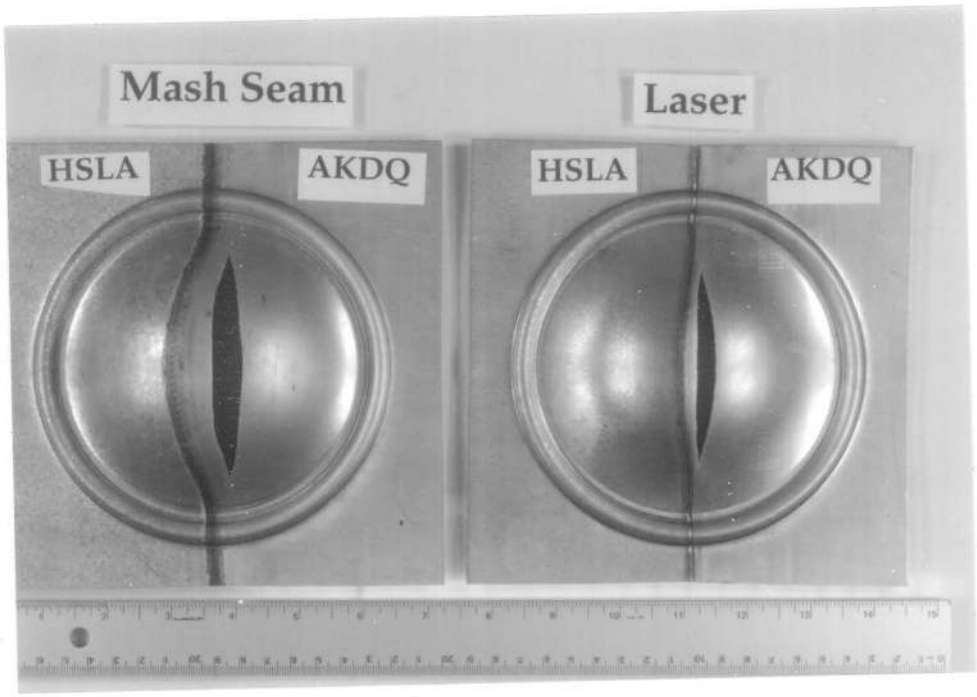

Figure 14. Failure modes for the Full Dome Stretch for HSLA/AKDQ blanks, both weld types. The HSLA material is always on the left, and the mash seam blank is on the left also.

the other hand, failed in the weld, with the crack propagating normal to the weld and growing out into the base material.

3.2.2 Full Dome Stretch

Because of the problems encountered using the LDH Test, we went to a full dome stretch test. A full dome stretch is when the blank is locked at all points around the punch, resulting in a balanced biaxial loading. This will prevent the blank from pulling out of the die, allowing a comparison between the weld types.

The data on Table 5 shows no correlation between the tensile ductility and the full dome stretch failure height. Even though the cold planished ductility is half that of the laser welds, it has a higher failure height for the full dome stretch than the laser welded blanks. This is explained by the failure mode of the full dome stretch blanks (Figure 14). Similar to the failure mode of the LDH laser welded blanks, the weld was pulled in the direction of the stronger material, resulting in a crack initiating in the weaker material parallel to the weld and then propagating parallel to the weld. With the fully clamped samples, this failure mode was observed for all welds. Therefore, since the deformation was not limited by the mechanical properties of the weld, there would be no correlation to the ductility of the welds determined in an uniaxial tensile test.

However, as one looks at the data, there is a only a slight difference from weld type to weld type. This is similar to the results of the OSU Test. In overall formability, there seems to be little difference between weld types.

At this point, we have found two different failure modes for two different of stretch formability tests. In the *OSU Formability Test*, the weld deformation was unidirectional, which resulted in the failure in the weld. There was no lateral movement of the weld and the formability was limited by the ductility of

the weld. In the full dome stretch test, the weld was pulled in the direction of the stronger material, resulting in the failure of the weaker material. Therefore, it appears that the failure mode is dependent upon the amount of weld movement. There needs to be an understanding under what conditions and what variables have the strongest influence on the weld movement. Knowing how the processing conditions and material properties influence these deformation modes and having the ability to predict this weld movement could help design a part that would have optimum formability.

We have observed two failure modes in the forming of tailor-welded blanks containing two different materials. The schematic in Figure 15 explains the two different modes. When the loading is primarily in the direction of the weld, the formability of the entire blank is dependent upon the ductility of the weld. When the loading is primarily transverse to the weld line, the formability in dictated by the plane strain forming limit of the weaker/thinner material.

3.3 Strain Distribution in Dome Test

There have been two different types of failures noted in tailor welded blanks and they have been governed by the amount of weld movement. Therefore, the formability of a blank has been defined as a function of this weld movement. This is an incorrect assumption, however. The formability of any sheet metal is defined by the limit strains of the material. Therefore, if this weld movement is going to directly influence the formability of the sheet, it must first affect the limit strains. For example, the weld may move, but if the boundary forces allows the edge of the blank to move, there would be no extra strain in the weaker material and formability would not be affected.

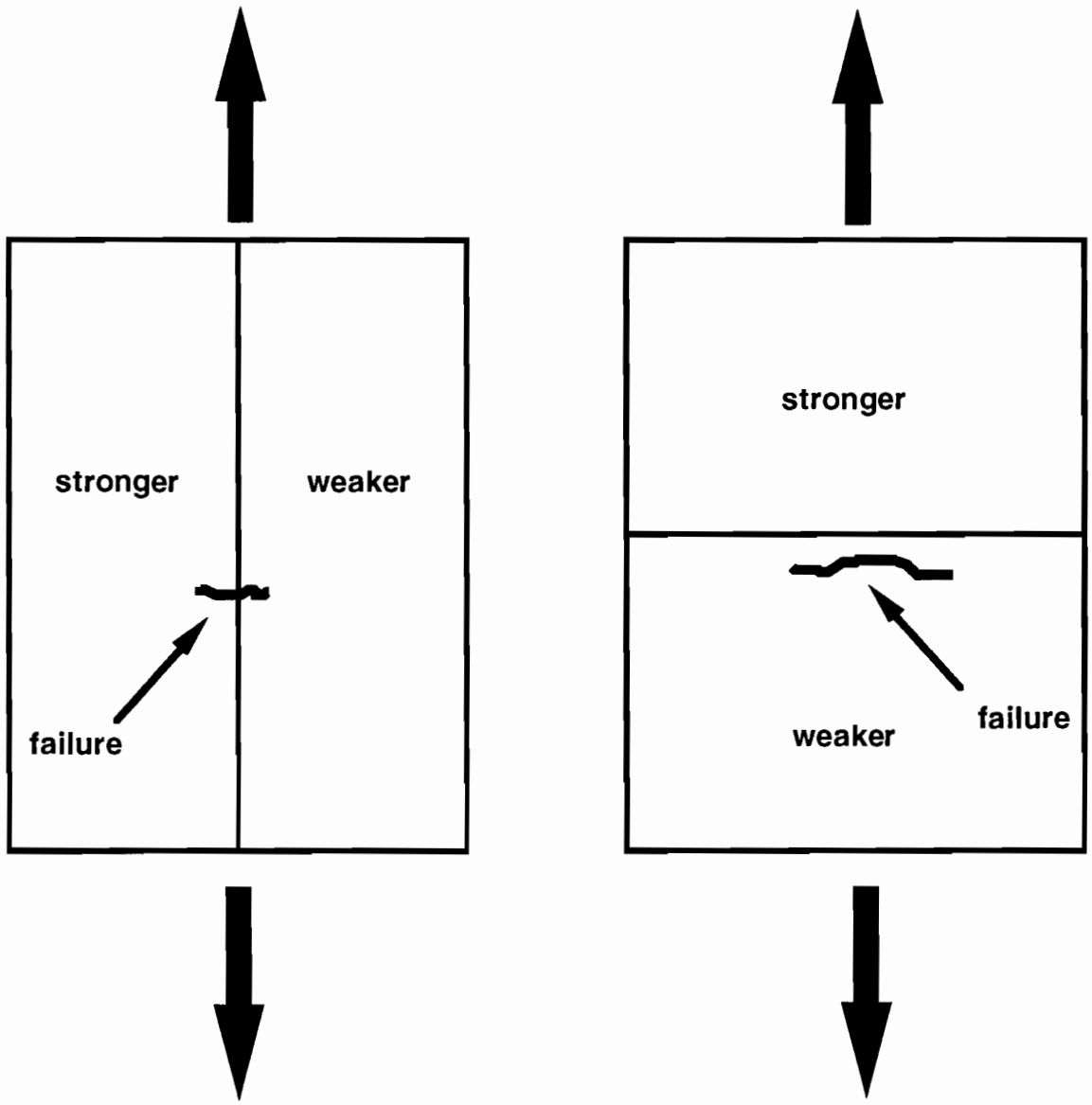

Figure 15. Two different failure modes for tailor-welded blanks. When the primary loading was in the direction of the weld line, the formability is limited by the ductility of the weld bead (left side). When the loading is normal to the weld, the formability is limited by the plane strain forming limit (on the right).

Therefore, as we look at the influence of weld movement on the formability of the dome test, we must also look at the resulting strains in the dome test. Figure 16 shows the experimentally measured strain distribution over the top of the dome normal to the weld line. The strain direction is also normal to the weld line. The strains local to the weld (less than 10 mm away) increase significantly, while the rest of the strain distribution is not strongly affected. Therefore, the influence of the weld movement on the strains seems to be in increasing the strains local to the punch in the weaker material.

There also needs to be a better understanding of what the failure criterion is when the sample fails as a result of weld movement. To understand this better, a circle gridded 0.8AK/1.8AK YAG laser welded blank was tested to height of 15.5 mm in the full dome stretch. At this punch travel, an incipient neck had formed in the 0.8 mm AKDQ, parallel to the weld. Therefore, the limit strain of the blank had been reached. The displacements of the circles in this critical area were measured in both principal axes to determine these limit strains. These strains are plotted against a typical FLD for a drawing quality steel taken from Hecker [50]. From this plot it is observed that the limit strains are just below or on the FLD for a drawing quality steel. Therefore, when the weld moves and fails in the base material, the failure is dictated by the forming limit diagram, just as in the base material.

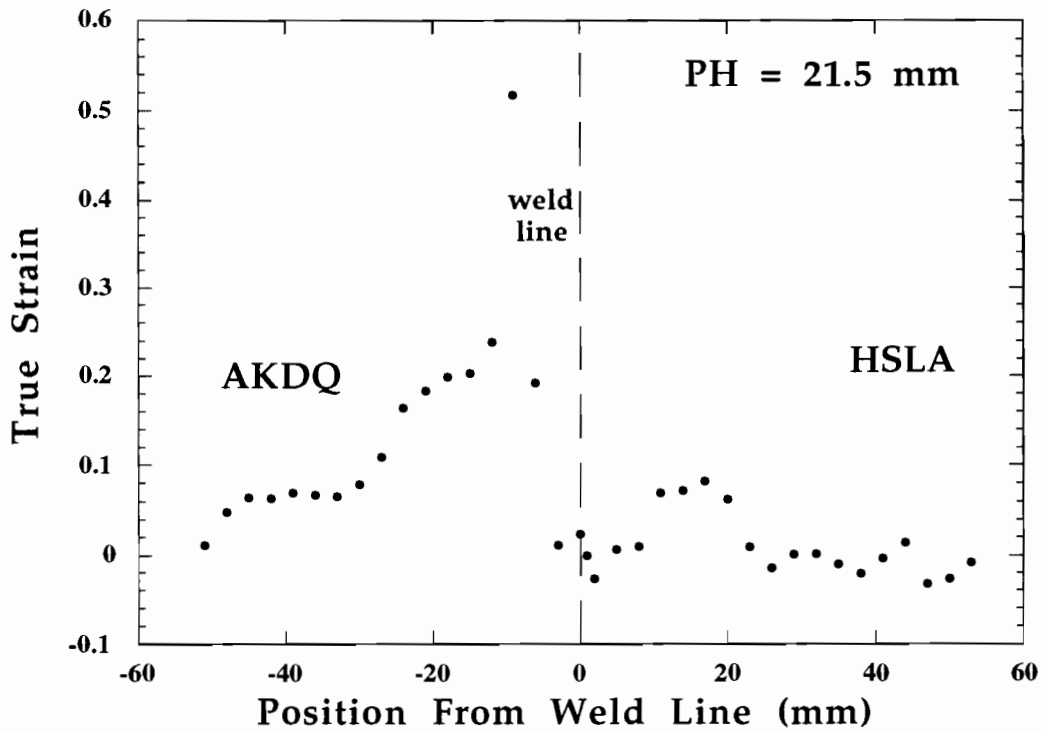

Figure 16. Measured strains along the line normal to the weld with the strain direction also normal to the weld line for an HS2.1/AK1.8 blank.

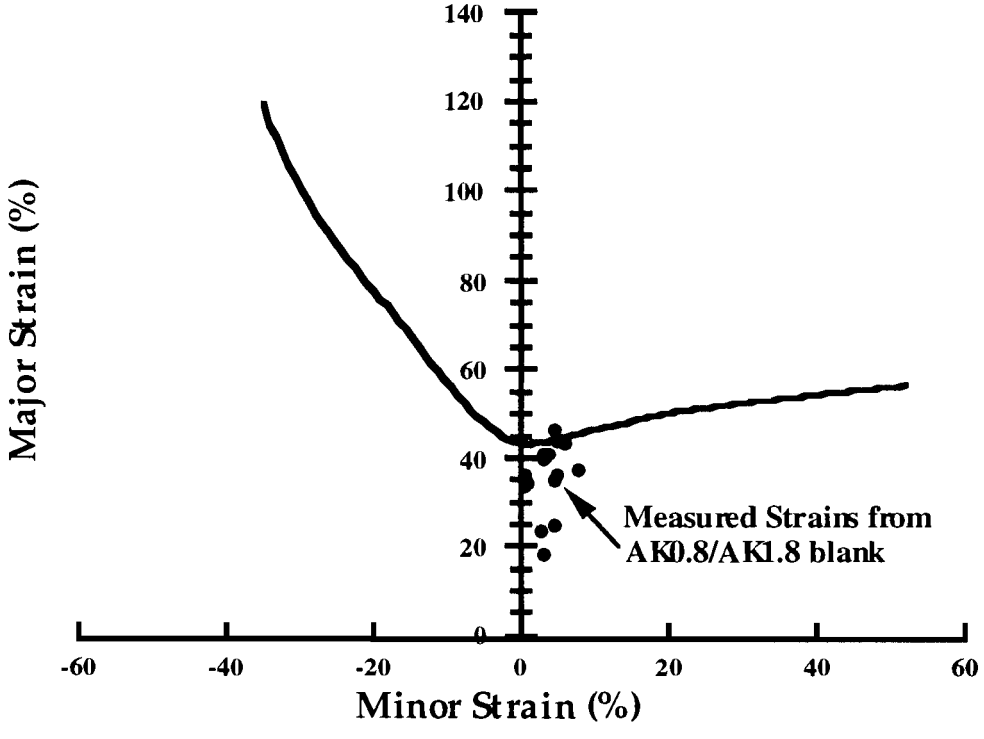

Figure 17. Measured limit strains compared to drawing quality steel FLD taken from Hecker [50].

CHAPTER V

DETERMINATION OF MATERIAL CONSTITUTIVE BEHAVIOR

1. Introduction

In order to model a sheet forming process, one needs to know the stress-strain relationship of the material that is being formed. In this chapter, we will determine the stress-strain constitutive laws that govern the deformation of the base and weld materials in the tailor-welded blanks that we are analyzing in this study. The point of this exercise is to determine a rough estimation of the plastic properties of the weld materials that can be implemented into a finite element code, not an exact description of the weld bead stress strain behavior. Therefore, it acknowledged now that there may be some built-in error in the calculation, i.e. inexact measurements of the actual cross sectional area of weld bead. However, the properties should be a reasonably close approximation such that they will give a decent representation of the actual mechanical behavior of the weld in a FEM simulation. Only the HSLA/AKDQ weld bead results are reported.

2. Base Materials

The tensile testing for the base materials followed the procedure outlined in Chapter 3, section 5.2. The true stress-strain curves were calculated from the load-displacement data and coefficients for the hardening law were determined using a curve-fitting program [51]. The AKDQ material precisely followed the

Swift hardening law, which is given as

$$\bar{\sigma} = K(\bar{\varepsilon} + \varepsilon_o)^n \qquad (1)$$

where $\bar{\sigma}$ is the effective stress, $\bar{\varepsilon}$ is the effective strain, ε_o is the prestrain, n is the work hardening exponent and K is the strength coefficient. The coefficients for the 0.8 mm and the 1.8 mm AKDQ material are given in Table 7. The experimental true stress-strain curve is shown in Figure 18.

The HSLA material was much different. The material exhibited a yield point elongation of nearly 6%, which was also observed in the material characterization performed by National Steel [39] (see Table 3). However, upon work hardening, the material followed a Swift-type hardening behavior. The curve fit coefficients for the Swift hardening law are listed in Table 7 with the AKDQ coefficients. The experimental true stress-strain curve is shown in Figure 19.

Table 7. The coefficients of the Swift hardening law for the base HSLA and the AKDQ steels.

	K (ksi)	n	ε_o
0.8 mm AKDQ	77.1	0.191	0.001
1.8 mm AKDQ	72.3	0.194	0.001
2.1 mm HSLA	108.2	0.174	0.001

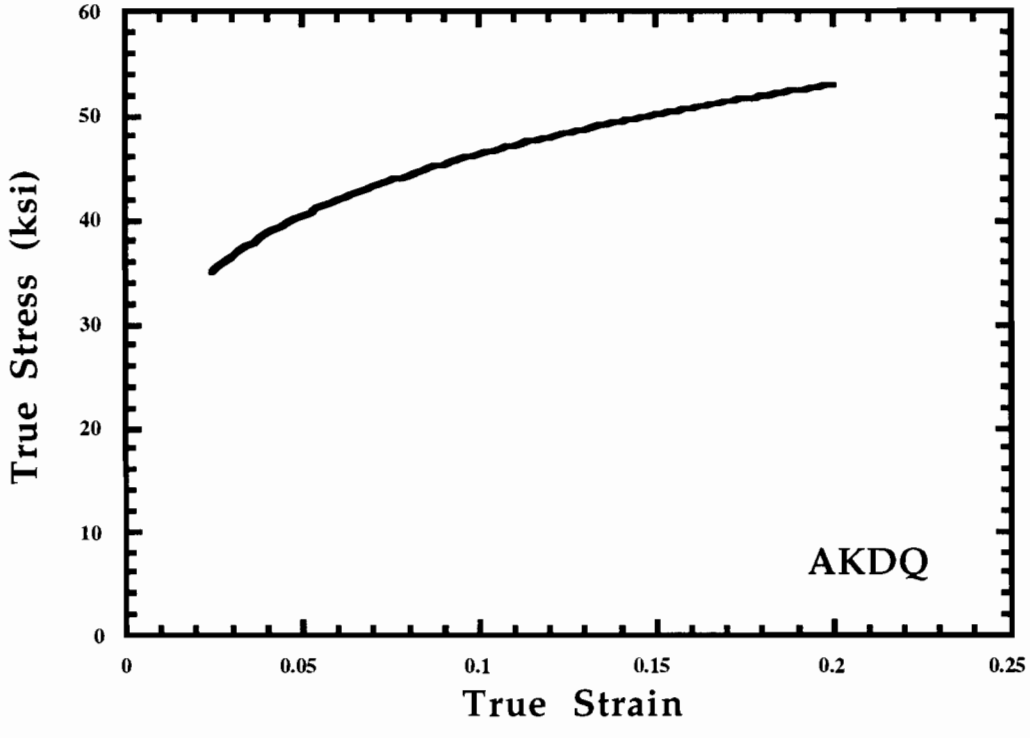

Figure 18. Experimental uniaxial true stress strain curve for the 1.8 mm AKDQ material.

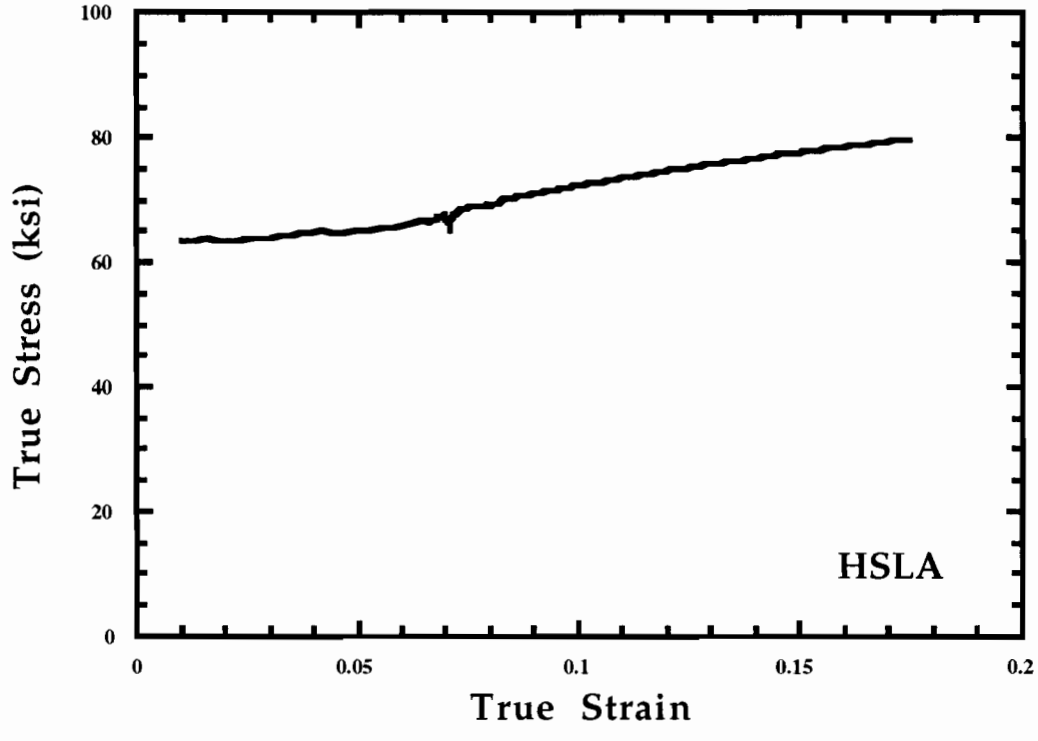

Figure 19. Experimental uniaxial true stress strain curve for the 2.14 mm HSLA material.

3. Mash Seam Welds

The subsize (1" gage) tensile specimens were used for the determination of the hardening laws for the mash seam welds. The resulting load-displacement relationship from these tensile tests is the direct hardening behavior of the actual mash seam weld bead. This is because the width of the deforming region was all affected area for the mash seam beads. The microstructural and microhardness evidence for this is discussed in Appendix A (Figures 78 through 83). Therefore, the direct load displacement curves from the subsized samples were converted to true stress-strain and the parameters for the constitutive hardening law were determined using the curve-fitting program.

The true stress-strain curves for the mash seam weld beads for the HSLA/AKDQ welds are shown in Figure 20. The unplanished mash seam weld bead and the hot planished weld bead have nearly the same hardening behavior as the base HSLA material. The cold planished stress-strain curve is at a much higher stress level and has a much lower tensile ductility. This is a result of the planishing step . The induced cold work as the weld bead is deformed would result in a higher dislocation density, hence a higher flow stress, and a severely reduced tensile ductility. The hot planishing, however, heat treats the weld region to reduce the influence of the cold work.

The coefficients for the constitutive hardening laws for the HSLA/AKDQ weld beads are presented in Table 8. The weld beads were found to follow the classical Holloman [52] hardening law

$$\bar{\sigma} = K\bar{\varepsilon}^{n} \qquad (2)$$

where $\bar{\sigma}$ is the effective stress, $\bar{\varepsilon}$ is the effective strain, K is strength coefficient and n is the coefficient of work hardening. This is not suprising, since most ferrous alloys follow this hardening law. The amount each weld bead work

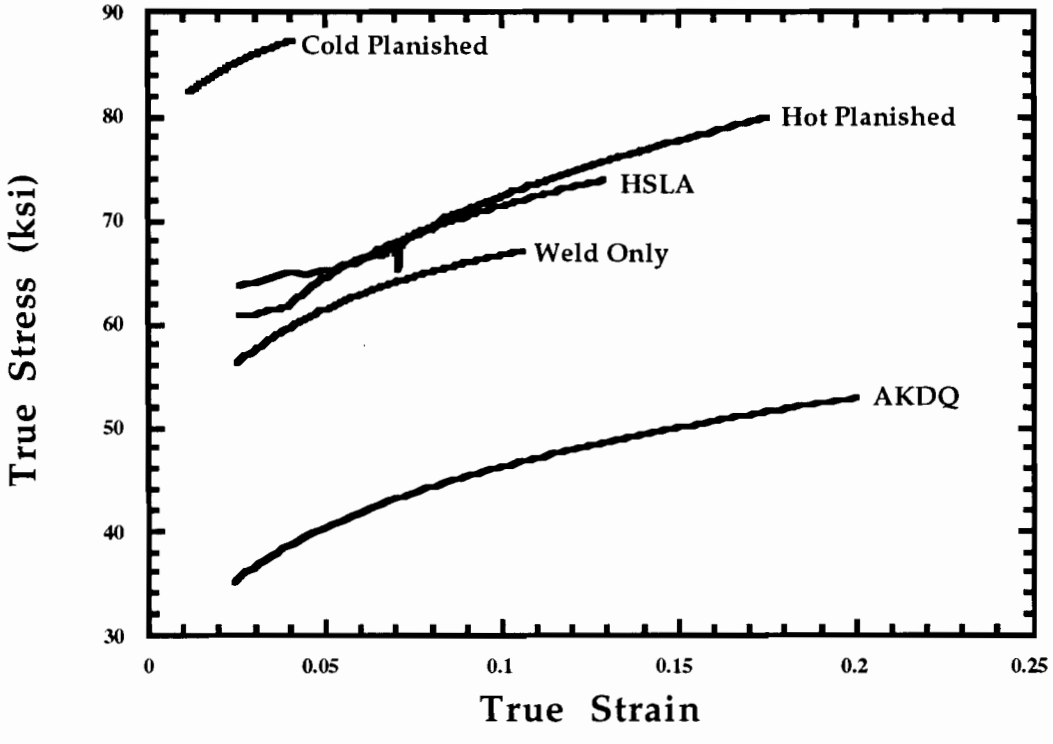

Figure 20. Experimental true stress-strain curves for the three mash seam welds.

hardens varies significantly, as can be observed by the variation in the n value for the three types of weld beads.

4. Laser Welds

The laser weld beads were tested using 1" gage length tensile specimens. Because the laser weld bead is narrow (< 1 mm) there is still base material surrounding the weld bead in the deforming region. Therefore, in order to determine the stress-strain relationship of the weld bead itself, an analytical procedure was developed to separate the properties of the base and weld bead materials. This procedure assumed the entire composite was in uniaxial tension and subtracted the load supported by the base material from the total load. This procedure is outlined in detail in Appendix B. Once the effective stress-strain curves are determined for the laser weld bead, the stress-strain curves are fit to a constitutive hardening law using the curve fitting program used for the mash seam welds.

As would be suspected from reported microhardness values in literature [2] and in Appendix A, the laser welds are much stronger than the base materials. The effective stress of the weld bead itself is much higher than the effective stress of the specimen calculated directly from the load cell (Figure 21), and the flow stress of the weld bead for both welding processes is nearly twice that of the base materials at the same effective strain (Figure 22). There is a slight difference in the flow stresses between the CO_2 and the Nd:YAG samples.

The constitutive law that describes the hardening behavior of the HSLA/AKDQ welds is also unique (Table 9). Instead of following the standard Hollomon equation [52], as the mash seam welds did along with almost all other ferrous materials, these materials followed a saturation type hardening law as described by Voce [53], which is defined as:

Table 8. Coefficient of Holloman law for different mash seam weld beads.

	K (ksi)	n
Unplanished	89.6	0.124
Cold Planished	101.0	0.046
Hot Planished	98.7	0.150

Table 9. Coefficients for saturation type hardening law for laser welds.

	K (ksi)	A	B
CO_2	141.9	0.54	-37.6
YAG	137.3	0.24	-25.1

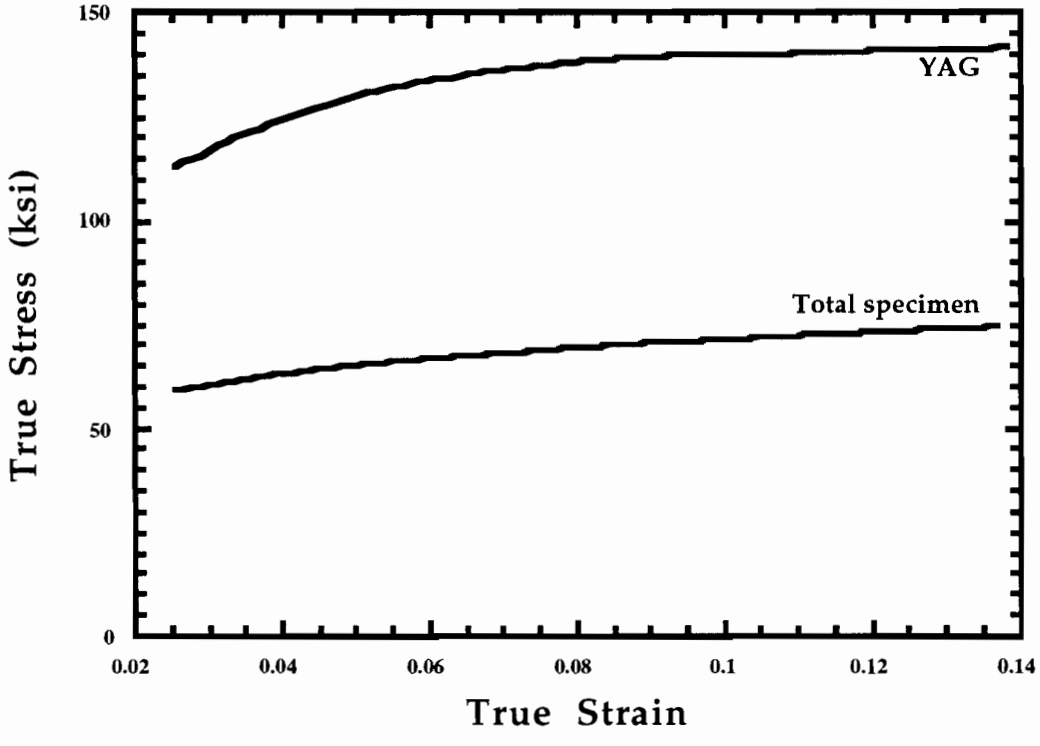

Figure 21. The calculated true stress strain curve of the Nd:YAG laser weld bead compared to measured stress strain curve of the HSLA/weld bead/AKDQ composite.

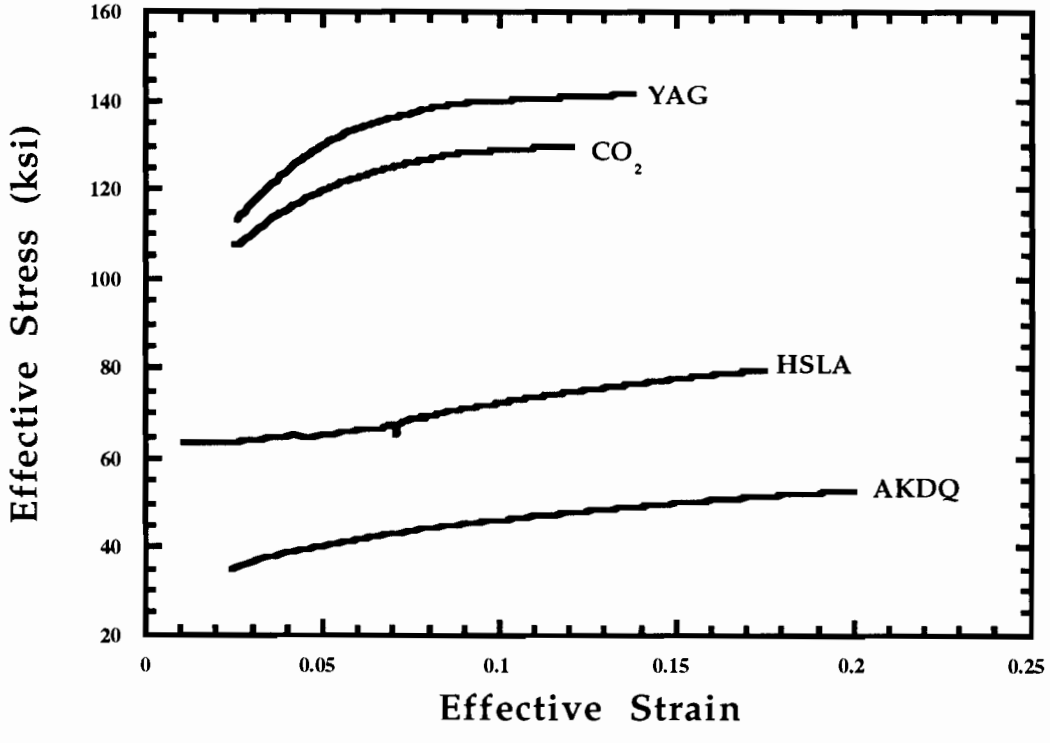

Figure 22. The calculated true stress strain curves for the CO_2 and Nd:YAG laser weld beads compared to the measured true stress-strain curves for the HSLA and AKDQ base materials.

$$\bar{\sigma} = K(1 - A\exp(-B\bar{\varepsilon})) \quad (3)$$

where $\bar{\sigma}$ is the effective stress, $\bar{\varepsilon}$ is the effective strain, K is the saturation stress level, and A and B are curve fit parameters. It is not clearly understood if the material actually follows this behavior, or if it is only a result of error incurred in the analytical method of determining the stress-strain behavior of the weld bead.

CHAPTER VI

ANALYSIS OF THE DOME TEST

1. Introduction

As mentioned at the end of Chapter 4, there is a need to understand what forming conditions induce weld movement and what variables influence it. This needs to be understood for two reasons; first, the failure mode could be dependent upon it (i.e. full dome stretch), and second, in applications where blanks are welded of different thicknesses, a step is required in the die to compensate. Therefore, it is important to know where the final position of the weld will be so the die can be designed accordingly. More fundamentally, simulation for purposes of die design and weld placement must be guided by the dominant mechanical failures. The FEM of the dome test was carried out completely on HSLA/AKDQ blanks.

Because of the vast number and uniqueness of each application of tailor-welded blanks, it is impossible to develop a simple analytical model that can predict the weld movement in every part. Therefore, numerical modeling must be utilized to be able to understanding and predict weld movement accurately.

In the next two chapters, we will establish FEM models that predict the weld movement in two geometries. In this chapter we will focus on predicting the weld movement in the dome test. This geometry features significant weld

movement and is easy to model, so it will be a good geometry to see if the model is accurate, and also to be able to run a sensitivity analysis to see what variables have a strong influence on the weld movement.

2. Experimental Verification of the Model

Figure 23 shows the mesh used for the full dome stretch simulation in the ABAQUS code. The mesh for the full dome stretch is 140 mm by 70 mm, with an axis of symmetry along the 140 mm axis. In order to simulate the dome test die, nodes around a radius of 60 mm were held fixed, to represent the clamping action. For modeling narrow widths, the blank size, mesh and boundary conditions were adjusted accordingly. An example of the LDH mesh is shown in Figure 24. The mesh is fine in the center so the correct width of the weld beads could be modeled. A 1 mm row of elements contained the laser bead mechanical properties (Chapter 5) for modeling a laser welded blank, while a 7 mm wide row of elements contained the mechanical properties of the mash seam beads for the mash seam blanks.

In all of the following simulations, the friction coefficient used for dry conditions is 0.25. This is based on numbers calculated by a simple friction testing apparatus at the Ohio State University [55].

Figure 25 compares the experimentally-measured weld movement in plane view compared to the simulated weld movement for the CO_2 laser and the unplanished mash seam blank for a full dome stretch. The experimental measurements of the weld movement were made using a traveling microscope, measuring the lateral position of the weld from the center line defined by the points where the weld was clamped in the lockbead. This was compared to the coordinates of the weld line taken from the ABAQUS output file. As one can observe, the weld movement prediction is very good.

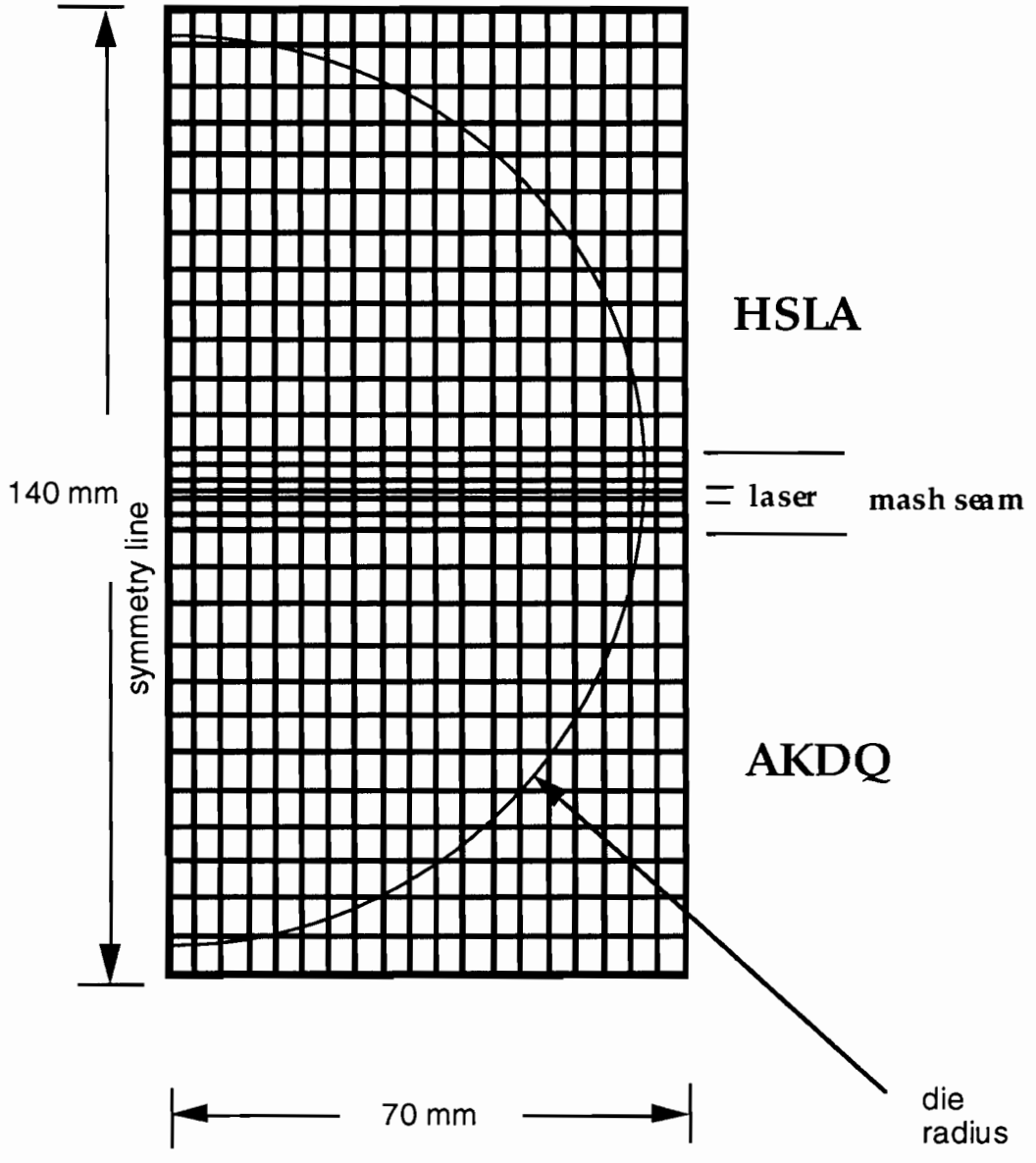

Figure 23. The mesh used in the ABAQUS finite element simulation for the full dome stretch.

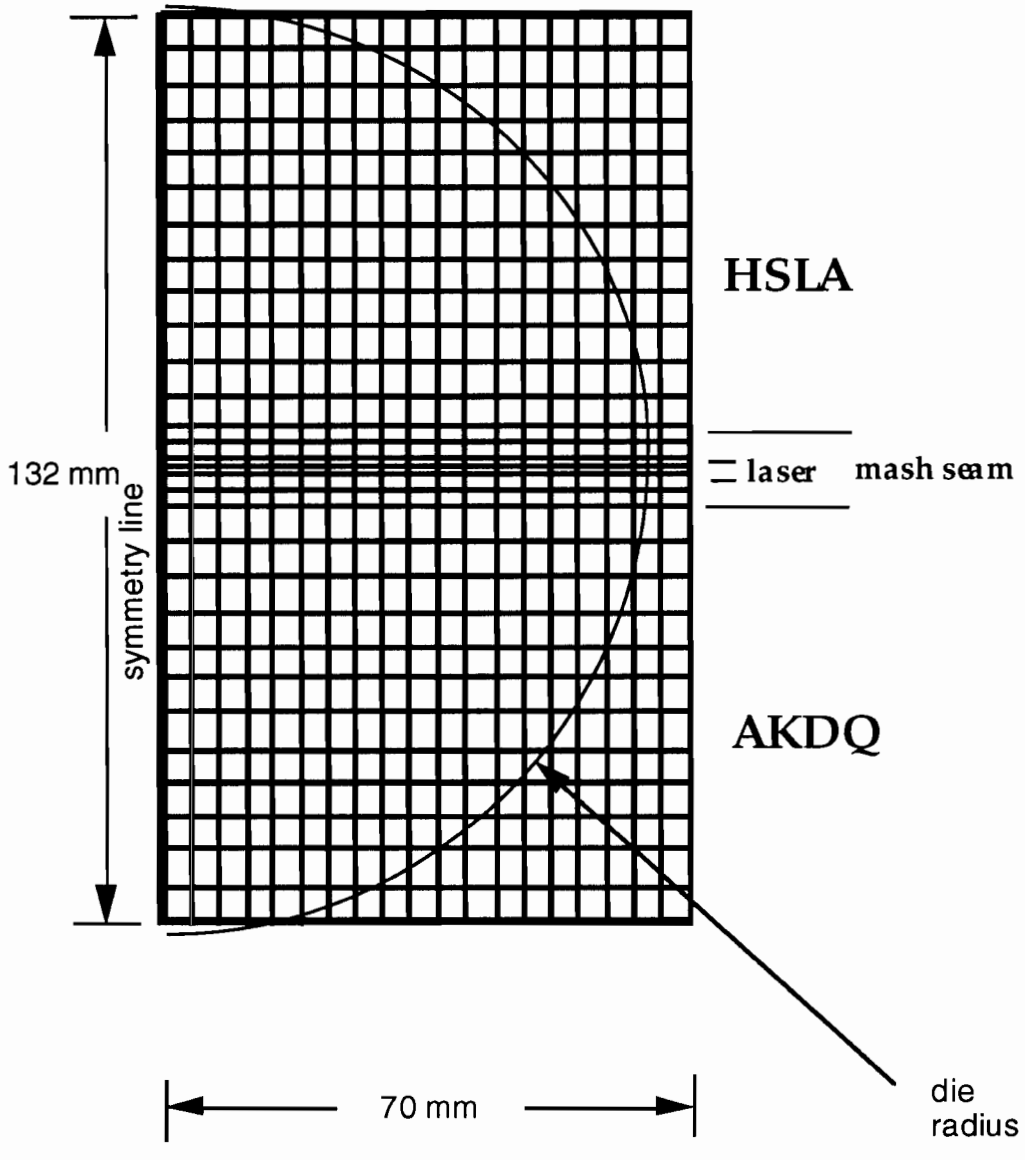

Figure 24. The mesh used in the ABAQUS finite element simulation for the LDH Test.

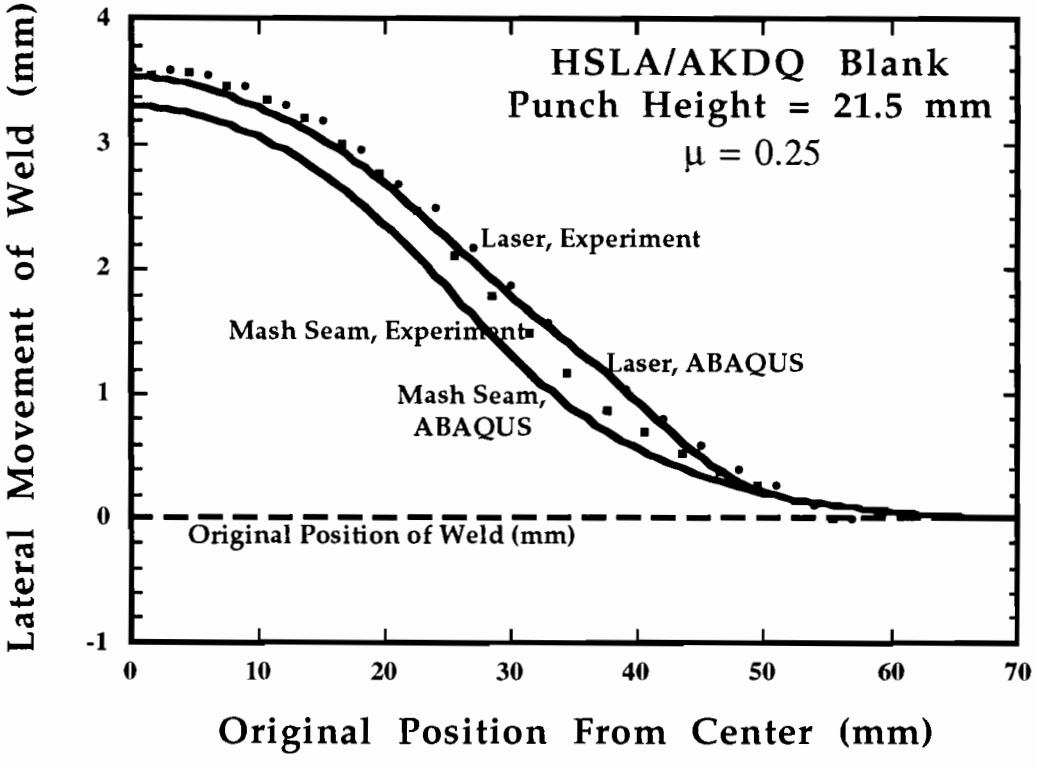

Figure 25. Experimentally measured weld movement of the mash seam and laser full dome stretch specimens compared to the ABAQUS simulations for HSLA/AKDQ blanks.

We have established that there is a reasonable correlation of the simulation to the experiment of the welded blank full dome stretch. From here we will investigate the influence of the global and local factors on the weld movement.

Ghosh [17] originally observed with the hemispherical stretch test that as the width of the blank is varied, the strain state in the material changes. This is because the force resisting the blank from drawing in the minor direction increases with increasing blank width. Therefore, comparing the model of the dome test for different width blanks to experiment would verify the model for a variety of loading conditions.

Figure 26 show the experimentally measured weld movement for a dome test specimens of 1", 2.5", 4", 5.25" and 7" width. As the specimen width increases, the weld movement becomes more severe. Therefore, as the boundary forces normal to the weld increases, the amount of weld movement increases as well. Figure 26 also shows each of the experimentally measured weld movement compared to the predicted weld movement using the ABAQUS model for the dome test. The ABAQUS model shows reasonable correlation to the experiment for each of the boundary conditions. A friction coefficient used was 0.25 for each simulation. This is a reasonable value for dry forming conditions [55], and the final weld location was not strongly dependent upon the friction coefficient.

Comparing Figures 25 and 27 results in an interesting observation. Figure 25 shows the ABAQUS-predicted weld movement in the full dome stretch for the mash and the laser welded specimens. Under these boundary conditions, there is little difference in weld movement between the mash seam and the laser weld. However, there is a significant difference between the two weld types for the LDH Test (Figure 27). The mash seam weld did not move as much as the laser

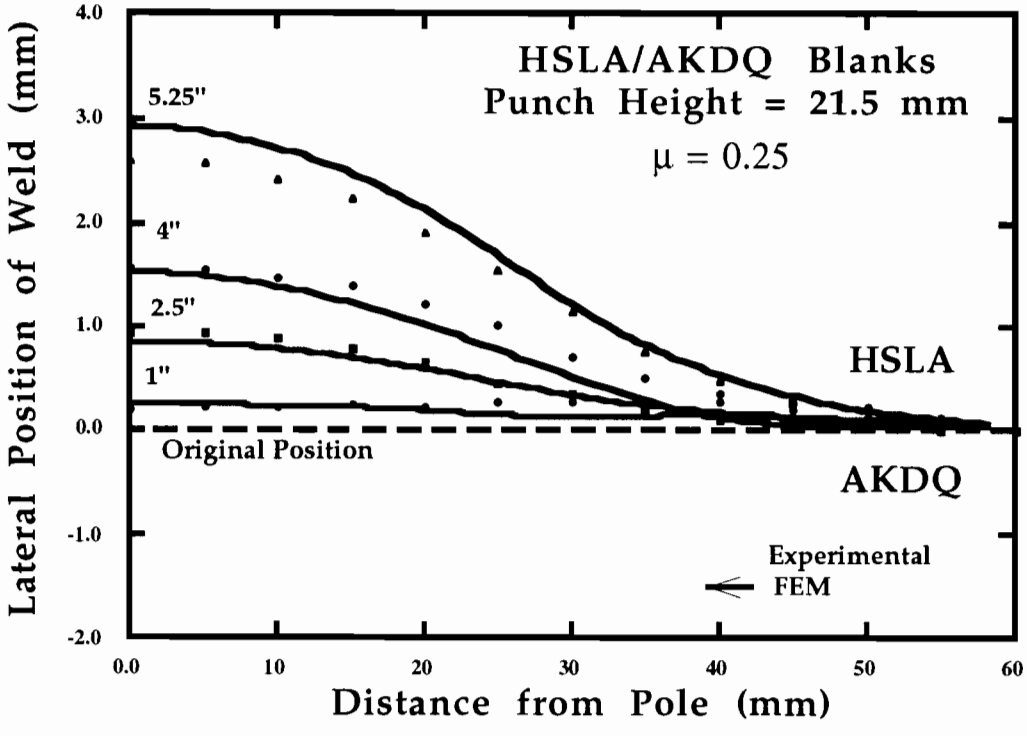

Figure 26. ABAQUS simulated weld movement compared to experimentally measured values for a number of different width blanks on the Dome test for HSLA/AKDQ blanks.

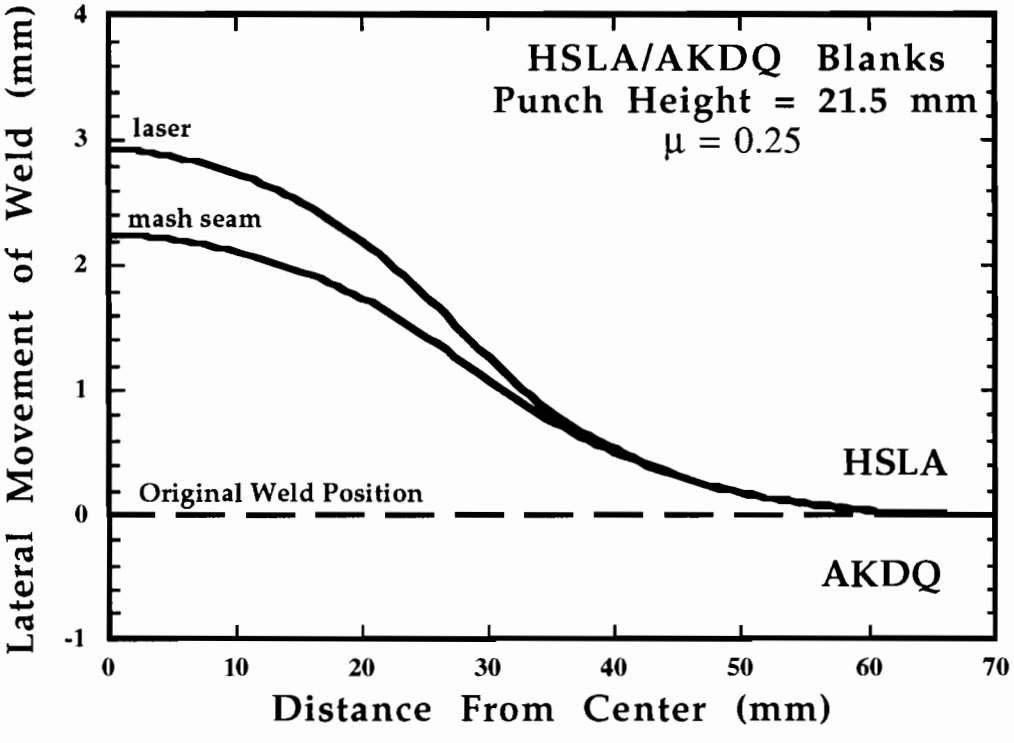

Figure 27. ABAQUS simulated weld movement for the laser and mash seam welded blanks for the LDH test for HSLA/AKDQ blanks.

weld under these boundary conditions. Therefore, there could be a difference in formability between the mash seam and the laser welded blank under certain boundary conditions. Unfortunately, this could not be verified with experiments because of the aforementioned problems with the mash seam LDH experiments.

A similar set of experiments and simulations were run for welded blanks with the same parent materials. Laser welded samples of 0.8 mm to 0.8 mm AKDQ were varied in width for 1" to 7" and tested to the same height of 21.5 mm and the weld movement was measured. Since the geometry is symmetric around the weld line, there was no observed weld movement in the simulation. Experiment showed the same trends (Figure 28) with the weld in all cases moving no more than 0.25 mm. Hence, the model also accurately predicted this behavior.

Another important aspect of this data is that this can give an idea of the amount of error involved in measuring the amount of weld movement. Since the amount of weld movement should be zero, the amount the weld movement is off in these measurements is the experimental error in measuring the amount the weld moves. From these 4 sets of data, it is found that the average error in measurement is ±0.25 mm. Therefore, any discrepancy in weld position less than this amount is unidentifiable in a research laboratory, let alone a press shop floor. For example, there is slight error in the prediction of the mash seam weld movement in Figure 25. However, the difference between experiment and FEM is only 0.25 mm, so therefore the prediction may fall within experimental error.

3. Variables Influencing Weld Movement

In the previous section it was shown that the FEM simulation predicted the amount of weld movement in the dome test accurately. Also, from the varying blank width and the 0.8/0.8 mm experiments, it was found that both a

force normal to the weld and the base materials of different load bearing capacities are needed for weld movement. In this section, we will investigate with the experimentally proven model the other variables that may influence weld movement besides the mechanical properties of the base materials and the boundary forces.

3.1 Friction

Figure 29 shows the influence of the global friction coefficient on the weld movement for the full dome stretch sample as predicted by simulation. The "global" friction is defined as the friction condition of the entire blank. The friction coefficient is varied between 0.1 and 0.3, which is a realistic range of

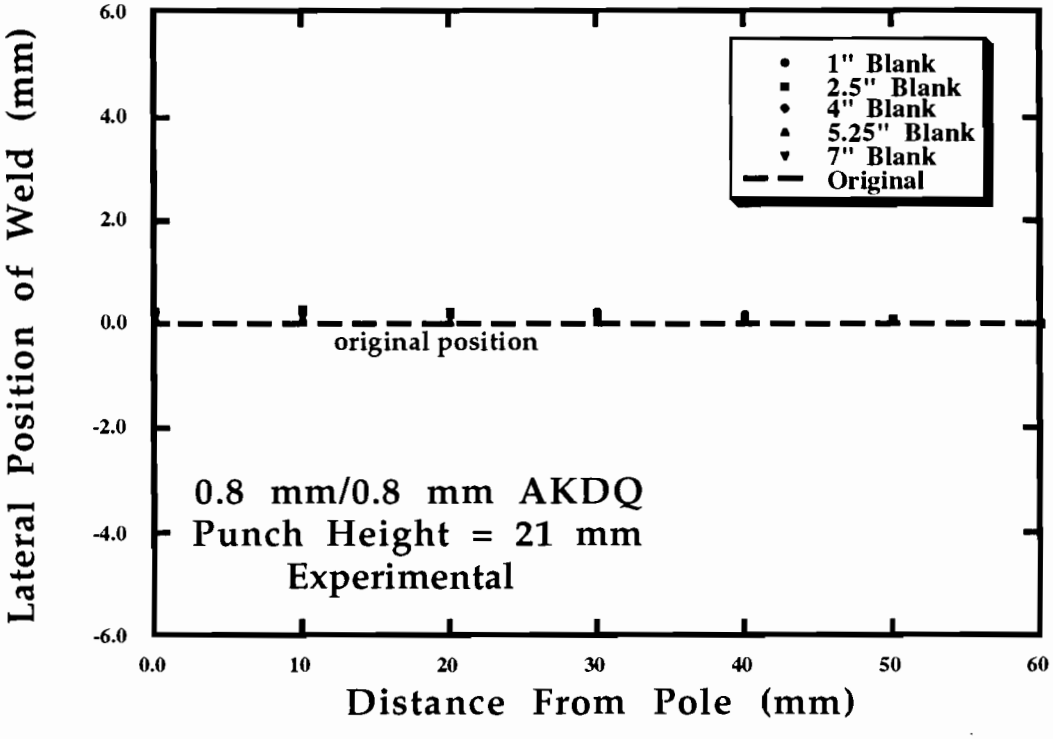

Figure 28. Experimentally measured weld movement for 0.8 mm/0.8 mm AKDQ for different widths on the dome test.

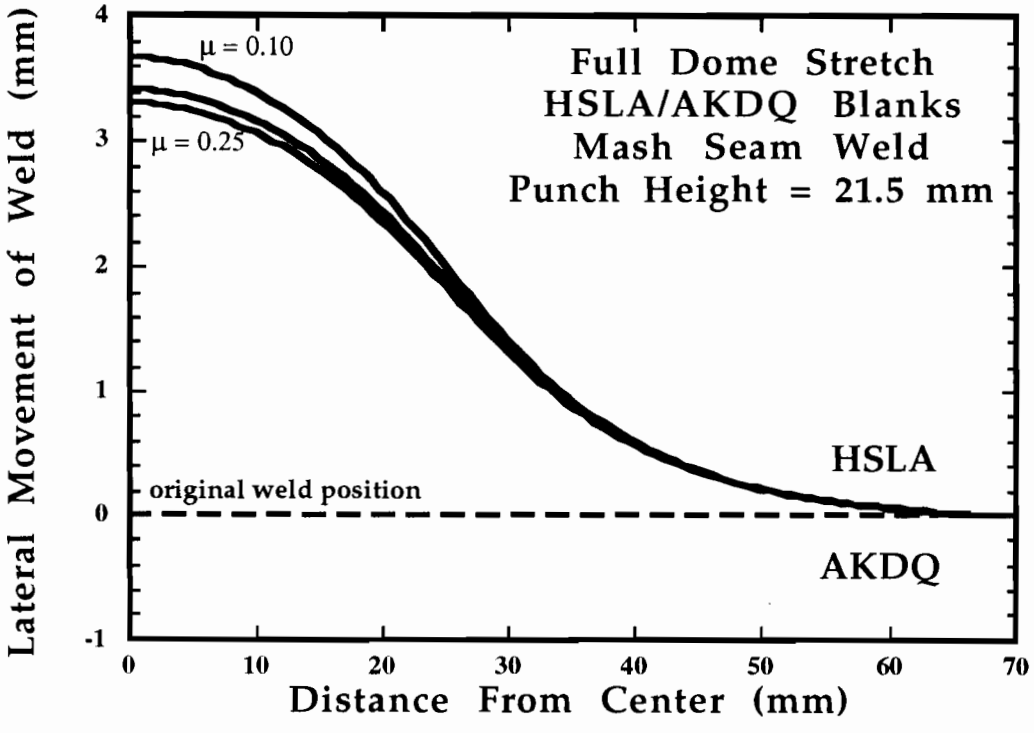

Figure 29. The ABAQUS simulated influence of the global friction condition on the total weld movement of the laser weld bead on the full dome stretch test for HSLA/AKDQ blanks.

friction coefficients in an actual forming operation for different lubrication conditions. For the full dome stretch, one can see that the amount of weld movement depends slightly on the friction coefficient. As the friction increases, the amount of weld movement decreases. Therefore, for the full dome stretch, the influence of lubrication has been reversed. If one increases the lubrication, and hence decreases the coefficient of friction, the weld movement will be more severe, resulting in a lower punch travel to failure. Usually lubrication and low friction results in improved formability. Figure 30 shows the simulated influence of the global friction coefficient on the weld movement for the LDH samples. The LDH is less sensitive to the global friction in terms of weld movement than is the full dome stretch.

3.2 Weld Mechanical Properties

The different welding processes produce different microstructures for each of the weld beads, and these different structures are characterized by different stress-strain responses. In this section the goal is to determine if the hardening behavior of the weld material has a significant influence on the weld movement. The approximate hardening laws for the laser and exact stress-strain relationships for the mash seam welds that were established in Chapter 5 will be used in the simulation.

The first issue addressed is whether it is necessary to include the properties of the weld for the laser weld in the simulation of a tailor-welded blank. The weld zone of a laser weld is small (approximately 1 mm wide) in relation to the rest of the blank, so it seems likely that the weld can safely be neglected. One simulation contained a row of 1 mm wide elements that possessed the properties of the weld bead between the two sets of elements that represented the parent materials, the other did not. The results are shown in

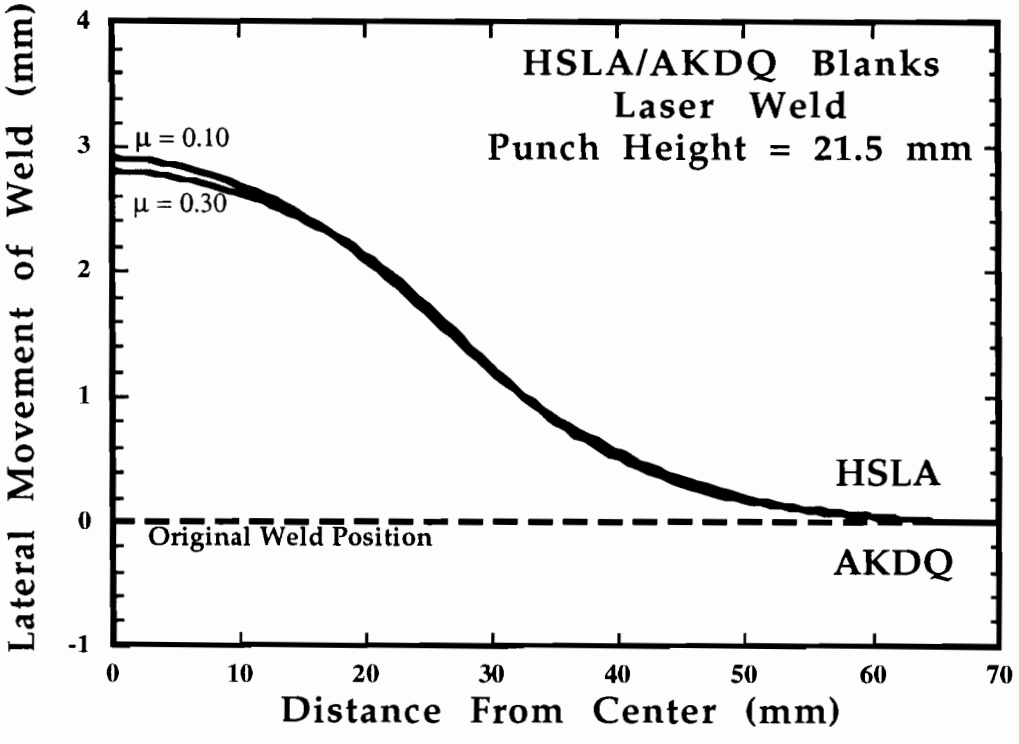

Figure 30. The ABAQUS simulated influence of the global friction condition on the total weld movement of the laser weld bead on the LDH test for HSLA/AKDQ blanks.

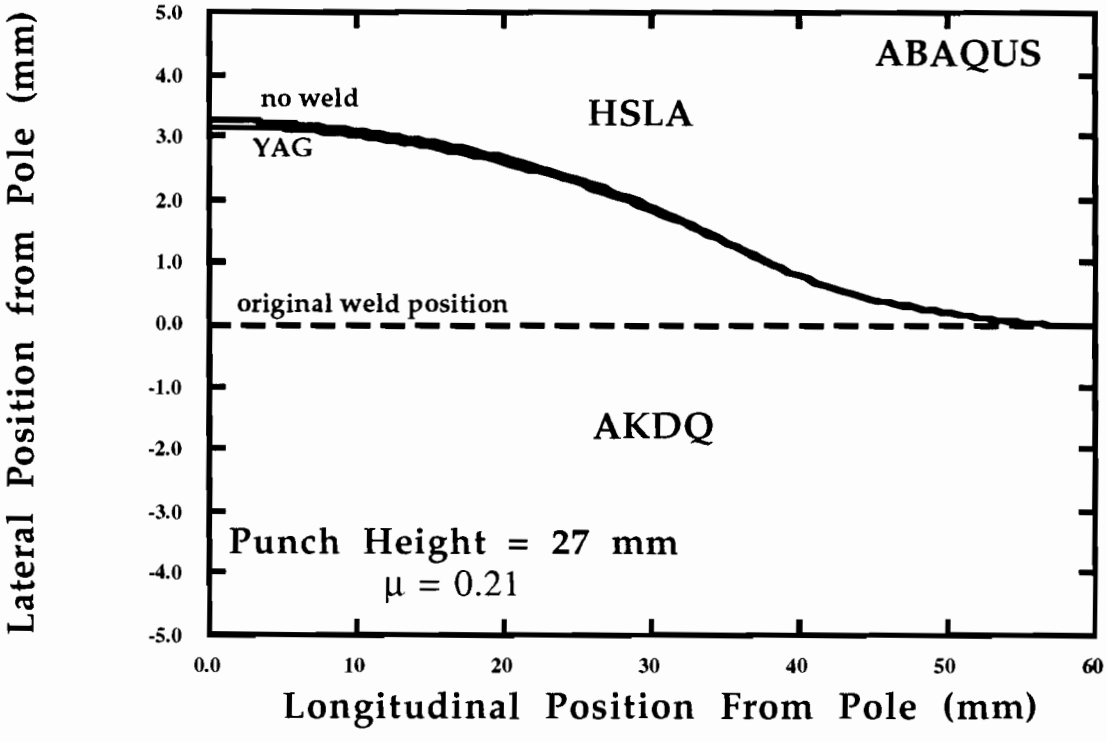

Figure 31. The ABAQUS simulated weld movement for the laser welded blank and a blank simulated with no weld zone for HSLA/AKDQ blanks.

Figure 31. There is a slight difference in the weld movement when the weld bead is taken into account, but not enough to justify determining the laser weld bead hardening laws.

As mentioned before, the mash seam weld bead is significantly larger than the laser weld bead. Therefore, it cannot be assumed that the properties of the mash seam bead can be neglected. The bead represents a significant amount of material, so its properties could influence the weld movement. Hence, we will model the mash seam blanks using the experimentally determined hardening laws for the three different types of weld beads and the correct mash seam weld geometry. This will give a good indication of the importance of weld mechanical properties because of the different mash seam welds provide a wide variety of weld properties.

Figure 32 shows the weld movement for the different mash seam types and no weld zone in a full dome stretch. There is no real difference in weld movement between weld types, and only a difference compared to the simulation assuming no weld zone. Hence, under these boundary conditions, the mechanical properties of the weld are insignificant. Figure 33 shows the same simulations for the different weld properties for the LDH test. The results are slightly different from the full dome stretch, as there is a slight difference in the amount of weld movement for the cold planished mash seam compared to the unplanished and the hot planished, and a significant difference for the simulation run with no weld properties.

3.3 Weld Geometry

Figure 25 shows the difference between the simulated weld movement between a mash seam weld and laser weld for a full dome stretch. The difference is small but significant. Mechanical properties of the weld do not influence weld

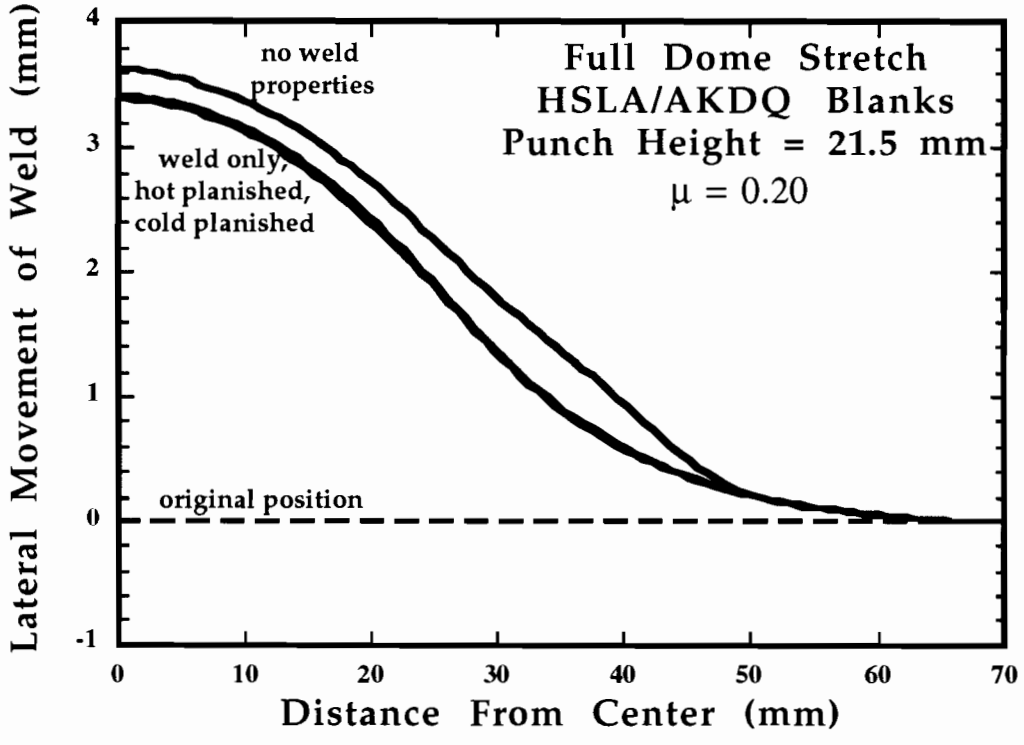

Figure 32. ABAQUS simulated weld movement for the unplanished, cold planished and hot planished welds for the full dome stretch for HSLA/AKDQ blanks.

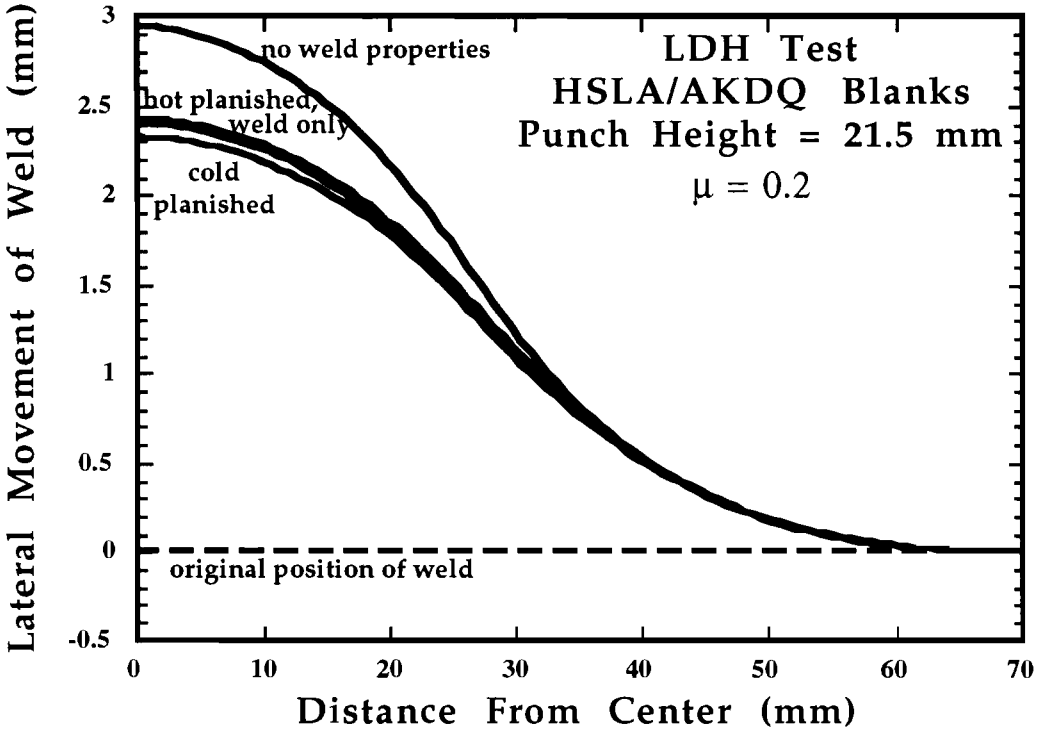

Figure 33. ABAQUS simulated weld movement for the unplanished, cold planished and hot planished welds for the Limiting Dome Height test for HSLA/AKDQ blanks.

movement for a full dome stretch, as shown in the previous section. There was no variation in the friction coefficient between the mash seam and the laser weld simulations in Figure 25, so the only variable that can account for this slight difference is the weld geometry. The mash seam weld bead possesses a larger volume of material.

3.4 Weld Friction

The local friction of the weld is not an issue in laser welded blanks because the weld bead is flush with the base materials. Therefore, the contact of the laser bead is small or even non-existent. The mash seam bead, on the other hand, protrudes from the surface of the base materials. Also, each of the different processes of the mash seam weld (i.e planishing, hot planishing or no planishing) produces a different surface roughness. Therefore, it is necessary to see how this difference in friction will influence the weld movement and hence the formability.

Not only is the surface roughness different, but also the contact is quite different. The protruding weld bead results in no contact of the base material at all in the immediate vicinity of the weld. However, in this simulation, we will lump both friction and contact into the friction coefficient. The ABAQUS model uses shell elements, so it is impossible to model the different contact. For this model, the friction coefficient defining the interface element properties associated with the weld bead will be varied from simulation to simulation, while the friction coefficient for the rest sample will be held constant.

Figure 34 shows the influence of variations in the local friction coefficient on the weld movement of an unplanished mash seam blank. There is a significant difference in weld movement for the full dome stretch over this range of local friction coefficients associated with the weld. Figure 35 shows that the

local friction coefficient does not have quite as strong effect on weld movement as does the global friction coefficient. However, the local friction coefficient does have a much stronger influence on the weld movement than does any other local property (i.e. weld mechanical properties, weld geometry) for a full dome stretch.

The influence of the local friction on the weld movement is much greater in the LDH Test than it is in the full dome stretch (Figure 34). In fact, the influence of the local weld friction coefficient in the LDH Test is much more significant than it is for the global friction coefficient. However, neither friction type shows an influence outside experimental error.

4. Summary of Weld Movement

Using the experimentally verified model that predicts weld movement in the dome test, the factors that influence weld movement have been identified. First and foremost, the most important variable that determines weld movement is the difference in the load bearing capacity of the base materials. Weld movement occurs when the material is stretched normal to the weld. If there is a difference in load bearing capacities of the two materials, the weaker material will stretch the most, and the weld will move in the direction of the stronger material. This brings up the second most important factor in determining weld movement: the boundary forces. A force must be applied normal to the weld in order to have weld movement. If there is no boundary force normal to the weld, i.e. *The OSU Formability Test*, then there will be no weld movement. Also, as this force increases, i.e. LDH to full dome stretch, the amount of weld movement will increase (Figure 26). The difference in the strength of the base materials will enhance the change in weld position, even under symmetrical loading conditions. In the case where the dome test stretched a laser welded sample that

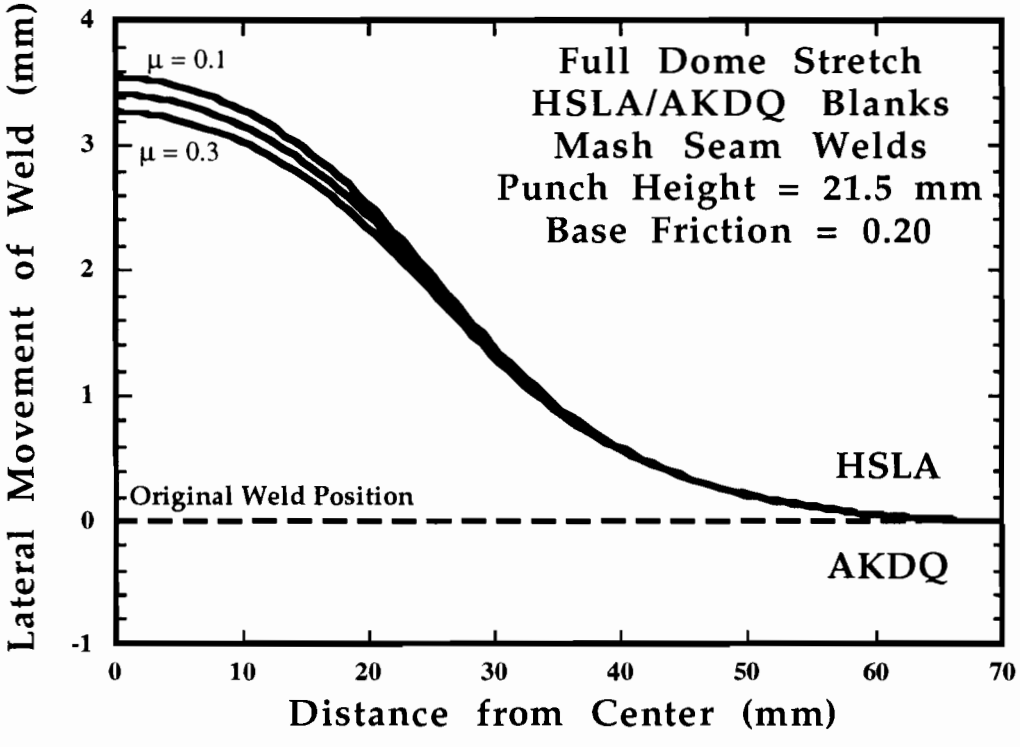

Figure 34. The ABAQUS simulated influence of the local friction of the mash seam bead the on weld movement in the full dome stretch for HSLA/AKDQ blanks.

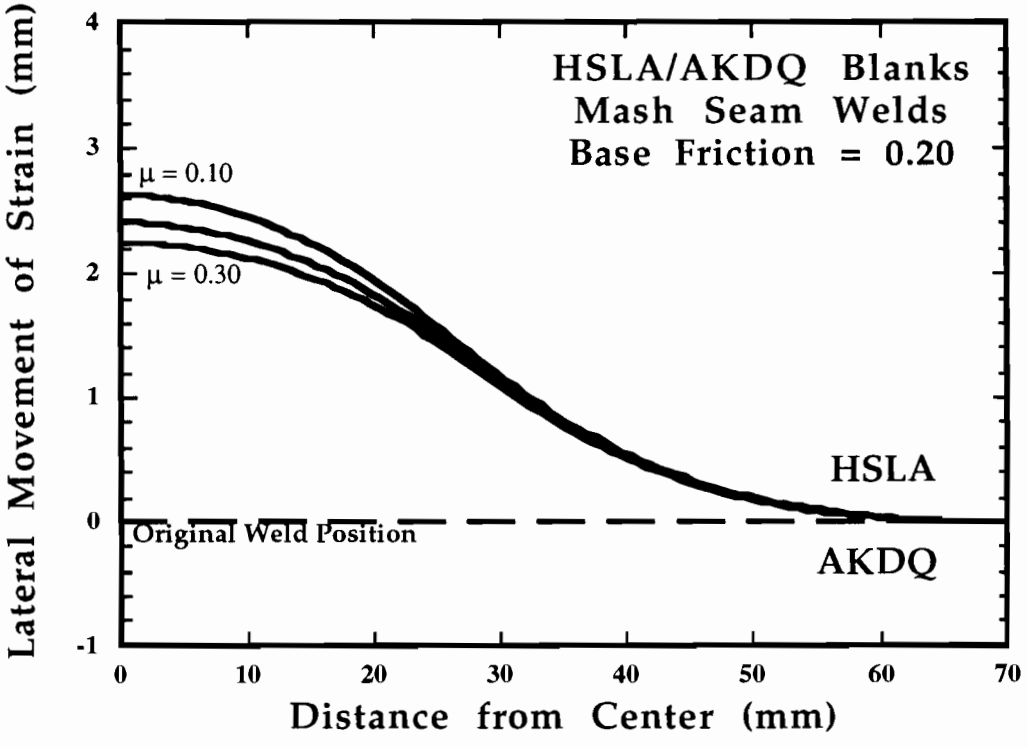

Figure 35. The ABAQUS simulated influence of the local friction of the mash seam bead the on weld movement in the Limiting Dome Height test for the HSLA/AKDQ blanks.

had no difference in thickness or strength of the base materials, regardless if it was a full dome stretch, or a plane strain LDH, the weld movement is zero.

The other properties, i.e. friction or those properties associated with the weld bead i.e. the weld geometry, friction or mechanical properties, FEM can predict the general trends that each of these variables will influence the amount of weld movement. However, in light of the results extracted from Figure 28 about error in weld movement measurement, the difference in movement as a result of these variables is negligible.

CHAPTER VII

THE FORMING SIMULATION OF AN AUTOMOTIVE FENDER WITH A TAILOR-WELDED BLANK

1. Introduction

In the previous chapter, the ABAQUS finite element model was able to predict the weld movement in the Dome test with reasonable accuracy. In this chapter, a much more complicated geometry, the scale fender die on the *Hydraulic Forming Simulator*, will be analyzed. This tool is fully three dimensional and features stretch-draw boundary conditions. Experiments will be run with the weld located at different positions, using different weld types and different lubrications to see how each influences formability. These forming conditions will be modeled using the SHEET-3 code to see if it can accurately predict the weld movement. Only the HSLA/AKDQ blanks were analyzed.

2. Experimental Analysis

2.1 Influence of Weld Position

It was pointed out by General Motors die engineers that this tool has a shape similar to a front door inner, which is a common application for the use of a welded blank. Therefore, we will attempt to simulate this same weld positioning in our scale fender die as in the door inner. We will place the weld normal to the long axis of the part (Figure 36). The actual position of the weld

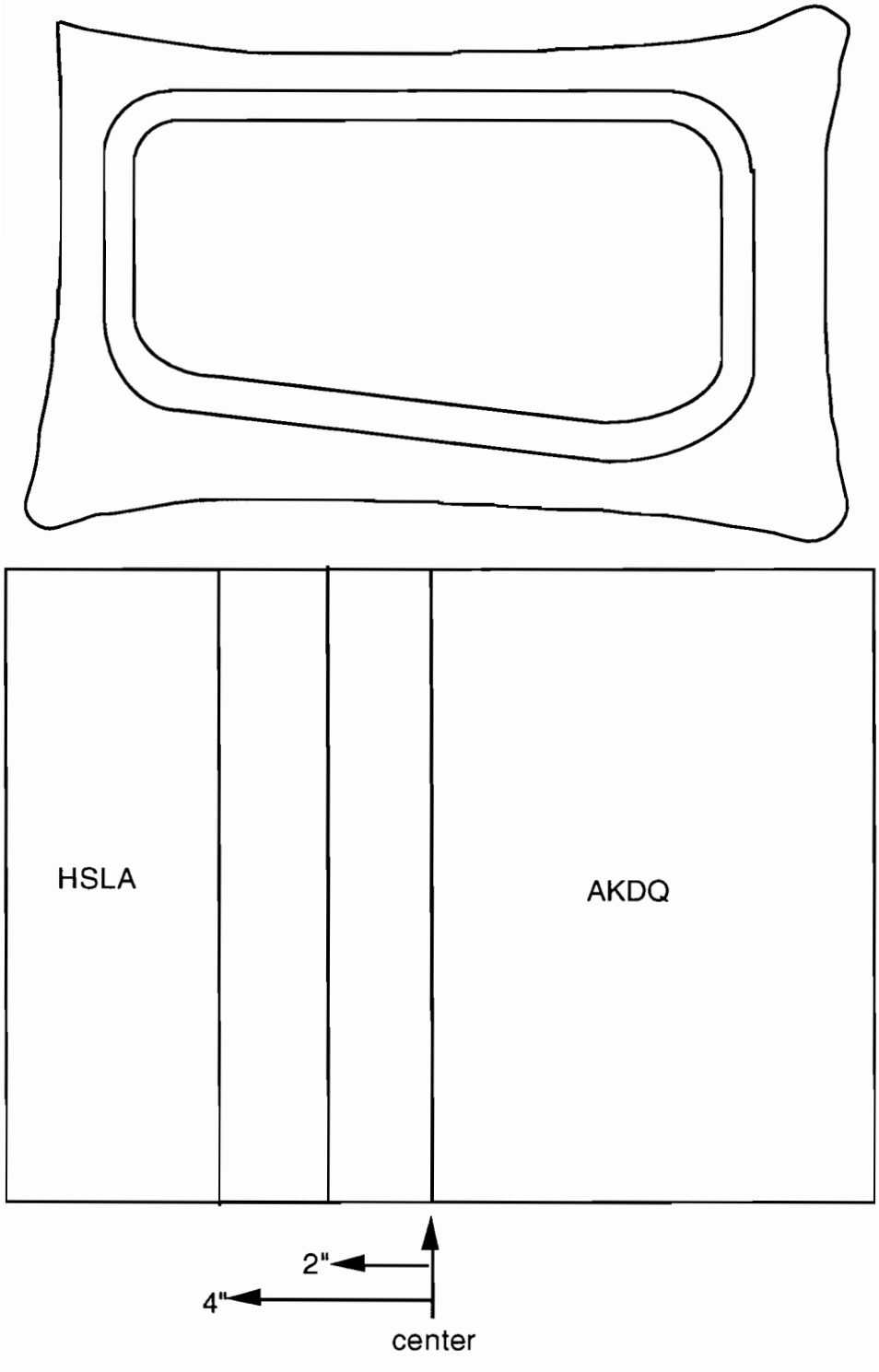

Figure 36. The proposed weld locations for the scale fender die.

will be varied, starting at the center of the punch and moving the weld line closer to the sloped end. The samples will be tested to failure in order to find what is optimum position of the weld line for greatest formability.

The failure height as a function of weld position is shown in Figure 37. The actual failure heights are shown in Table 10. The failure heights reported are the average of three tests run under the same conditions. The failure height was fairly constant, but the failure mode changed significantly. When the weld is located between the center of the blank and 2.75" from the center, the failure occurs at the punch corner in the HSLA steel. When the weld is located between 2.75" from the center and 4" from the center, the failure is dominated by weld movement, and the failure occurs in the AKDQ, parallel to the weld line. As the weld line moved closer to the edge of the punch, the weld line movement becomes significant in determining the failure mode.

2.2 Friction

Since weld position did not have a strong influence on the overall formability, we will now investigate the effect of increasing the lubrication. In order to reduce friction as much as possible, the specimens were coated with a dry film lubricant provided by D. A. Stuart & Co. [54]. When the specimen was placed in the tool, polyurethane plastic sheets (garbage bags) were placed between the blank and the tool on both sides. This produced a highly lubricated condition.

Table 10 shows the punch travel of the tool for the blanks where the weld was 2", 3" and 4" from the center of the blank for the fully lubricated condition. Decreasing the friction resulted in a huge increase in formability. The 2" and 4" samples made a full part (57.5 mm) with some wrinkling, while the 3" sample was just short of making a full part. The 3" sample failed in the base AKDQ

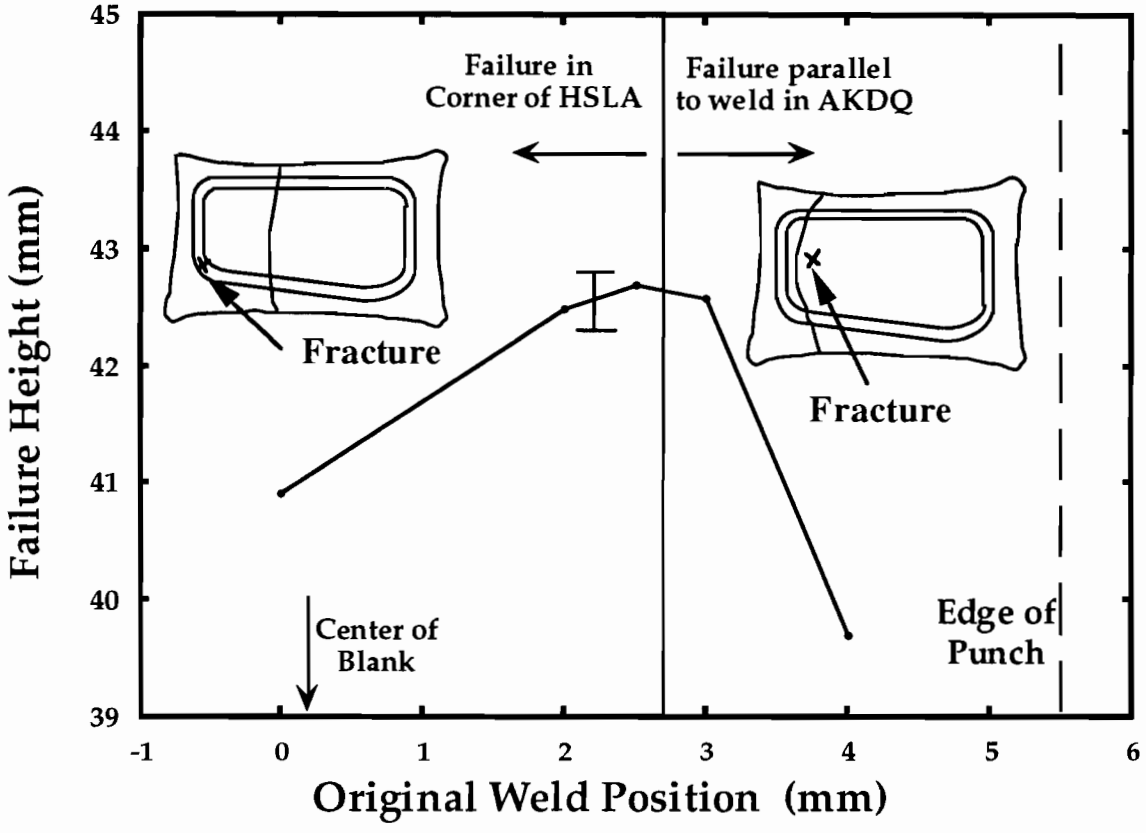

Figure 37. The failure height of the tailor-welded blank in the scale fender die as function of the original position of the weld

Table 10. Failure heights of HSLA/AKDQ blanks for scale fender die for different forming conditions.

	Failure Height (mm)		
Position of Weld	2"	3"	4"
Laser weld, no lube	43.0±0.5	43.0±0.4	40.0±0.6
Full Lubrication	57.0±0.3	54.0±0.7	57.0±0.5
Unplanished Mash Seam	44.0±0.5	N/A	N/A
Cold Planished Mash Seam	46.0±0.4	N/A	N/A
Hot Planished Mash Seam	44.0±0.6	N/A	N/A

material parallel to the weld, as a result of severe weld movement. Either way, the increase in lubrication resulted in much improved formability.

2.3 Weld Type

In Table 10 the failure heights for the three mash seam welds are compared to the laser-welded sample when the weld is located 2" from the center. This was the only weld position that could be tested in the scale die fender for the mash seam welds because of limitations of the initial blank size received from the supplier. The failure modes were all the same; each failed at the corner of the punch in the HSLA material. It is interesting to note that all

three mash seam weld types have higher failure heights than the laser, and hence the ductility of the weld has no real influence on the overall formability of a blank in the scale fender die. The fact that the cold planished mash seam welds had the worst ductility did not affect the formability of the entire blank.

It is not clear why the mash seam welded blanks had a greater formability than the laser blanks. A possible explanation is the blank holder force was not as great on the HSLA for the mash seam blanks. The mash seam welds were thicker than the base materials and were not compensated for in the dies. Therefore, the majority of the force would be applied to the mash seam weld in the binder, with much less force applied to the base materials. In this case, the HSLA would be able to draw into the die cavity more easily, reducing the stretch in the HSLA, and improving the formability.

The blank shape for the cold planished mash seam weld is shown in Figure 38.

3. Analysis of Weld Movement

We have observed different failure modes for different weld positions and lubrication conditions. Some are directly related to the amount the weld actually moves. In this section we will briefly investigate the experimentally measured weld movement for different weld positions, different lubrication conditions, and different weld types.

Five specimens under different forming conditions were tested to punch heights just below the experimentally observed failure height corresponding to their weld position under dry forming conditions, i.e. a blank with the weld located 4" from center failed at 40 mm under dry conditions, so any blank with the weld located 4" from center was tested to 38 mm. The five forming

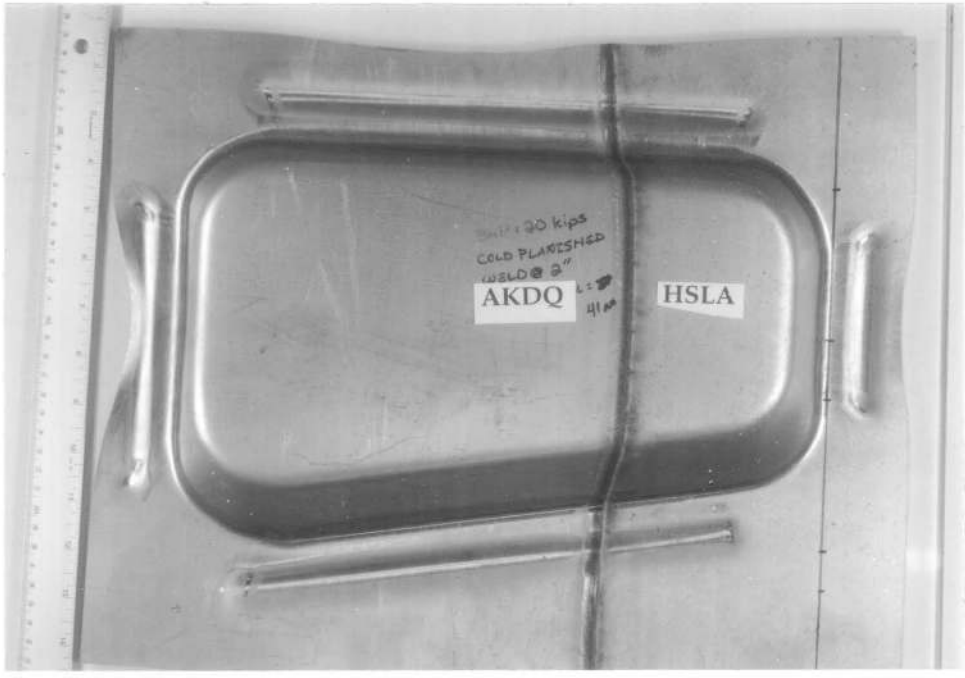

Figure 38. A photograph of the deformed blank for a cold planished HSLA/AKDQ tailor-welded blank on the scale fender geometry.

conditions were:

1.) Laser weld 4" from center line, no lubrication, punch height = 38 mm
2.) Laser weld 4" from center line, lubrication, punch height = 38 mm
3.) Laser weld 2" from center line, no lubrication, punch height = 41 mm
4.) Laser weld 2" from center line, lubrication, punch height = 41 mm
5.) Cold planished weld 2" from center line, no lubrication, punch height = 41 mm

The final weld line position was measured from a line drawn on the blank where the material first started to enter the die cavity. This line can be seen on the right hand side of the cold planished blank (Figure 38). This was a common reference point for all experimental forming conditions, and is also a reference point for the computer simulations.

Figure 39 shows the experimentally measured final weld line position compared to the original position when the weld was located 4" from the center, formed under dry conditions. As one can see, the weld on top of the punch moves significantly (14 mm), which would eventually lead to the tearing of the AKDQ parallel to the weld bead. What is interesting, however, is that the weld line movement is not that much less for lubricated conditions compared to dry (Figure 40). At the most, the lubricated weld moved 2 mm less than the dry formed blank. Therefore, the difference in formability between a lubricated sample and a dry sample doesn't appear to be the lubricant's influence on the weld movement.

Figure 41 shows the weld movement for a blank with the weld located 2" from the center formed under dry conditions. The weld movement is much less in this case (8 mm) than it is for the weld located 4" from center (14 mm). This would explain the difference in failure modes between the two locations. The

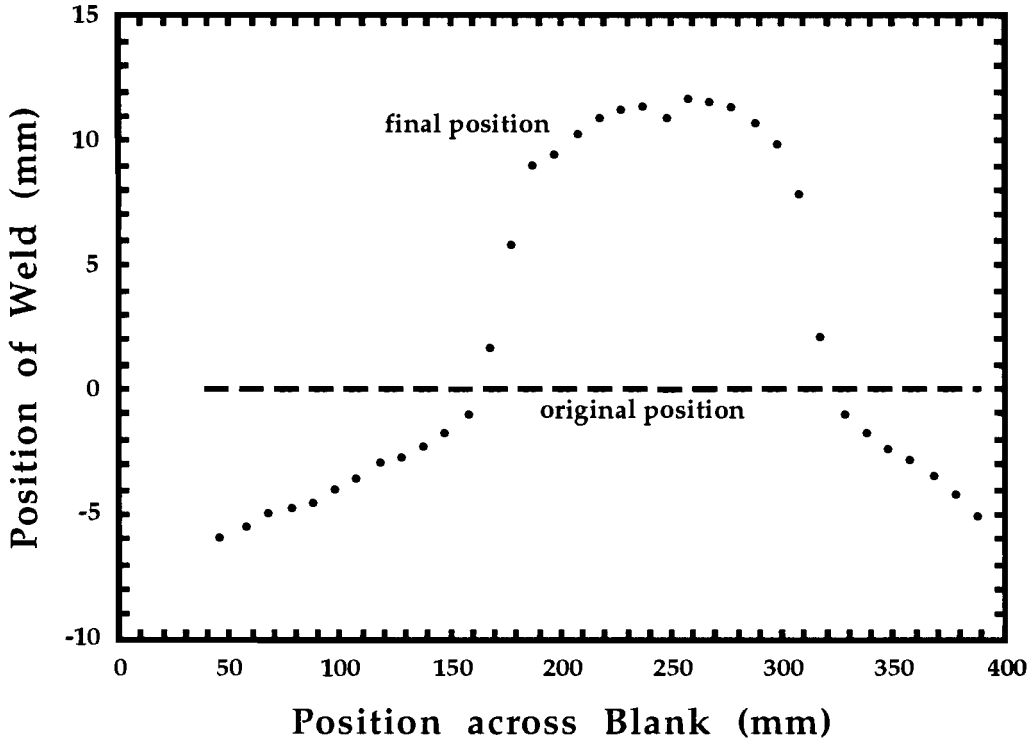

Figure 39. The experimentally measured weld movement for a HSLA/AKDQ laser welded blank with the weld located 4" from center, dry conditions, punch height = 38 mm.

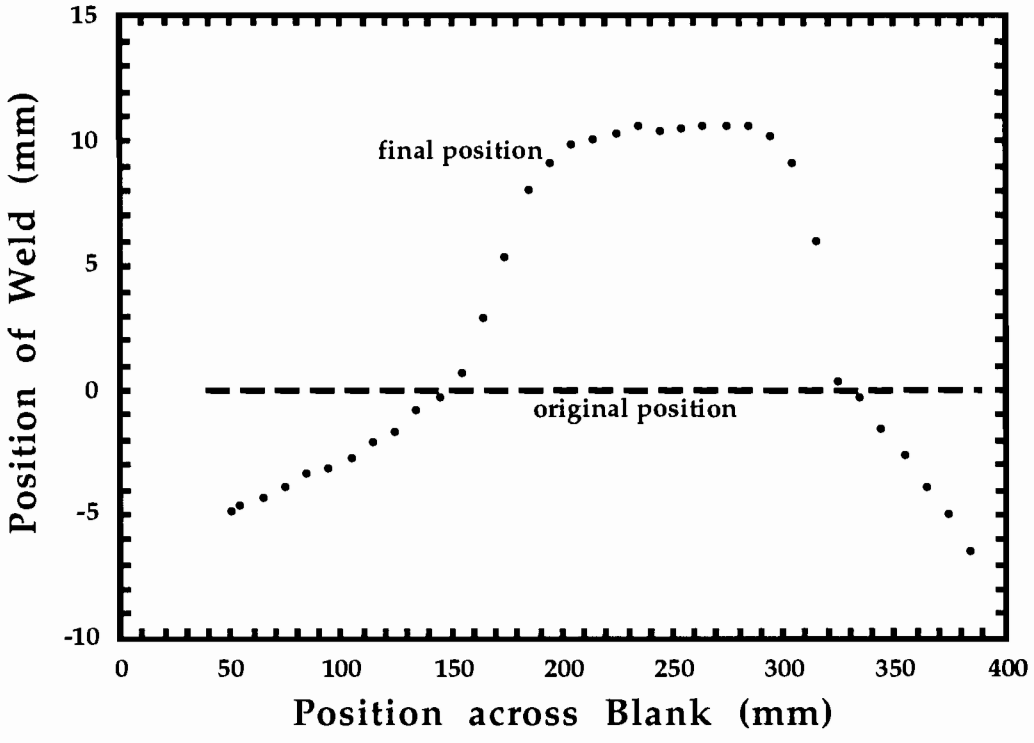

Figure 40. The experimentally measured weld movement for a HSLA/AKDQ laser welded blank with the weld located 4" from center, lubricated conditions, punch height = 38 mm.

weld movement is less severe, and therefore wouldn't force the AKDQ to fail parallel to the weld. Again, the lubrication has very little influence on the weld movement (Figure 42). The weld movement was approximately (8 mm), just as in dry conditions.

Figure 43 shows the weld movement of the cold planished mash seam weld located 2" from center. The weld movement is almost the exact same as it is for the laser welds. Therefore, as it was observed in the dome test, the difference in formability between a mash seam and laser weld blank seems to be small. The local properties of the weld seem to be insignificant in the overall forming.

4. Finite Element Analysis

In the finite element analysis of the scale fender die, the main focus will be on attempting to predict the weld line movement in the blank. As shown in the previous section, the amount of weld movement in the scale fender die was different for different weld locations in the blank. This different weld movement influenced the failure mode. Therefore, being able to predict this movement is very important for blank design and die design.

4.1 The model

The in-house OSU code SHEET-3 was used for this geometry. The ABAQUS program was unable to converge for a simple u-channel draw, so it was assumed it would not converge for something as complex as the scale fender geometry. A representative mesh is shown in Figure 44, displaying the two materials and the weld line. The mesh featured 800 elements and 441 nodes. The properties of the two base materials were represented by internally modifying the program to allow different elements to possess different hardening behavior. Laser welded blanks were modeled and the properties for the weld bead were neglected. Mash seam welds were not modeled because the aspect ratio of the

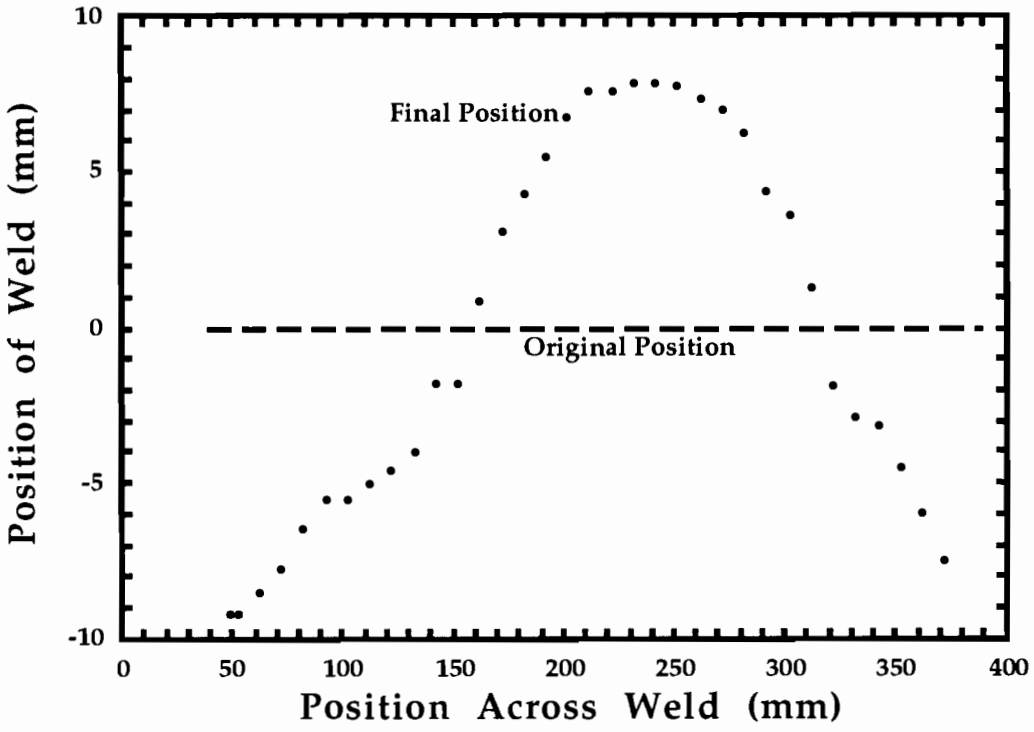

Figure 41. The experimentally measured weld movement for a HSLA/AKDQ laser welded blank with the weld located 2" from center, dry conditions, punch height = 41 mm.

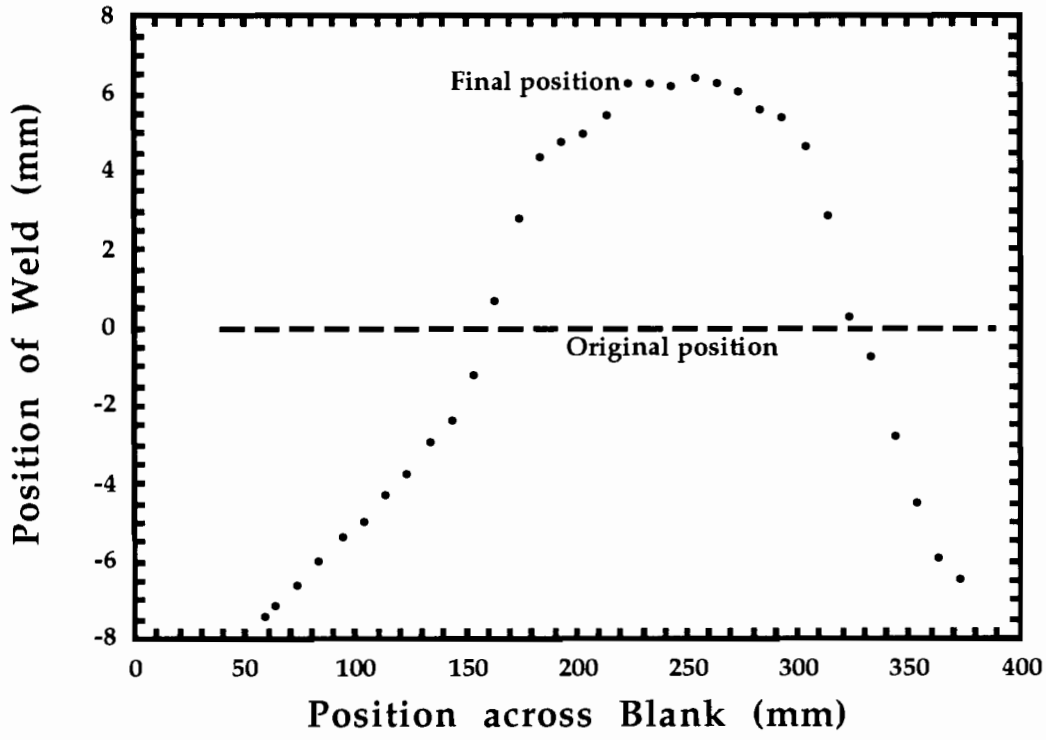

Figure 42. The experimentally measured weld movement for a HSLA/AKDQ laser welded blank with the weld located 2" from center, lubricated conditions, punch height = 41 mm.

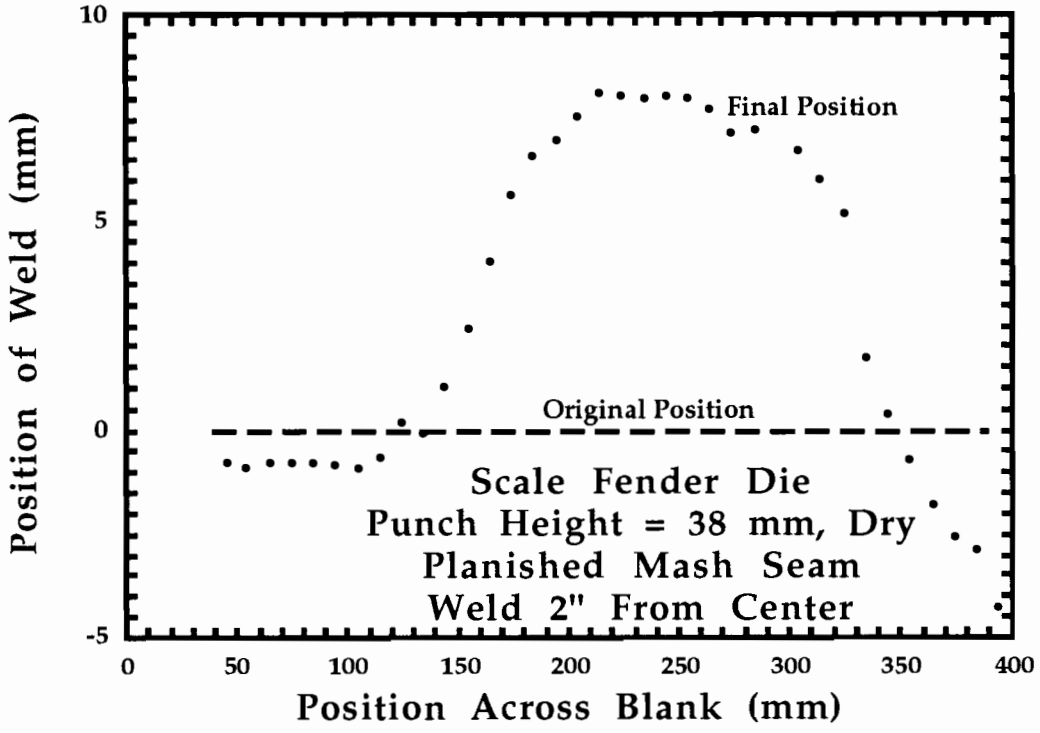

Figure 43. The experimentally measured weld movement for a HSLA/AKDQ cold planished mash seam welded blank with the weld located 2" from center, dry conditions, punch height = 41

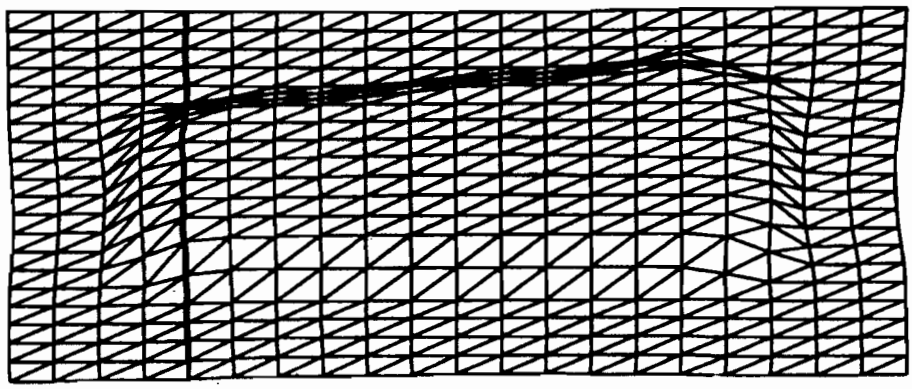

Figure 44. The SHEET-3 mesh in the simulations of the scale fender geometry.

narrow weld bead elements caused numerical instability and hence divergence. The friction coefficient was chosen to be 0.25 for the dry condition and 0.10 for the heavily lubricated condition, based on friction results done at Ohio State [55]. The boundary forces were initially assumed to be uniform around the blank and a direct function of the blank holder pressure, friction and blank contact area. The calculation for this is shown in Appendix C. However, these conditions did not result in good correlation to experiment (Figure 45). This tool has been simulated before [32] and has shown a reasonable correlation to experimental results, so the problem does not lie in the tool model or mesh. Since we have accurate measurements of the plastic response of the material, the only other two variables that could be causing problems would be the friction or the boundary forces. Figure 46 shows the difference in weld movement for a reasonable variation in friction for the lubrication conditions. The friction coefficient does have some effect on the weld movement, but clearly not enough to make up for the discrepancy between the experiment and simulation.

Therefore, the error must lie in the boundary forces. As the experimental conditions are examined more closely, it is found that the use of a constant boundary force model all around the blank is unreasonable. First, there is a slight difference in thickness between the HSLA and the AKDQ. The difference is 0.3 mm, and is not great enough to cause wrinkling and require a stepped die, but the contact condition would surely be different. Also, the presence of drawbeads would increase the resistance to material flow. Therefore, the boundary forces must be altered.

The boundary forces for different regions were calculated based on the contact area of the blank. It was assumed the binder contacted the HSLA at all points while the AKDQ only contacted the binder in the drawbead region,

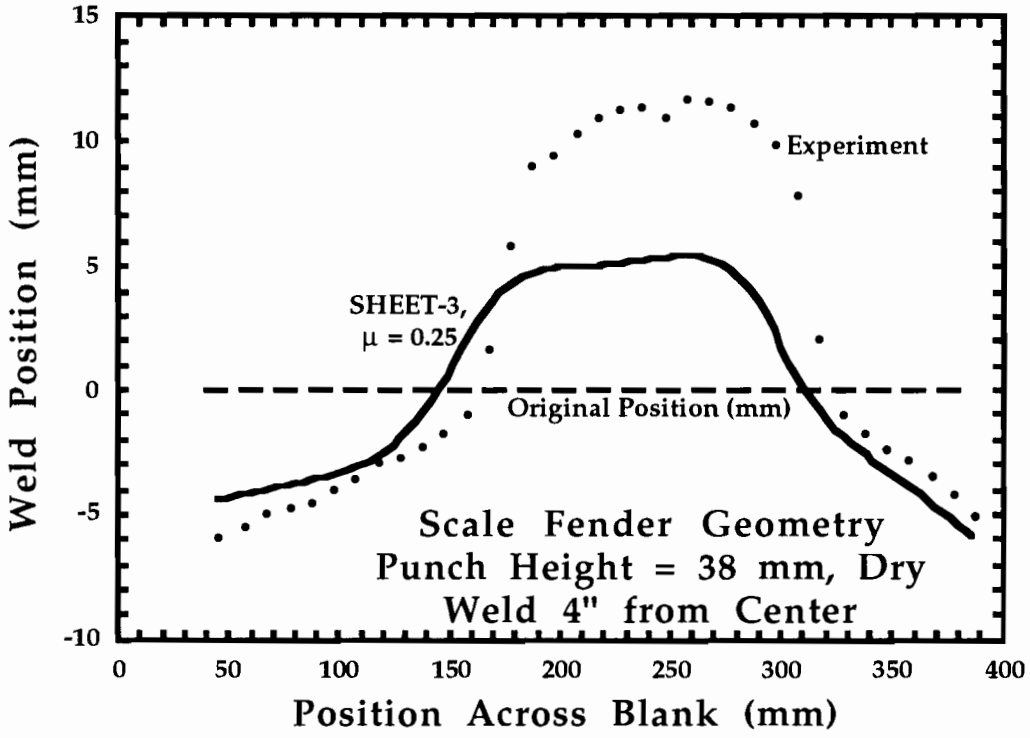

Figure 45. The SHEET-3 predicted weld movement compared to the experimental values for a HSLA/AKDQ blank with the weld 4" from center, no lubrication with even boundary forces around the blank.

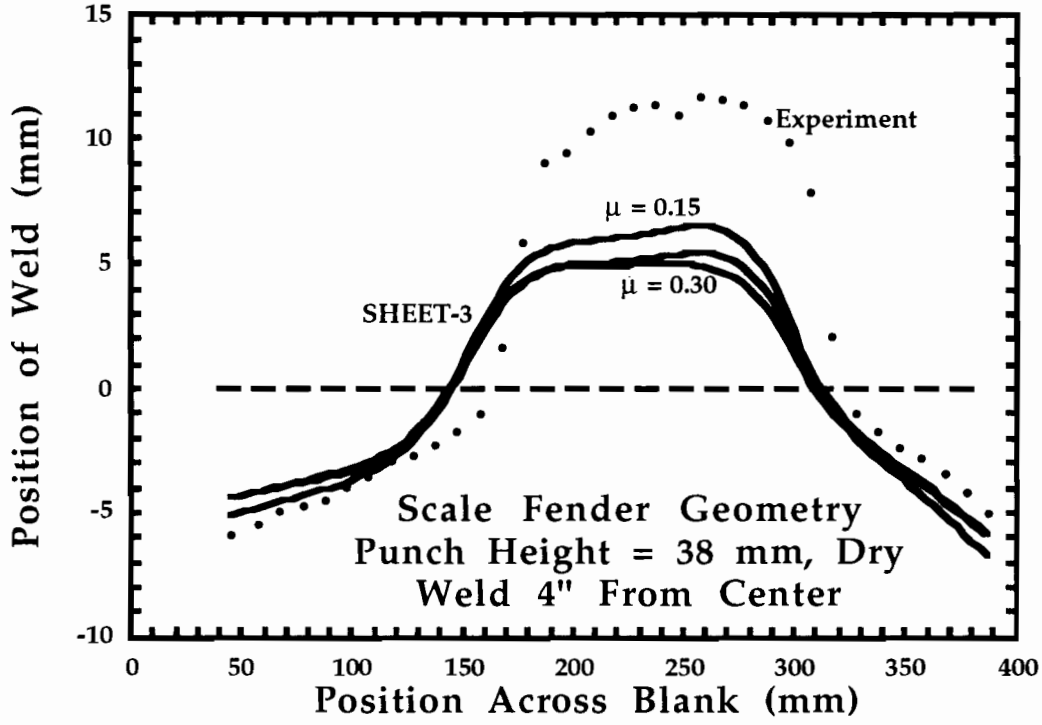

Figure 46. The SHEET-3 predicted weld movement compared to the experimental values for a HSLA/AKDQ blank with the weld 4" from center, no lubrication at a number of different friction coefficients..

because of the difference in thickness. Based on the area of contact, friction coefficient and blankholder force, the resistance force on each node was calculated. There was no allowance for the resistance force provided by the drawbead. This procedure and calculated boundary forces are included in detail in Appendix C.

These boundary forces resulted in divergence for SHEET-3. It was found that they had to be increased for the program to converge, let alone predict the experimental behavior. They were increased until the simulated weld movement matched the experimental weld movement. The reason for increasing the boundary forces cannot be justified directly. There are a couple possibilities, however. First, initially there was no accounting for the force required to pull the workpiece through the bead. In the final values, the forces were increased in the drawbead regions, but without any experimental basis. Second, the base materials are 2mm thick and are flowing over a die radius of 10 mm. This gives an r/t ratio of 5, which means the bending forces could be significant. Since SHEET-3 is a membrane code, the bending forces are not calculated. Therefore, the higher forces could be a result of neglecting the bending. A schematic of the blank and the corresponding boundary forces per node in each region is shown in Figures 47-50.

In an attempt to provide more justifiable boundary conditions, a drawbead restraining force model proposed by Stoughton [56] was employed. Stoughton proposed that there was a force resisting the flow of the sheet metal through a drawbead. This force was calculated based on the work required to bend the material around the different radii of a drawbead. This model also includes the material properties of the sheet (i.e. the work hardening and the rate sensitivity) as well as accounting for a bead that is not fully penetrating. The

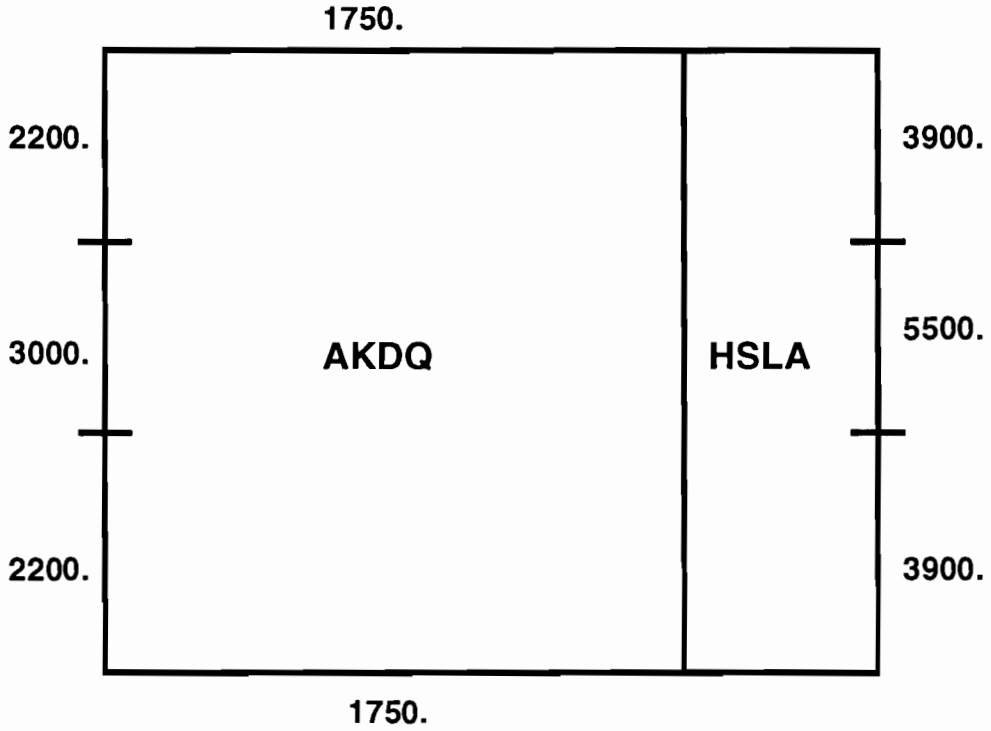

Figure 47. The blank holder forces fit to experiment used around the edge of the blank for the blank with the weld located 4" from center, no lubrication.

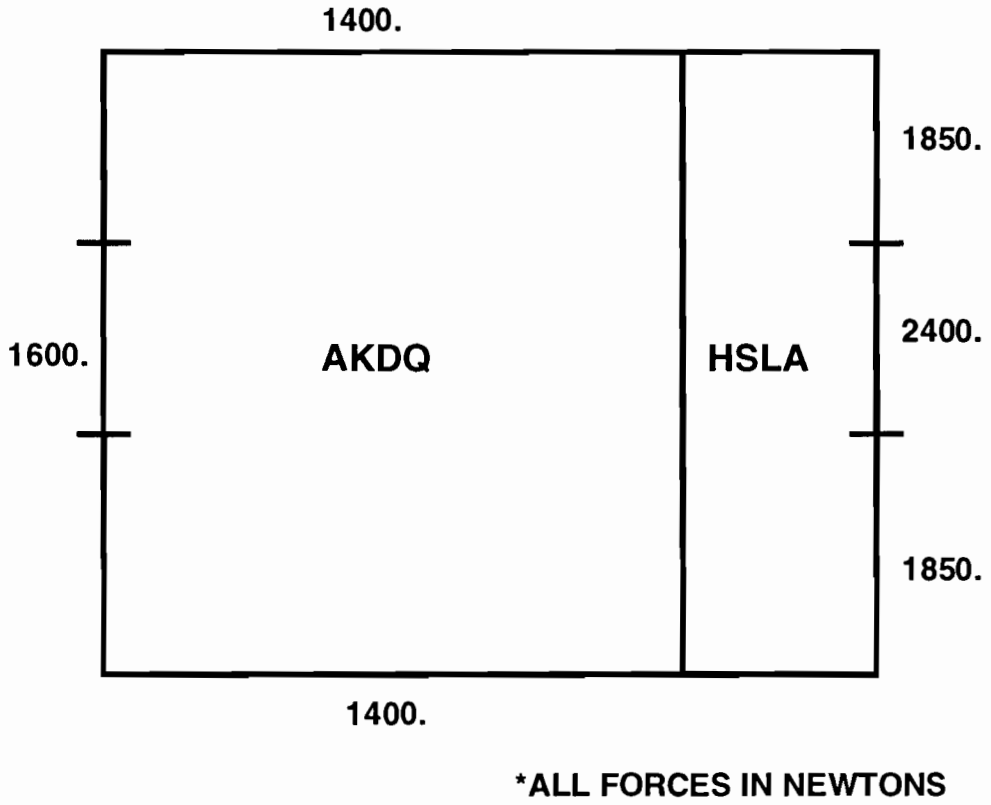

Figure 48. The blank holder forces fit to experiment used around the edge of the blank for the blank with the weld located 4" from center, lubricated.

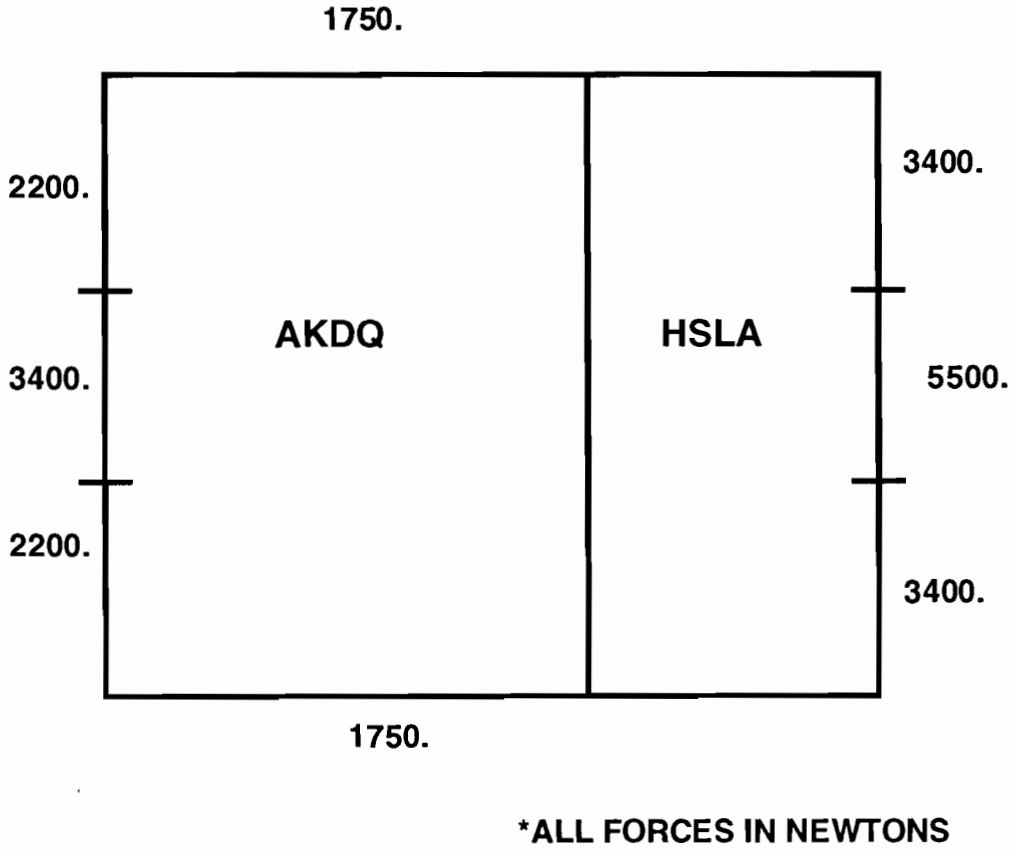

Figure 49. The blank holder forces fit to experiment used around the edge of the blank for the blank with the weld located 2" from center, no lubrication.

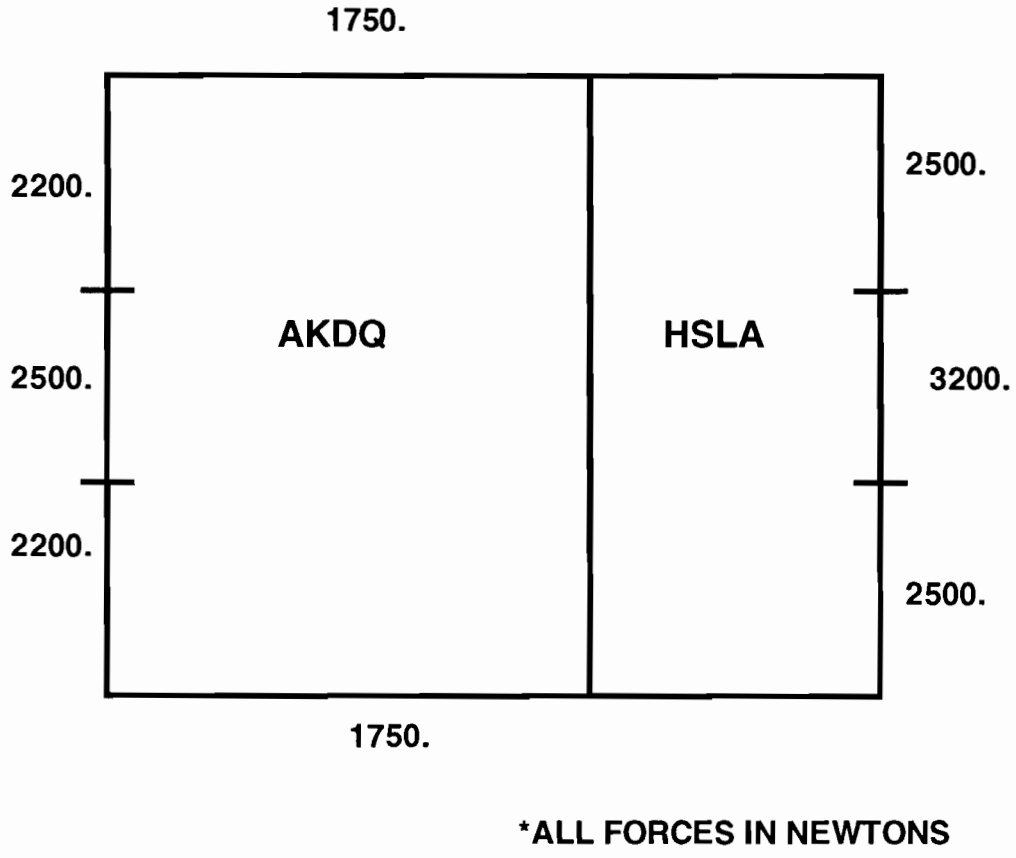

Figure 50. The blank holder forces fit to experiment used around the edge of the blank for the blank with the weld located 2" from center, lubricated.

calculation is shown in detail in Appendix C. The restraining forces for the drawbeads calculated by the model were used as the restraining force at the nodes corresponding to the drawbeads in the AKDQ. In the regions between the drawbeads a token restraining force of 500 N was applied to maintain numerical stability. Having a restraining force of zero at any point on the blank would produce divergence. In the HSLA region, there was a force corresponding to the blankholder force on the blank all around the edge. This was calculated in the same way as the previous paragraph. The corresponding drawbead restraining force was added where necessary. The resistance forces, in Newtons, are shown in Figures 51 through 54.

4.2 Results

Figures 55 through 58 shows the comparison of the experimentally measured weld movement for different forming conditions compared to SHEET-3 simulations with the best fit boundary force model. The four conditions are:

1.) Weld 4" from center line, no lubrication

2.) Weld 4" from center line, lubrication

3.) Weld 2" from center line, no lubrication

4.) Weld 2" from center line, lubrication

Again, lubrication means Stuart dry film + plastic. In almost all cases, the simulated maximum movement of the center part of the weld matched the experiments. The greatest discrepancies came near the edge on the blank.

Figures 59 through 62 shows the FEM compared to experiment using the Stoughton drawbead restraining force model. The correlation to experiment is not as good, although this model predicts the dry conditions with some accuracy. There is a significant amount of error for the lubricated conditions. However, the

boundary forces on this model were calculated with some analytical basis, whereas the previous model had none.

4.3 Prediction of Failure in the Scale Fender Die

Now that the ability to predict the movement of the weld using FEM has been established, now it will be determined if the SHEET-3 code can predict the failure modes and heights that were observed experimentally. Simulations were run with the weld located at the positions corresponding to those in Figure 35. The simulations were run to 57 mm using the best fit boundary forces. The best fit forces were used because they had the best correlation to experiment, and would most likely predict the experimental failure modes. The failure height and position was defined as when an element had a thickness strain of -0.30 or greater.

Figure 63 shows the experimental failure heights (as reported in Figure 37) compared to SHEET-3 predicted simulated failure heights. For the most part, the FEM is in somewhat reasonable correlation with the experiment. The only two major diversions from the experimental behavior is first when the weld in located 2" from center the FEM predicted failure height is much higher than what is observed experimentally (48 mm compared to an experimental failure height of 42 mm). Also, when the weld was located at the center, SHEET-3 predicted failure in the corner of the AKDQ instead of the HSLA. Therefore, there is some error again in the model.

In order to determine what has the larger influence on the formability and the prediction, simulations were run varying the resistance forces and the friction over the tools. The first simulation run was for the highly lubricated condition, with low friction and low boundary forces with the weld located 4" from center. The second simulation was run with boundary forces for low friction but a high

friction coefficient, to determine if increasing friction would have a detrimental effect on the punch height without changing the boundary forces. The third simulation was run with low friction over the punch but with boundary forces correlating to dry conditions. This way it could be determined if the boundary forces or the punch friction is most important in increasing formability.

In all cases, the critical area was in the AKDQ, parallel to the weld. With the fully lubricated friction and boundary force condition, the peak thickness strain at a punch height of 40 mm was -0.28, which is already 3 mm higher than the simulated failure height for the dry conditions. When a friction coefficient of 0.25 was used with the lubricated condition boundary forces, the peak thickness strain was -0.30. Therefore, the friction over the punch does have some influence on the formability. When the lubricated friction coefficient of 0.10 is used with the boundary forces correlating dry conditions, the peak thickness strain shoots up to -0.37. Therefore, even with low friction over the punch, the formability is relatively poor with the higher boundary forces. Therefore, it can be concluded that the boundary forces are the most critical variable to have a clear knowledge of in determining accurate failure modes of stretch-draw forming operations using FEM. This would explain the error in predicting the failure modes of the different weld positions in the scale fender die. For the weld at the center and 2" from center, there was most likely an inaccuracy in boundary forces, resulting in a poor prediction of the failure mode.

4.4 Discussion

Although the blankholder force values may not be exact, the trends are significant. The lubrication had very little influence on the weld movement in

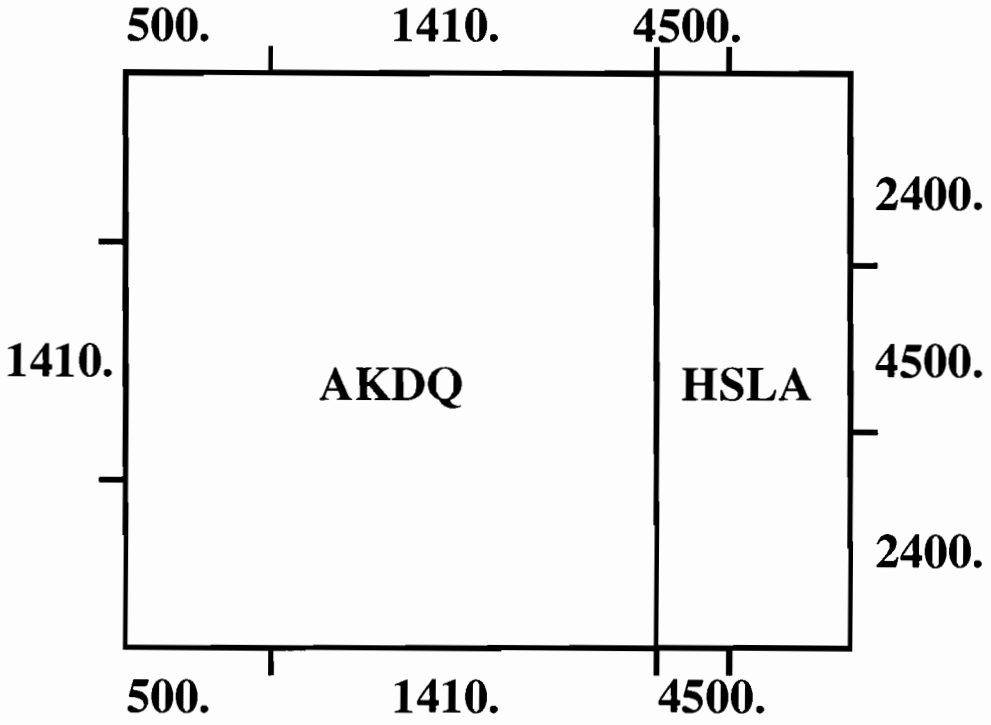

Figure 51. The restraining forces used for the blank with the weld 4" from center, dry conditions calculated based on Stoughton's drawbead model and binder force.

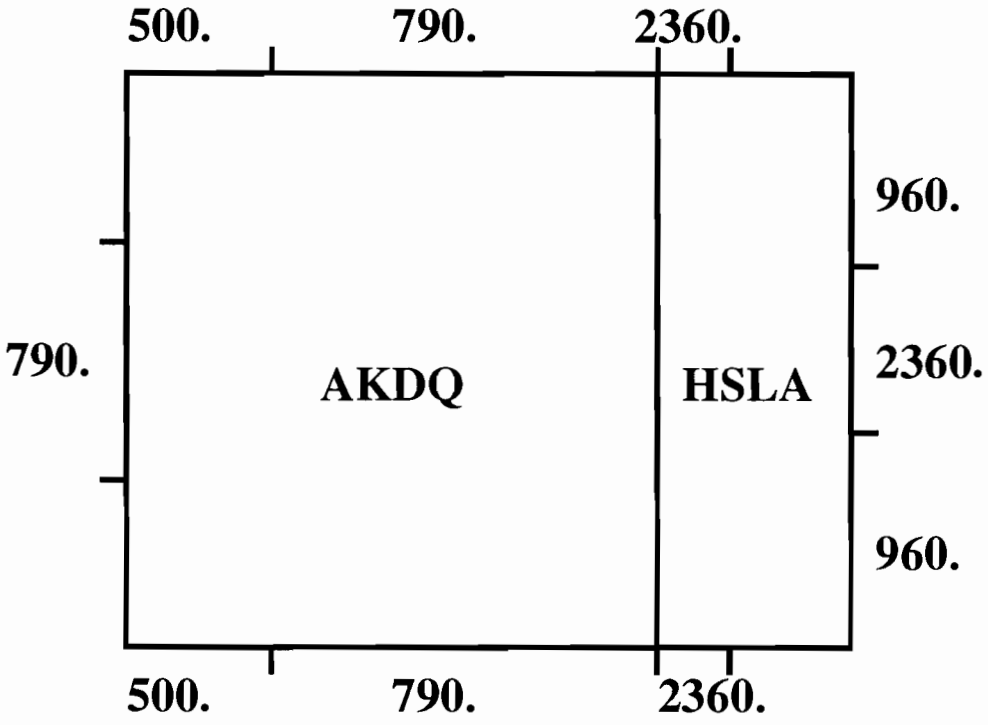

Figure 52. The restraining forces used for the blank with the weld 4" from center, lubricated conditions calculated based on Stoughton's drawbead model and binder force.

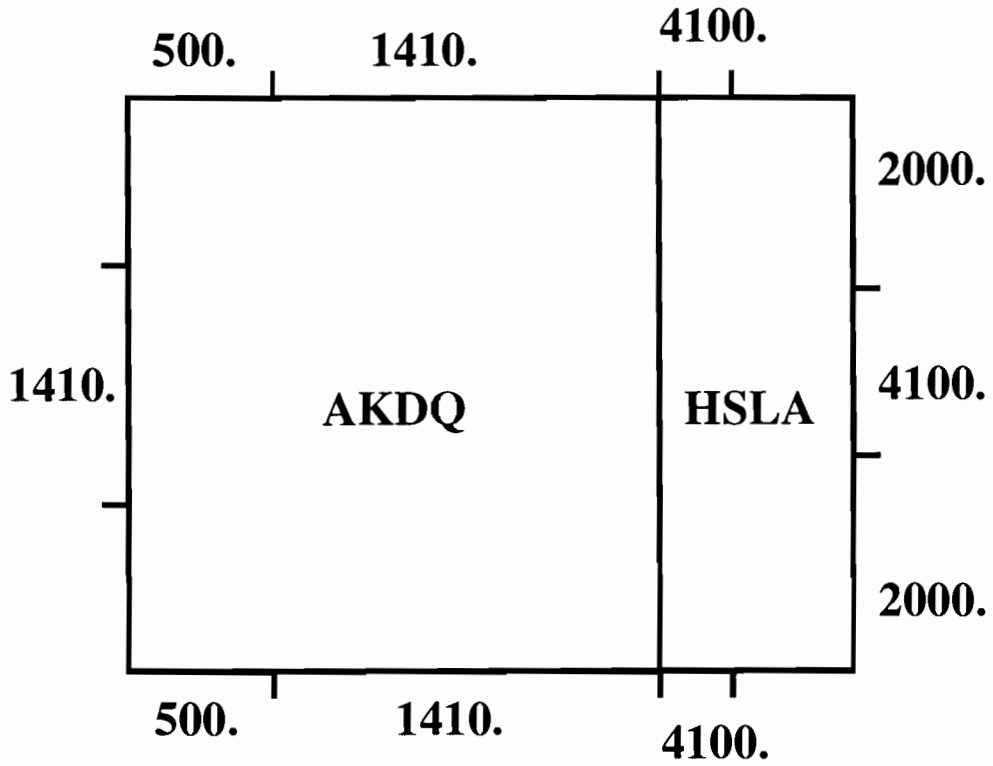

Figure 53. The restraining forces used for the blank with the weld 2" from center, dry conditions calculated based on Stoughton's drawbead model and binder force.

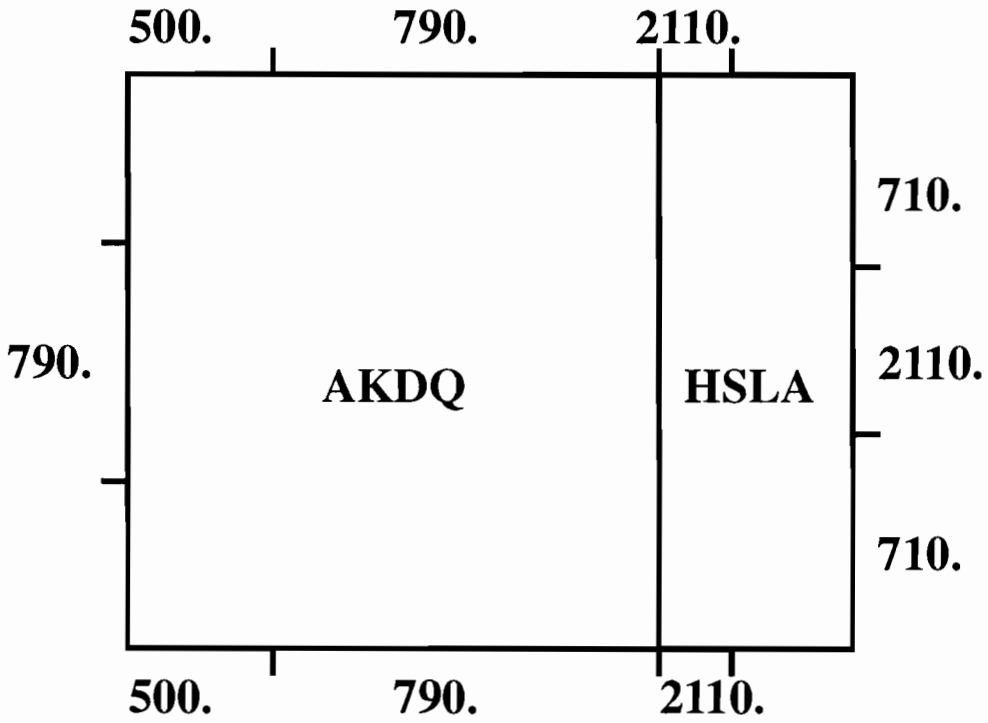

Figure 54. The restraining forces used for the blank with the weld 2" from center, lubricated conditions calculated based on Stoughton's drawbead model and binder force.

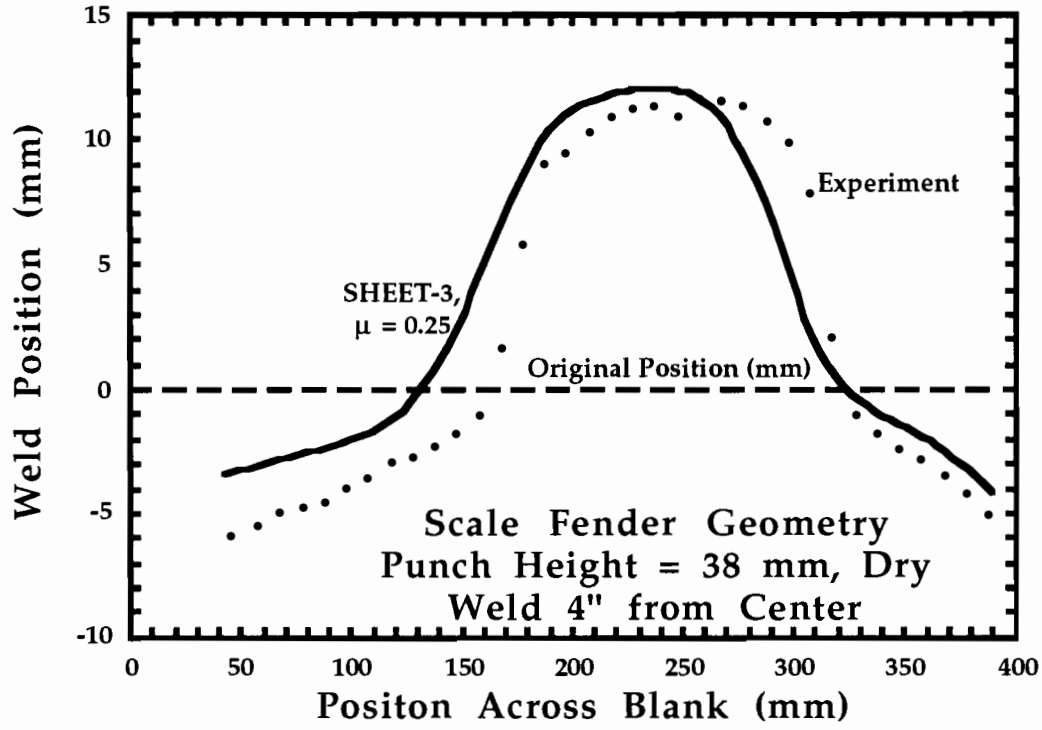

Figure 55. The SHEET-3 predicted weld movement using fit boundary conditions compared to the experimental values for a HSLA/AKDQ blank with the weld 4" from center, no lubrication.

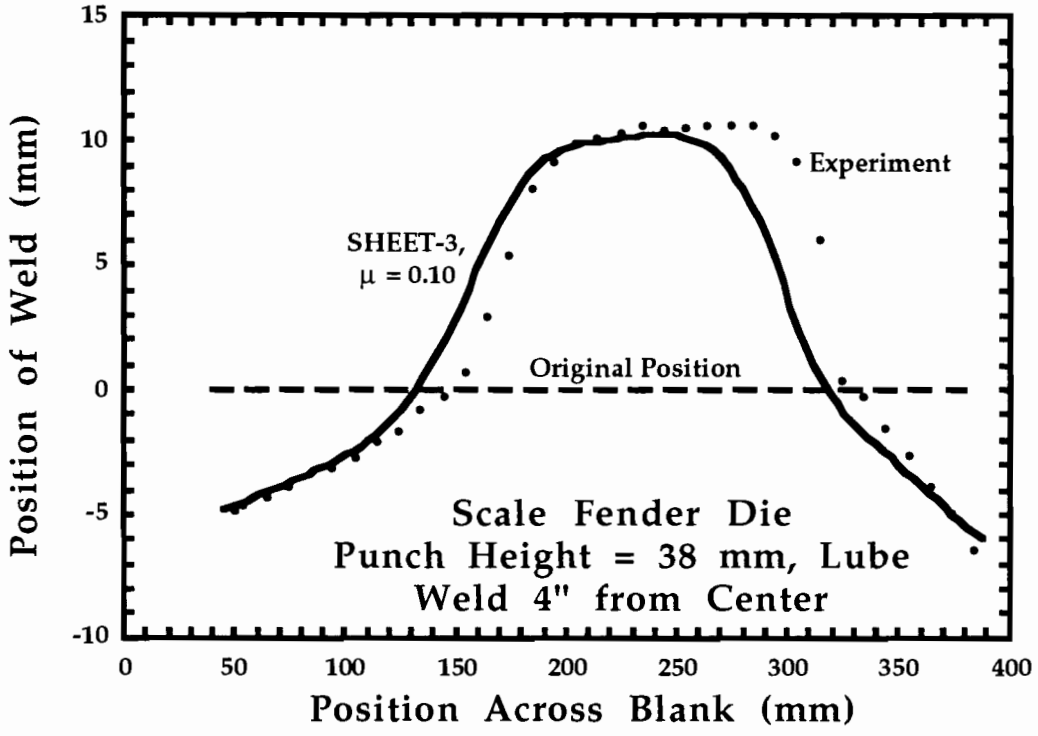

Figure 56. The SHEET-3 predicted weld movement using fit boundary conditions compared to the experimental values for a HSLA/AKDQ blank with the weld 4" from center, lubricated.

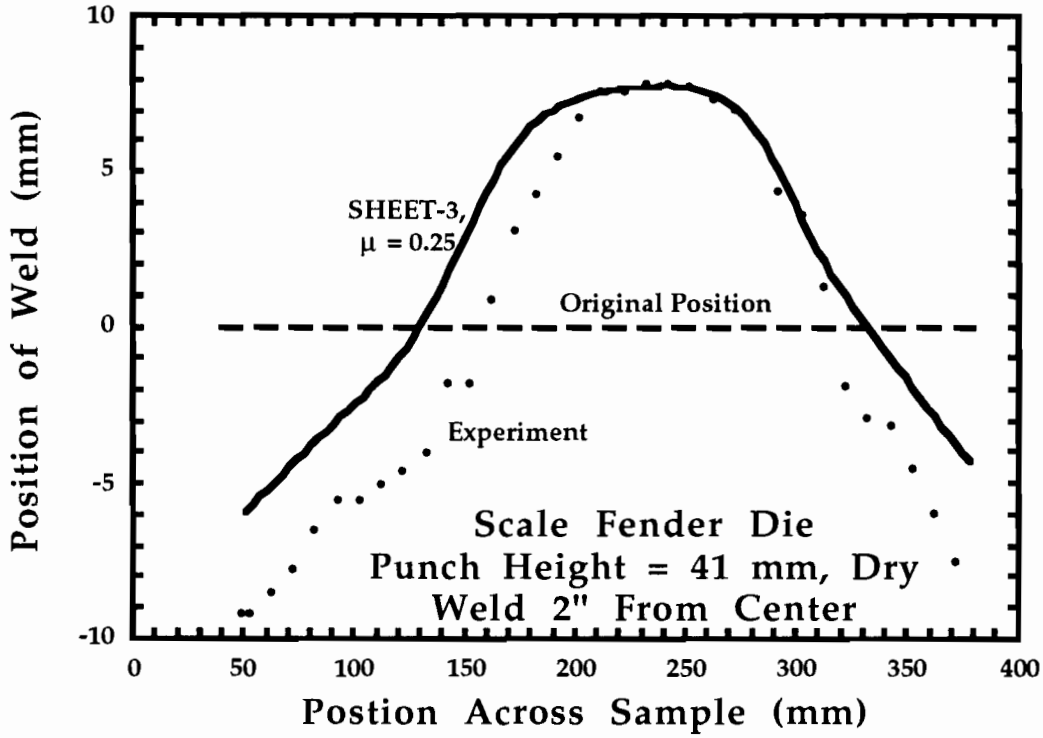

Figure 57. The SHEET-3 predicted weld movement using fit boundary conditions compared to the experimental values for a HSLA/AKDQ blank with the weld 2" from center, no lubrication.

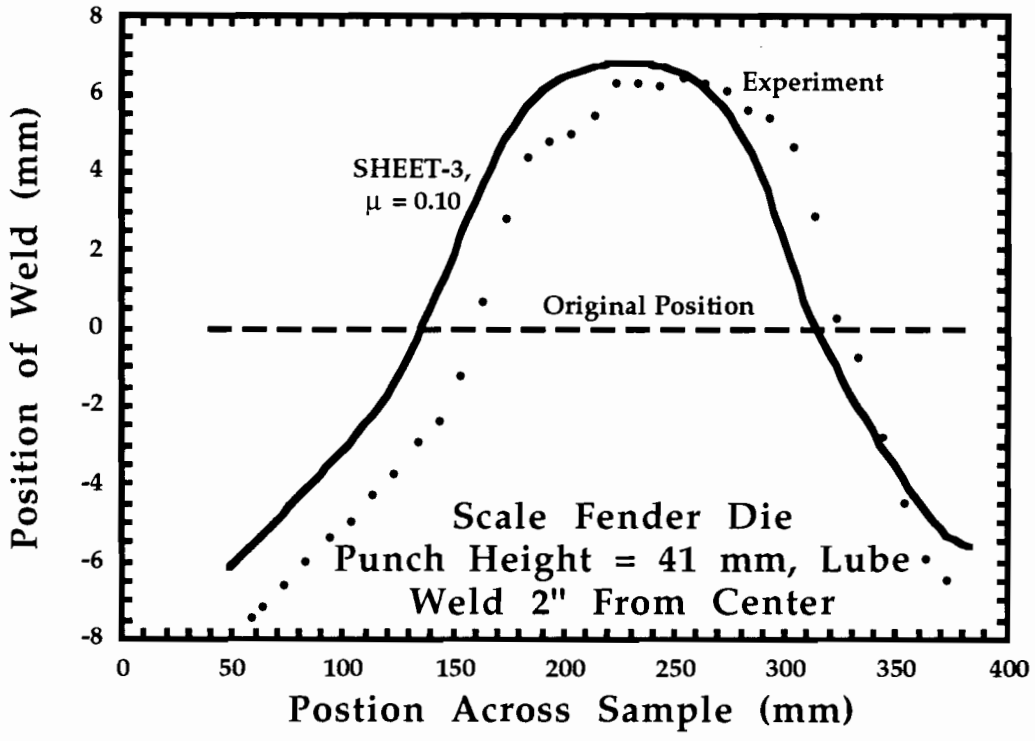

Figure 58. The SHEET-3 predicted weld movement using fit boundary conditions compared to the experimental values for a HSLA/AKDQ blank with the weld 2" from center, lubricated.

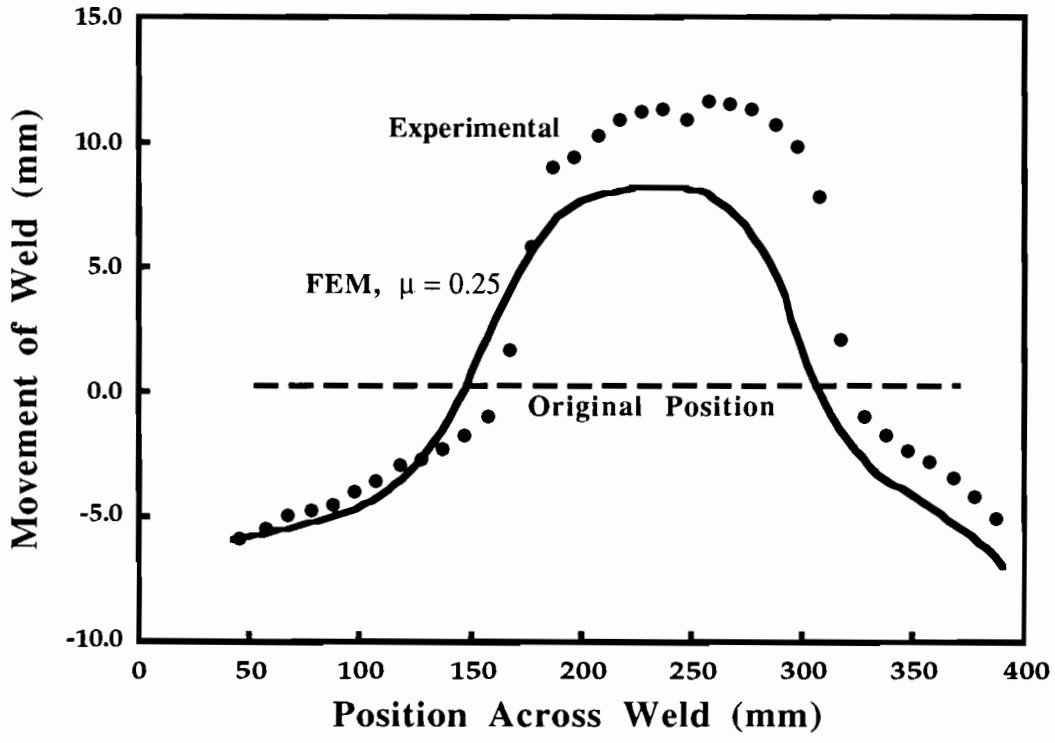

Figure 59. The SHEET-3 predicted weld movement using calculated boundary conditions compared to the experimental values for a HSLA/AKDQ blank with the weld 4" from center, dry.

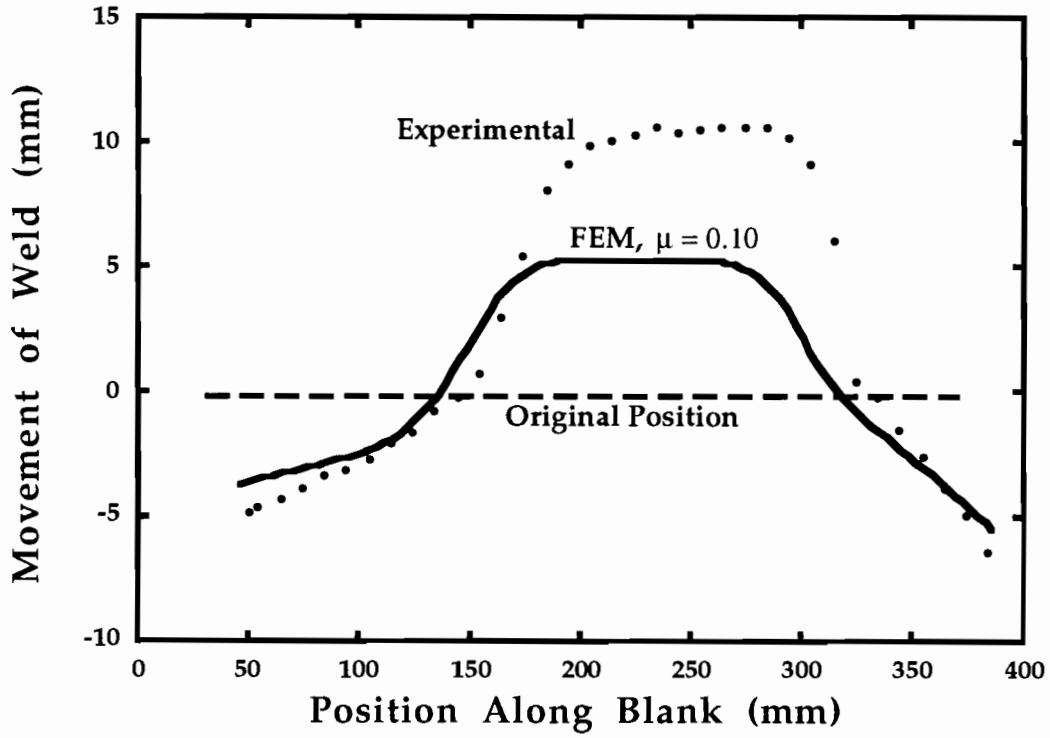

Figure 60. The SHEET-3 predicted weld movement using calculated boundary conditions compared to the experimental values for a HSLA/AKDQ blank with the weld 4" from center, lubricated.

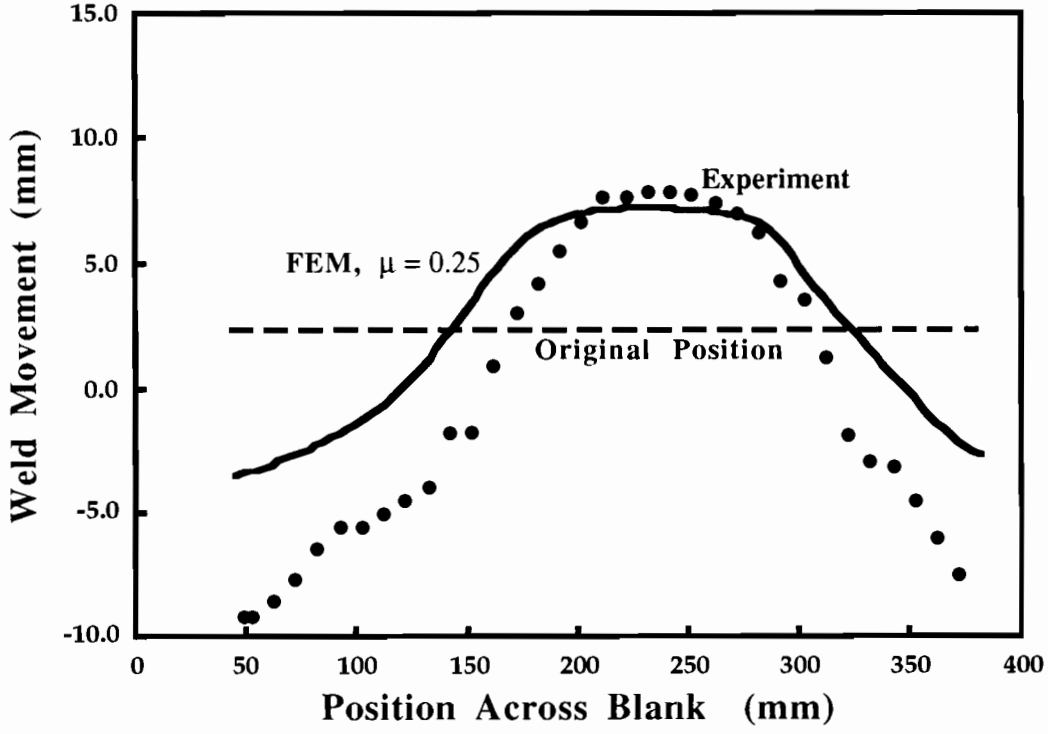

Figure 61. The SHEET-3 predicted weld movement using calculated boundary conditions compared to the experimental values for a HSLA/AKDQ blank with the weld 2" from center, dry.

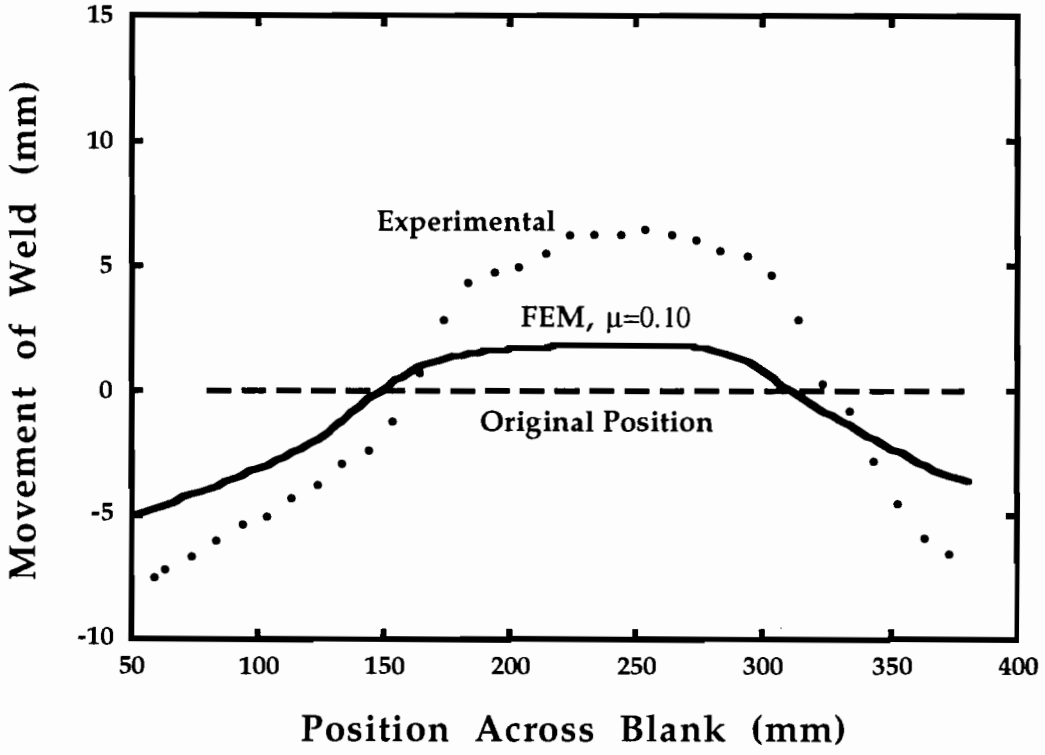

Figure 62. The SHEET-3 predicted weld movement using calculated boundary conditions compared to the experimental values for a HSLA/AKDQ blank with the weld 2" from center, lubricated.

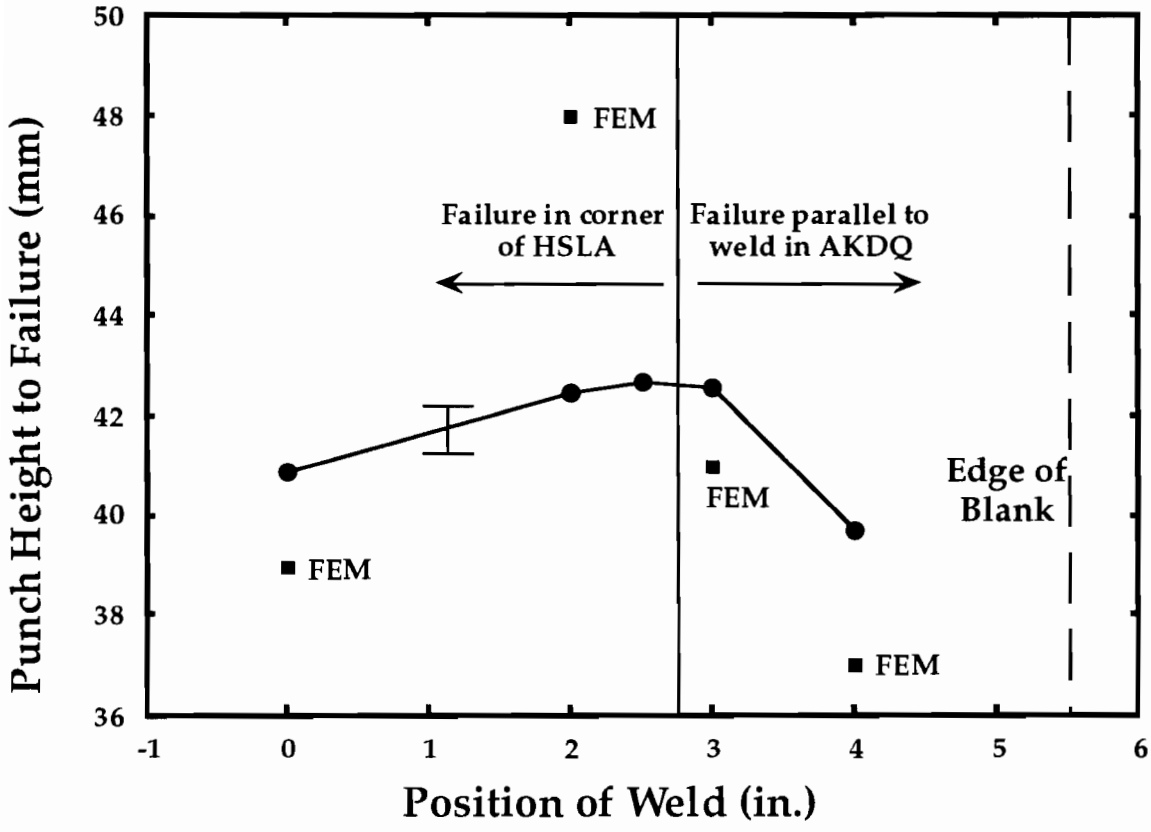

Figure 63. SHEET-3 predicted failure heights of the scale fender die using best fit boundary forces compared to experimental failure heights.

the experimental analysis, yet there was significant improvement in formability. From the FEM simulation, we have a little more insight on why the formability is improved. The boundary forces used to match the experiments were significantly lower for the lubricated samples compared to the dry specimens. Therefore, the influence of the lubrication seems to be in reducing the boundary forces around the sample, allowing more material to flow into the die, reducing the severity of the stretch.

The key development in this study is that an FEM model can be used to predict the experimental weld movement in a complex stretch-draw operation of a tailor-welded blank. Because of the aforementioned reasons, having this type of predictive ability is very valuable for die and product design engineers. The second is that the key issue in predicting this weld movement in a stretch-draw condition has also been determined: accurate knowledge of the boundary forces acting around the edge of the blank. The local properties of the weld are insignificant, and the plastic hardening behavior of the base materials can be determined and modeled with great accuracy. The friction did not have a great effect on the weld movement, so the one unknown that requires a precise experimental understanding are these boundary forces. If one knows these accurately, then the forming behavior of a tailor-welded blank should be able to be predicted with reasonable confidence.

CHAPTER VIII

SIMPLE ANALYTICAL MODEL TO PREDICT WELD MOVEMENT

1. Introduction

We have observed the weld line movement in complex forming operations of tailor welded blanks. We have seen how this weld movement influences the strain states in the base materials and thus has an influence on the formability of a tailor welded blank. The variables than drive this weld movement and what variables have an effect on the weld movement were also determined. In this section, a simple one dimensional model will be proposed that will give up a better understanding of the fundamentals of what controls the weld movement in the forming of a tailor welded blank. The results of this simple model will be compared to FEM results of SHEET-S, which is the plane strain 2-D sister program to SHEET-3.

2. The Model

The model assumes a welded blank is being stretched (no draw) over a punch with 0 mm radius corners. The punch face (Figure 64) is 50 mm (L in Figure 64) and the gap between the punch and the clamp is 20 mm (g in Figure 64). The weld position is at a distance l from the left edge in Figure 64 and the punch travels to a height of h (Figure 64). Using this simple geometry the amount of weld movement and the strain ratios of the two regions will be predicted as a

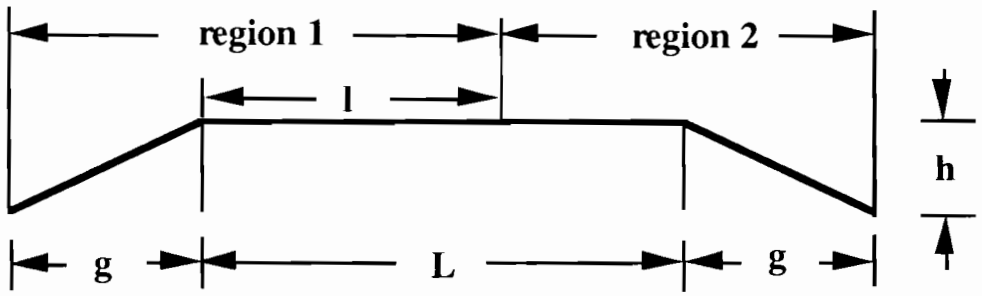

Figure 64. Schematic of the geometry used for the simplified model for weld movement prediction.

function of the difference in material properties of the two regions, the punch travel, and the location of the weld l on the punch face.

The model was set up mathematically in the following way. It is assumed from the start that there is no friction interacting between the punch and the workpiece. First we need to relate the strains in the two regions two each other. This can be done knowing the hardening laws of the base materials and assuming the load is constant throughout the entire blank. First, we can assume the material follows the Hollomon hardening law, defined as:

$$\bar{\sigma} = K\bar{\varepsilon}^{n} \tag{4}$$

Converting to engineering stress, the equation now becomes:

$$\sigma_{eng} = K\bar{\varepsilon}^{n}e^{-\bar{\varepsilon}} \tag{5}$$

Assuming the original cross sectional areas of the two blanks are equivalent, and knowing the load supported by region 1 will equal that supported by region 2, the following relationship evolves:

$$K_1\bar{\varepsilon}_1^{\,n_1}e^{-\bar{\varepsilon}_1} = K_2\bar{\varepsilon}_2^{\,n_2}e^{-\bar{\varepsilon}_2} \tag{6}$$

Also, the strains are related to each other through the original and final length of the sheet:

$$(l+g)e^{\bar{\varepsilon}_1} + (L-l+g)e^{\bar{\varepsilon}_2} = L + 2\sqrt{g^2+h^2} \tag{7}$$

This can be rearranged to solve for $\bar{\varepsilon}_2$ as a function of $\bar{\varepsilon}_1$:

$$\bar{\varepsilon}_2 = \ln\left[\frac{-\left[(1+g)e^{\bar{\varepsilon}_1}\right] + L + 2\sqrt{g^2+h^2}}{(L-1+g)}\right] \tag{8}$$

Inserting (8) into (6) gives the relation:

$$\frac{K_1}{K_2}\bar{\varepsilon}_1^{n_1}e^{-\bar{\varepsilon}_1} - \left[\ln\left[\frac{-\left[(1+g)e^{\bar{\varepsilon}_1}\right] + L + 2\sqrt{g^2+h^2}}{(L-1+g)}\right]\right]^{n_2}\left[\frac{(L-1+g)}{-\left[(1+g)e^{\bar{\varepsilon}_1}\right] + L + 2\sqrt{g^2+h^2}}\right] = 0 \tag{9}$$

This equation was solved using modified linear interpolation to solve for $\bar{\varepsilon}_1$.

Equations (8) and (9) will give the strain ratio for the different regions under different forming conditions. The final position of the weld can be determined by calculating the final length of region 1 and the subtracting out was is geometrically necessary:

$$l_f = (1+H)e^{\bar{\varepsilon}_1} - 2\sqrt{g^2+h^2} \tag{10}$$

which would give the weld movement.

3. Comparison of simple model to 2-D FEM

The results of the simple model was compared to simulations run using the 2-D plane strain finite element code SHEET-S. SHEET-S has all the same basic formulations as SHEET-3, but with only two dimensions. The tool description was set up with nearly the same dimensions, with the only

discrepancy in the punch radius. A radius of 1 mm was used as opposed to 0 mm in the model. SHEET-S would not converge with a 0 mm radius. At a punch height of 10 mm, assuming constant properties throughout the sheet, the analytical model predicted a strain of 0.051 throughout with the FEM predicted 0.053. This difference is assumed to be a result of punch radii.

3.1 Varying K_2/K_1 Ratios

The point of varying the K_2/K_1 ratio is to look at how the strength ratio affects the weld movement and strains in both regions. Figure 65 shows how the weld movement behaves with increasing K ratio. In this model, the weld line was in the center of the punch face, i.e. l = L-l and the punch travel was 10 mm. As the K ratio increases, the weld movement increases and moves towards the material with the higher K value. This is predicted by both FEM and the simple analytical model. The reason this happens can be explained by looking at Figures 66 and 67. As the K ratio increases, the amount of strain in region 2 decreases. Therefore region 1 stretched more, resulting in the interface (the "weld line") moving towards the region 2 material. Again, the FEM and the analytical model both predicted this sort of behavior.

3.2 Increasing Height

Figure 68 shows the predicted weld line movement as a function of increasing height. In these predictions, the weld line was in the center of the punch face and the K_2/K_1 ratio was set at 1.2. It was set at this level because the FEM would have trouble converging with higher ratios. As can be observed, the punch height increases as a function of punch travel. Again, looking at Figures 69 and 70, the strain behavior explains this phenomena. The strain in region 2 does not increase all that much with punch travel, while the strain in region

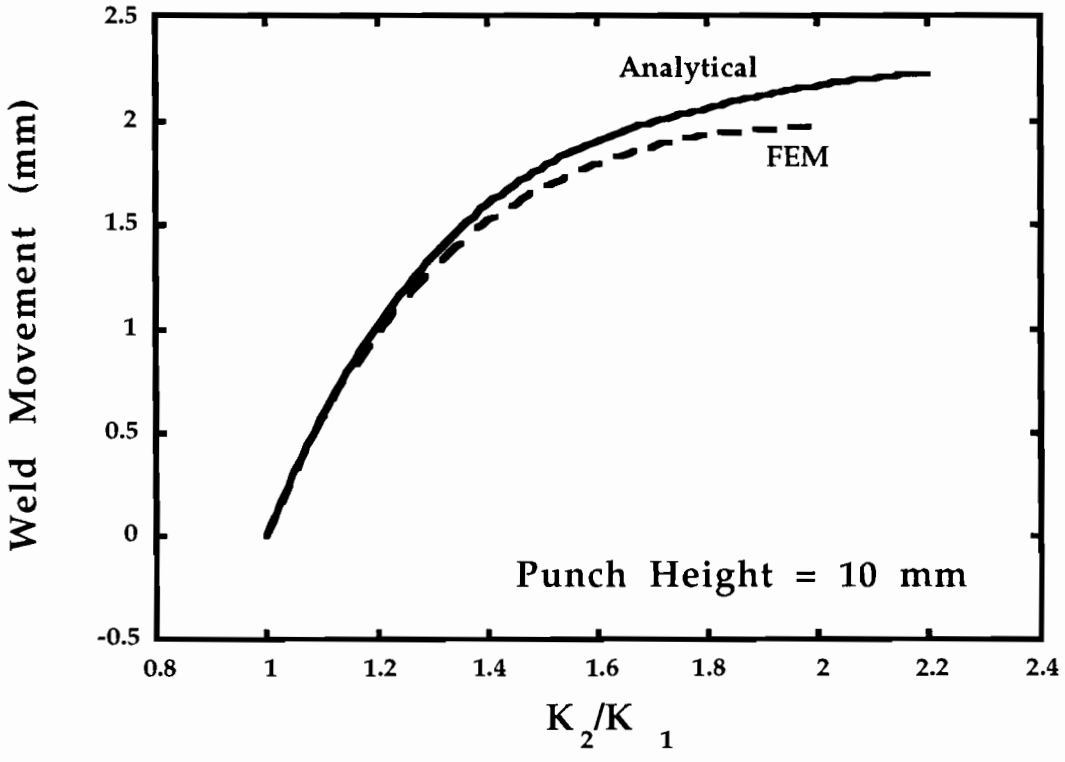

Figure 65. The change in the weld position as a function of the K_2/K_1 ratio with the weld in the center of the sheet at 10 mm punch height for as predicted by the simple analytical model and by SHEET-S.

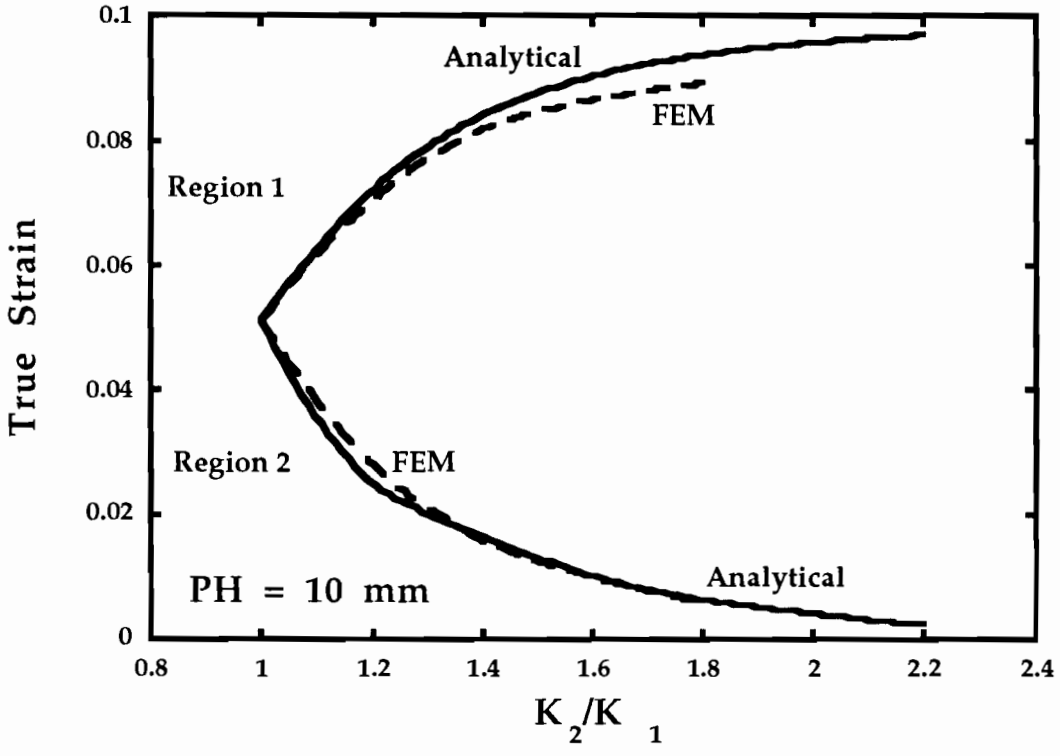

Figure 66. The strains in both regions as a function of the K_2/K_1 ratio with the weld in the center of the sheet at 10 mm punch height for as predicted by the simple analytical model and by SHEET-S.

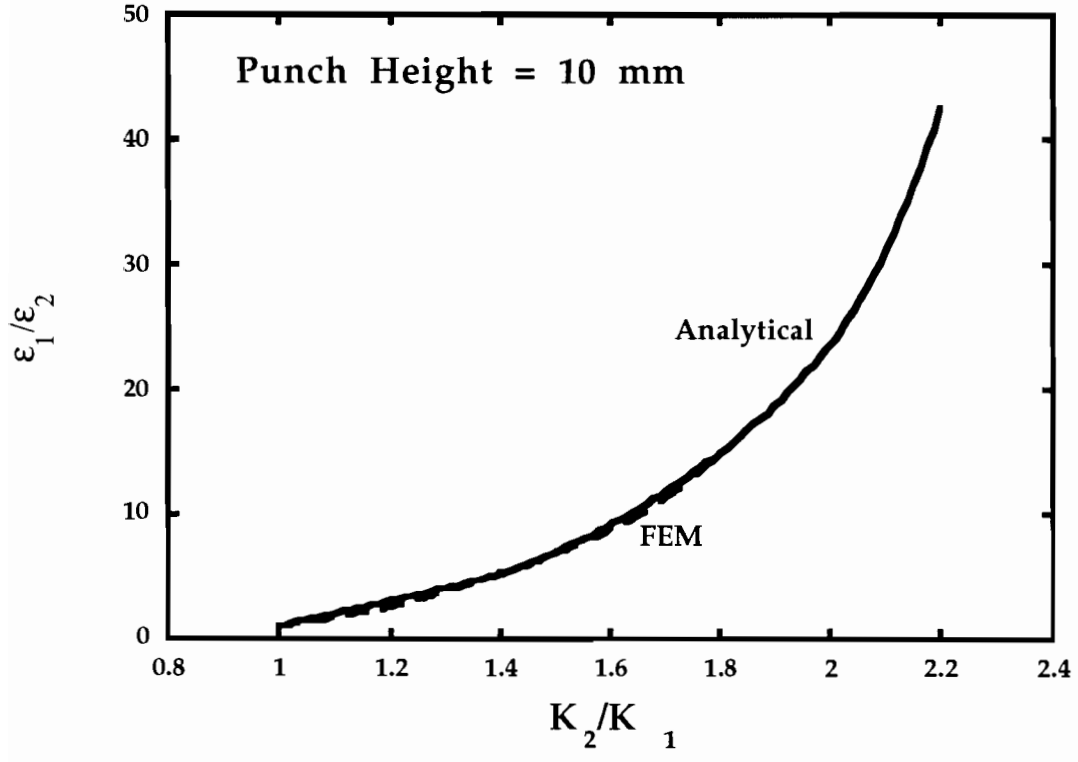

Figure 67. The strain ratio of the two regions as a function of the K_2/K_1 ratio with the weld in the center of the sheet at 10 mm punch height for as predicted by the simple analytical model and by SHEET-S.

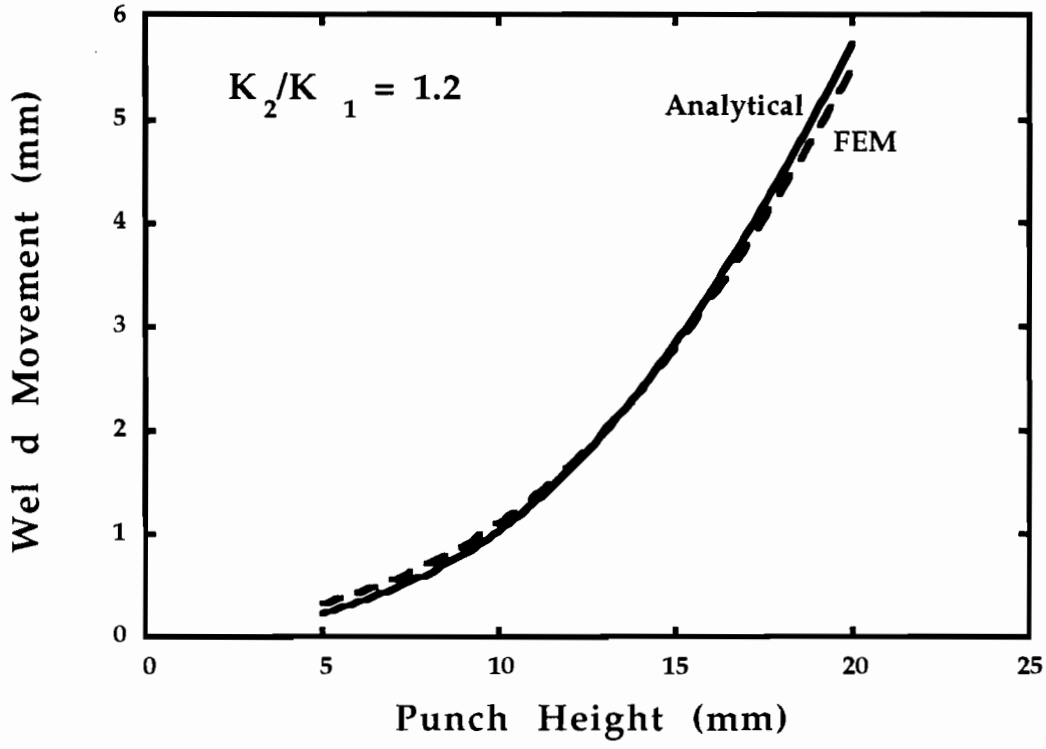

Figure 68. The change in the weld position as a function of the punch travel with the weld in the center of the sheet and $K_2/K_1 = 1.2$ as predicted by the simple analytical model and by SHEET-S.

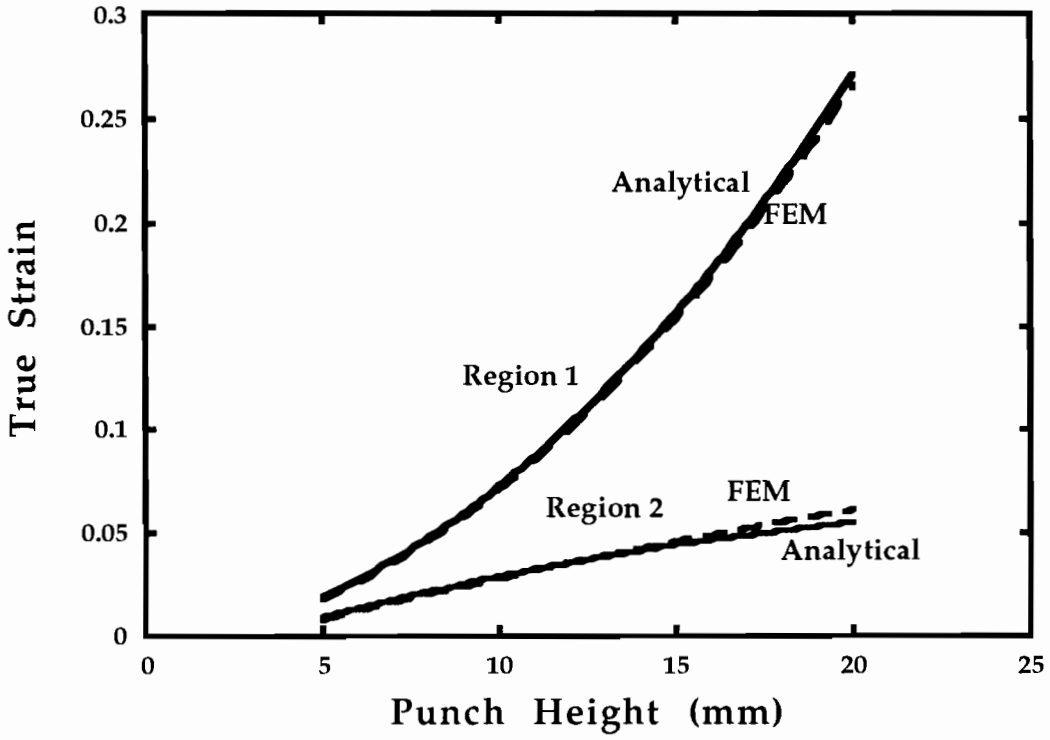

Figure 69. The strains in both regions as a function of the punch travel with the weld in the center of the sheet and $K_2/K_1 = 1.2$ as predicted by the simple analytical model and by SHEET-S.

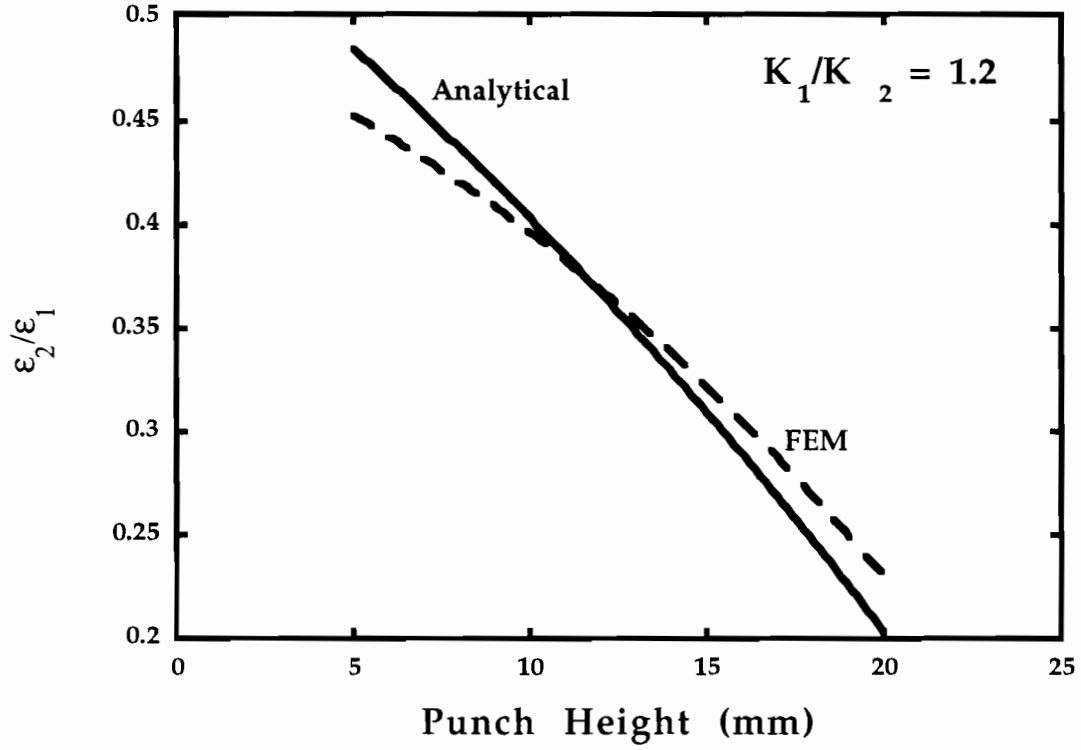

Figure 70. The strain ratio of the two regions as a function of the punch travel with the weld in the center of the sheet and $K_2/K_1 = 1.2$ as predicted by the simple analytical model and by SHEET-S.

increases almost exponentially with punch height. Therefore, region 1 is expanding in length with punch travel, resulting in weld movement.

3.3 Different Weld Position

Figure 71 shown the amount of weld movement as a function of the position of the weld. In these predictions, the weld line was in the center of the punch face and the K_2/K_1 ratio was set at 1.2. The punch height was to 10 mm. As the fraction of the weaker material increases, the more weld movement that exists. This is not as clearly understood as the previous effects on weld movement. As one looks at the strains and strain ratios, it is observed that the magnitude of the strains in both regions decrease with increasing fraction of weaker material (Figure 72) and the strain ratios are nearly constant (Figure 73). The explanation that describes this behavior deals with the fraction of weaker to stronger material and how much each segment strains. When there is little of the weaker material, it must strain more to make up for the displacement of the punch travel. As the original length of the weaker material increases, there is less strain required to get to a specific displacement. A similar argument can be used to explain the weld movement phenomena. As the weld approaches the right side, i.e. l is increasing, a given strain in region 1 will give a much higher displacement. Therefore, for a given strain in the weaker material, a blank with a longer region of weaker material will give more weld movement.

4. Summary

This simple model gave some basic ideas on what fundamentally influences weld movement. Basically, the weld movement is governed by the strain ratio and this strain ratio increases the increasing ratio of strength or with punch height. It was also found that as the fraction of the weaker material increased the amount of weld movement also increased. Therefore, as the weld

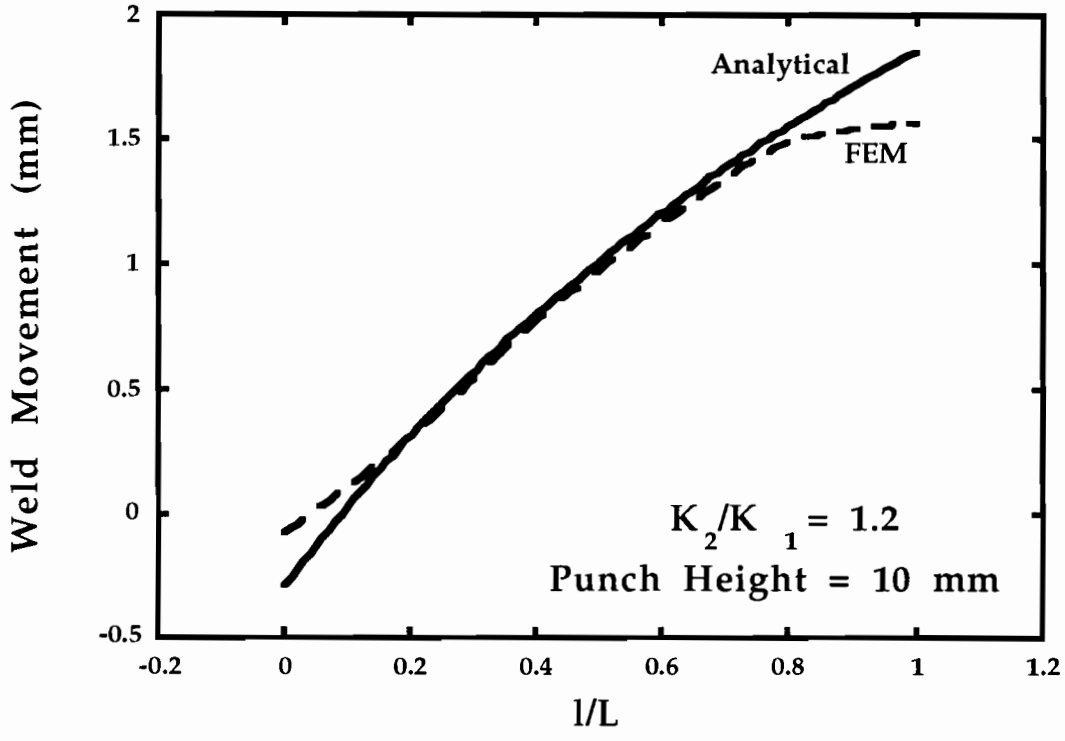

Figure 71. The change in the weld position as a function of the position of the weld at 10 mm punch height and K_2/K_1 = 1.2 as predicted by the simple analytical model and by SHEET-S.

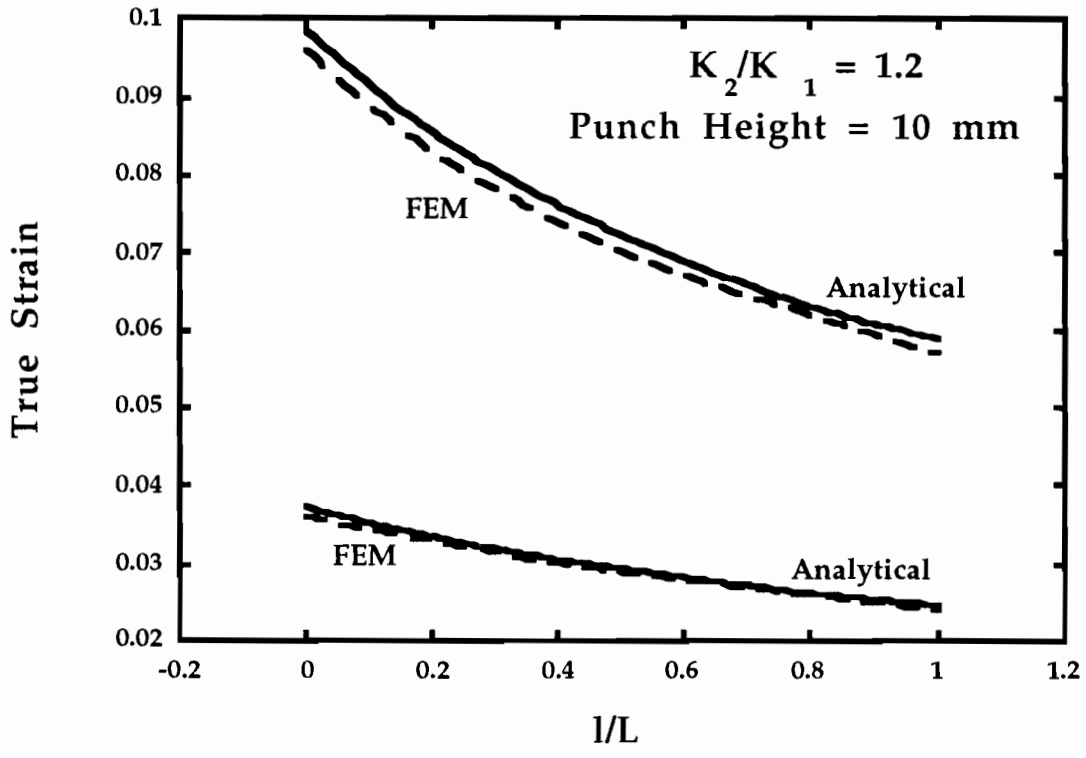

Figure 72. The strains in both regions as a function of the position of the weld with 10 mm punch height and K_2/K_1 = 1.2 as predicted by the simple analytical model and by SHEET-S.

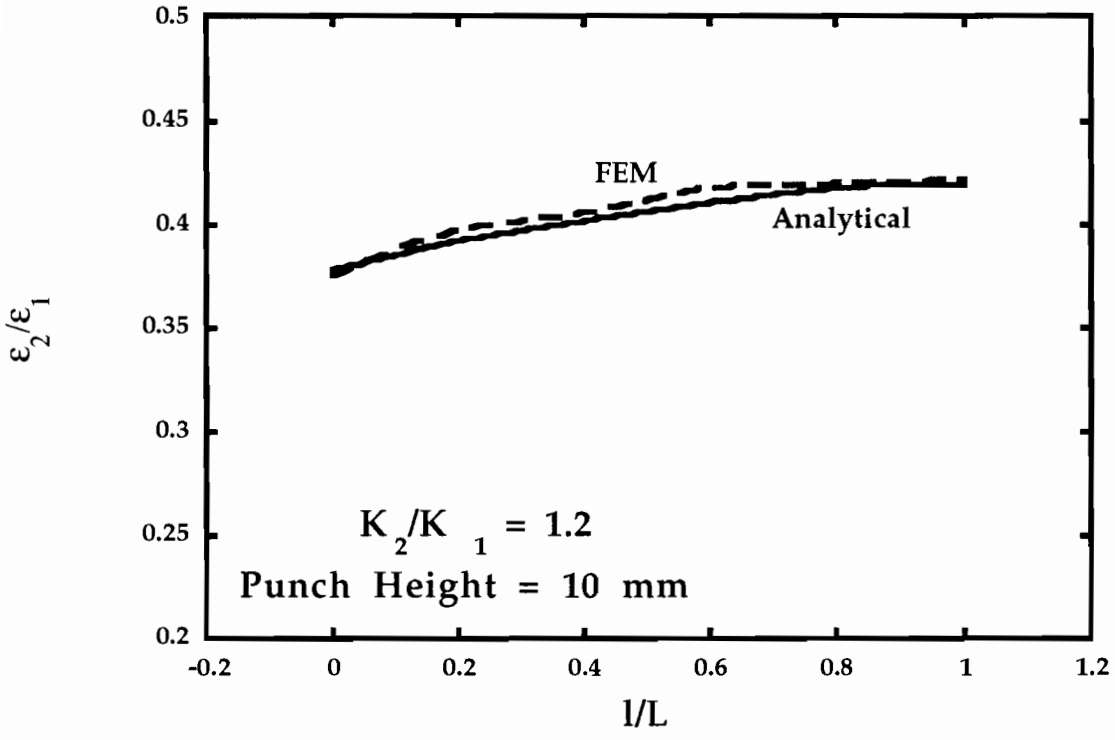

Figure 73. The strain ratio of the two regions as a function of the position of the weld with 10 mm punch height and K_2/K_1 = 1.2 as predicted by the simple analytical model and by SHEET-S.

is located closer to the edge in a geometry such as the scale fender die, a slight increase in weld movement would be expected with all other things equal.

The 2-D FEM code SHEET-S predicted these basic behaviors as well. It was also hoped to compare this model with the 3-D FEM code , SHEET-3, for the scale fender die. This could not happen because SHEET-3 would not converge for frictionless conditions with the scale fender die geometry. Therefore, a suggestion for future work is to modify the simple model to account for friction and then be able to compare it to the SHEET-3 model.

CHAPTER IX

CONCLUSIONS

We have investigated the forming behavior of tailor-welded blanks with the intent of developing an understanding of what factors have the greatest influence on the formability and developing some type of predictive ability for weld placement, type and other design factors. From this study, we have concluded:

1.) Failure in tailor-welded blanks is highly dependent upon the amount the weld line moves and how this weld line movement influences the strain of the base material surrounding the weld line. If the weld movement is too severe and causes stretching of the base material, the base material parallel to the weld line will tear. If the weld movement is not severe, or the boundary forces are such that the weld movement does not result in stretching of the base material, the blank will either fail in the weld bead itself or an some other part of the blank, depending on the loading condition.

2.) The in house code SHEET-3 could be used to model the forming of a tailor-welded blank using the scale fender die on the *Hydraulic Forming Simulator*. The program was able to predict accurately the experimentally-observed movement of the weld during forming. It was found that the most important variable for

accurately predicting the forming behavior was the boundary forces on the edge of the blank in the binder.

3.) The commercial code ABAQUS could be used to accurately predict the weld movement observed in the dome test. This model had good correlation to experiments for a number of different blank widths and material combinations. This model could also be used to evaluate the sensitivity of the weld movement to a number of variables.

4.) There is little or no difference in formability between a mash seam and a laser welded blank. An unplanished mash seam weld had a similar tensile ductility to the laser welds, while the cold planished weld had significantly less ductility that the unplanished weld. The hot planishing process recovered the majority of the ductility lost in planishing. The planished and hot planished welds have much larger heat affected areas than a simple planished weld. The results for the formability testing was very similar between the two welds. The only difference observed was in the dome test where the size of a mash seam weld has a slight influence on weld movement.

5.) There are two different failure modes in a tailor welded blank, depending on the loading. If the majority of loading in parallel to the weld line, then the overall formability is limited by the ductility of the weld. If the majority of the loading is transverse to the weld line, the failure will be in the weaker base material, dictated by the forming limit of the weaker material in plane strain.

6.) The *OSU Formability Test* ranks the weld blanks in the same was as the uniaxial tensile test. However, the separation of weld types is not as significant in the OSU Test as it was in the tensile test.

7.)The dome test (either LDH or full dome stretch) showed no correlation to the uniaxial tensile test. This is because the failure mode of the dome test is that the weld is pulled toward the stronger material, forcing the weaker base material to fail parallel to the weld. This type of behavior is not influenced by the elongation to failure of the weld material. However, dome tests might be useful in investigating failures dominated by weld movement.

8.) Two conditions must be present for weld movement; a difference in load bearing capacities of the two materials that it is joining and stretching perpendicular to the weld. This combination forces the weaker material to deform more and the weld moves in the direction of the stronger material to compensate for it. If either a force normal to the weld is absent (*OSU Formability Test*) or there is no difference in strength of the parent materials (0.8 mm/0.8 mm AKDQ LDH), no weld movement will be observed. The severity of the weld movement is of course dependent on the strength ratio of the materials and the magnitude of the boundary forces.

9.) FEM can be used to predict the trends of the influence on weld movement of the following variables:

a.) The global friction

b.) The local friction of the weld (mash seam especially)

c.) Weld geometry

d.) Weld mechanical properties.

However, the error in the measurement of weld movement of a tailor welded blank in a research setting was determined to be ±0.25 mm, and the amount these variables influenced the weld movement was on that order. Therefore, the influence of these variables on the weld movement is negligible and these properties can ignored in the model with no major error in results.

10.) In experiments using the scale fender die on the *Hydraulic Forming Simulator*, it was found that increasing lubrication made large improvements in formability, mostly by allowing more material to flow into the die. It was found the weld movement was invariant to the lubrication conditions.

11.) A simple analytical model to represent a punch stretch operation of a tailor welded blank was developed. The resulting predicted strains and weld movement was also predicted by a 2-D FEM code, SHEET-S. This model predicted the weld movement would increase as the fraction of the weaker material increased.

LIST OF REFERENCES

1. N. Nakagawa, S. Ikura, and F. Natsumi: *Finite Element Simulation of a Laser-Welded Blank*, SAE Paper #930522, 1993

2. M. F. Shi, K. M. Pickett and K. K. Bhatt: *Formability Issues in the Application of Tailor Welded Blank Sheets*, SAE Paper #930278, 1993

3. Y. S. Yang, C. R. Hsu, C. E. Albright, and Y. Kuroda: *Heat Flow in Laser Die Blank Welding*, submitted for publication

4. B. Irving; *Blank Welding Forces Automakers to Sit Up and Take Notice* , Welding Journal, Sept. 1991

5. Jay Baron, private communication

6. Kumar Bhatt, private communication

7. J. Baysore, *Welded Sheet Metal Blanks: An Application and Process Overviw*, Internal Report, Utilase Blank Welding Technologies

8. K. M. Radlmayr, J. Szinyur, *Laser Welded Sheet Panels for the Body In White*, IDDRG Working Groups Meeting, PISA, Italy Palazzo dei Congressi, 7-9 May, 1991

9. K. Schmidt, *Growing Sheet Metal Stamping Blanks*, Metal Forming, Sept. 1991, p. 43

10. B. Van Otteren, R. Rodriguez, D. Alexander, M. Toth, B. Vanden Bosch, *Hardness Reduction of a Mash Seam Weld Using the Hot Planih Process*, Internal Report, Newcor Bay City, 1846 Trumbull Drive, Bay City, MI 48707-0918

11. K. Azuma, K. Ikemoto, K. Arima, H. Sugiura and T. Takasago: *Proc. of 16th Biennial IDDRG Congress*, ASM International, 1990

12. N. Iwata, M. Matsui, N. Nakagawa, and S. Ikura, *Improvements in finite element simulation for stamping and applications to the forming of laser-welded blanks,* NUMISHEET '93, Proceedings of 2nd International Conference on Numerical Simulation of 3-D Sheet Metal Forming Processes, Isehara, Japan 31 August - 2 September 1993, Eds. A. Makinouchi, E. Nakamachi, E. Onate, R.H. Wagoner

13. A. Erichsen: German Patent No. 260180 6 July,1912

14. M. Gotoh, *An Improvement in the Theory of Plastic Orthotropy by Biquadrdic Yield Function (Plane Stress State) 1 and 2,* Journal of the JSTP, Vol. 19, No. 208 p. 377 (1978) and Vol. 19 No. 210 p. 599 (1978)

15. B. Y. Wang, M. F. Shi, H. Sadrina and F. Lin: *Structural Performance of Tailor Welded Sheet Steels,* to be published at 1995 SAE Congress

16. S.S. Hecker: *A Cup Test for Assessing Stretchability,* Metals Engineering Quarterly, 1974, vol. 14, p. 30

17. A.K. Ghosh: *The Effect of Lateral Drawing-In on Stretch Formability,* Metals Engineering Quarterly, 1975, vol. 15, pp. 53-64

18. R. A. Ayres, W. G. Brazier and V. F. Sajewski: *Evaluating the GMR-Limiting Dome Height Test as a New Measure of Press Formability Near Plane Strain,* J. Appl.Metalworking, vol. 1, no .1, pp. 41, 1979

19. NADDRG Round Robin Test Evaluation, Summer, 1989

20. LDH Committee/NADDRG, Final Report of the LDH Committee, May 1990

21. D.J. Meuleman, J.L. Siles, and J.J. Zoldak: *The Limiting Dome Height Test for Assessing the Formability of Sheet Steel,* SAE Paper 85005, 1985, pp. 1-9

22. M.P. Miles, *A Better Sheet Formability Test,* M.S. Thesis, Dept. of Materials Science and Engineering, The Ohio State University, 1991

23. M.P. Miles, N. Krishnaiyengar, R.H. Wagoner, and J.L. Siles, *A Beeter Sheet Formability Test,* Metall. Trans. A, May 1993

24. F. I. Saunders and R. H. Wagoner, *Finite Element Modeling of a New Formability Test,* Computer Applications in Shaping and Forming of Materials, eds. M. Demeri, Symposium at 1993 TMS Annual Meeting, Denver, Co.

25. Y. S. Suh and R. H. Wagoner, *Optimized Design of Tooling of The New Formability Test Using FEM,* Computer Applications in Shaping and Forming of Materials, eds. M. Demeri, Symposium at 1993 TMS Annual Meeting, Denver, Co.

26. ABAQUS, v.5.2 at the Ohio Supercomputer Center, under academic licence from Hibbitt, Karlsson & Sorensen, Inc., Pawtucket, R. I., 1993

27. Y. Germain, K. Chung and R.H. Wagoner: *A Rigid-Visco-Plastic Finite Element Programs for Sheet Metal Analysis,* Int. J. Mech. Sci., 1989, Vol. 31, No. 1, pp 1-24

28. J.R. Knibloe and R.H. Wagoner: *Experimental Investigation and Finite Element Modeling of Hemispherically Stretched Sheet,* Metall. Trans. A, 1989, vol. 20A, pp. 113-123

29. C.T. Wang, and R.H. Wagoner: *Square Punch Forming: Experiments and Simulations in 2-D and 3-D,* J. Mech. Working Tech., 30 (1992) 173-196

30. T.B. Stoughton, *Finite element modeling of 1008 AK sheet steel stertched over a rectangular punch with bending effects,* Computer Modeling of Sheet Metal Forming Process: Theory, Verification and Applications, The Metallurgical Society of AIM, Warrendale, PA., 1986, pp. 143-160

31. Y.T. Keum, E. Nakamachi, R.H. Wagoner and J.K. Lee: *Compatible Description of Tool Surfaces and FEM meshes for Analyzing Sheet Forming Operations,* Int. J. Num. Meth., vol. 30, 1471-1502

32. R. H. Wagoner and D. Zhou: *Analyzing sheet forming operations - Recent numerical and experimental advances,* NUMIFORM '92 - Proceedings on the 4th International Conference on Numerical Methods in Industrial Forming Processes, Valbonne, France, 14-18 September 1992

33. D. Zhou and R. H. Wagoner, *Development and Application od Sheet Forming Simulation,* NUMISHEET '93, Proceedings of 2nd International Conference on Numerical Simulation of 3-D Sheet Metal Forming Processes, Isehara, Japan 31 August - 2 September 1993, Eds. A. Makinouchi, E. Nakamachi, E. Onate, R.H. Wagoner

34. FE-Simulation of 3-D Sheet Metal Forming Processes in Automotive Industry (Proceedings Conference held May 14-16, 1991, Zurich, Switzerland) VDI Berichte 894, VDI-Verlag GmbH, Dusseldorf, 1991

35. NUMISHEET '93, Proceedings of 2nd International Conference on Numerical Simulation of 3-D Sheet Metal Forming Processes, Isehara, Japan 31 August - 2 September 1993, Eds. A. Makinouchi, E. Nakamachi, E. Onate, R.H. Wagoner

36. Dr. Gary Neiheisel, Armco Research and Technology, 705 Curtis St., Middletown, Oh 45043

37. Tim Webber, Hobart Laser Products, 332 Earthart Way, Livermore, CA 94550

38. Bob van Otteren, Newcor Bay City, 1846 Trumbull Dr., Bay City, Mi 48707-0918

39. Ming Shi, National Steel, Product Application Center, 12261 Market St., Livonia, MI 48150

40. The Department of Materials Science and Engineering, The Ohio State University, Columbus, Ohio 43210

41. Data Translation, Marlboro, MA 01752

42. ASTM Standard E-8, American Standard of Testing of Materials

43. Instron Corporation, Canton, Mass. 02021

44. Interlaken Technology Corp. Eden Prarie, MN 55346

45. Y. Hishida and R. H. Wagoner, *Experimental Analysis of Blank Holder Force Control in Sheet Forming*, SAE Paper # 930285, 1993

46. Y. Hishida and R. H. Wagoner, *Hydraulic Forming Simulator and Tester*, Proceedings of the 1992 NSF Design and Manufacturing Systems Conference, Atlanta, GA, January 8-10, 1992

47. R. Hill: *Proc. Roy. Soc.*, 1949, vol. 198, p. 428

48. A. Parmer and P.B. Mellor: *Predictions of Limit Strains in Sheet Metal Using a More General Yield Criterion*, Int. J. Mech. Sci., 1978, vol. 20, pp. 385-392

49. W.F. Hosford, *A Generalized Isotropic Yield Criterion*, J. Appl. Mech., 1972, E39, pp. 607-609

50. S. S. Hecker, J. Eng. Mater. Technol., Trans. ASME, Vol. 97H, 1975, p. 66

51. M.S. Caceci, W.P. Cacheris: *Byte*, 1984, p. 340

52. J.H. Holloman: Trans. AIME, 1945, vol. 162, p. 268

53. E. Voce, *J. Inst. Met.*, 1948, vol. 74, pp. 537, 562 and 760; *The Engineer*, 1953, vol. 195, p.23; *Metallurgica*, 1953, vol. 51, p. 219

54. D. A. Stuart & Co., 7575 Plaza Court, Willowbrook, IL 60521

55. F. I. Saunders, J. M. Garrett, R. H. Wagoner, B. Smola, K . Gasper, *A New Method for Ranking Lubricants*, to be published

56. T. B. Stoughton, *Model of Drawbead Forces in Sheet Metal Forming*, Proceedings of 15th IDDRG, pp. 205-215

APPENDIX A

WELD METAL EVALUATION

1. Microhardness

In order to understand the macroscopic forming behavior of the different types of welds, one must investigate the microstructure and properties of the actual weld metal itself. At this point, microhardness testing and metallographic inspection of the 5 different welds have been completed. Because of the observed presence of cracks in the mash seam welds, non destructive evaluation will be carried out to check the severity of the cracks and if that would explain the poor forming behavior of the mash seam welds.

The samples to be tested for microhardness were sectioned and hot press mounted in either black or red phenolic. Microhardness testing was performed on a Buehler Micromet II Digital Micro Hardness Tester at The Ohio State University. Each sample was polished through 600 grit silicon carbide paper and then finished polishing with 0.3 micron diamond paste on a Buehler polishing wheel. To make the actual microhardness indention, a load of 500 grams was held for 10 seconds on a Vickers hardness indenter. After measuring the dimensions of the diamond, the machine automatically calculated the Vickers number, so no conversion tables were needed.

The microhardness indentions were taken along a straight line across the cross section of the weld. For the HSLA/AKDQ welds, they were centered in the center of both samples, since the thickness was nearly the same. For the 0.8/1.8 welds, the line of indentations started at the center of the 0.8 mm material, so when it went into the 1.8 mm material, it was near the bottom edge.

Figures 74 through 83 show the microhardness as a function of position from the center of the weld. Figures 74 and 75 show the microhardness profiles for the CO_2 Laser welds for both the HSLA/AKDQ combination and the 0.8 mm/1.8 mm AKDQ combination. Even though the hardness of the base HSLA is

much higher than the AKDQ, the peak hardness of the HSLA/AKDQ weld is not that much greater than that of the 0.8/1.8 weld. The highest hardness for the HSLA/AKDQ weld is 348 Vickers, while the maximum hardness of the 0.8/1.8 is 338 Vickers. This would probably be attributed to the likely formation of martensite in the solidification region of the weld zone. The hardness in martensite is a very strong function of carbon content. Since the difference in carbon content is not that different between HSLA and AKDQ (Table 2), the peak martensite hardness should be similar. The size of the actual weld bead is also very similar. For the 0.8/1.8 weld, the weld size is about 0.8 mm. The HSLA/AKDQ is slightly smaller, at approximately 0.5 mm. The edge of the weld was defined as the position of the midway point between the peak hardness of the weld and the average hardness of the base material.

The microhardness plots for the YAG laser weld would be expected to be almost the same (Figures 76 and 77), but are significantly different in actual magnitude. The peak hardness of the welds are significantly lower than that of the CO_2 laser weld. The peak for the solid state weld zones are only 277 Vickers for the 0.8/1.8, and 253 Vickers for the HSLA/AKDQ. These values are nearly 100 points below the CO_2 laser, which is rather suprising. As mentioned before, it was decided that the process conditions for the two laser welds would be identical for this study. Therefore, there must be some fundamental difference between the two lasers to cause this obvious difference in hardness. Also, the size of the YAG laser weld seems to be slightly larger from the microhardness plots. The approximate width seems to be around 0.4 mm for the 0.8/1.8 weld and closer to 0.6 mm for the HSLA/AKDQ.

Figures 78 through 83 show the different microhardness plots for the mash seam welds. Overall, the hardness values for the mash seam weld are

significantly lower. The distributions for mash seam, weld only are shown in Figures 78 and 79. Note not only difference in hardness but also the difference in size of the weld. Actually the difference in hardness is not all that much different between the YAG welds and the mash seam, weld only weld zones for the HSLA/AKDQ. The peak hardness is 244 Vickers for the mash seam weld, while it was 253 Vickers for the YAG. The difference in the 0.8/1.8 welds is much more significant; the peak hardness for the mash seam weld is only 160 Vickers while it was 277 Vickers for the solid state laser. The huge difference between these two welds is the unbelievable difference in size. If you notice the plot of the mash seam HSLA/AKDQ, the hardnesses at the outer edges of this plot are 195 Vickers for the HSLA end and 148 Vickers for the AKDQ end. This is well above the microhardness values for the base materials (155 Vickers for the HSLA and 95 for the AKDQ). Even though this plot covers 12.5 mm, the heat affected zone is still larger than that. The 0.8/1.8 weld is not nearly as large, but still significantly larger than the laser weld. It is also a much more gradual change than that of the laser welds, where there was a significant drop off in hardness nearly instantly. It looks like the heat affected zone spans about 6 mm, which is less than half of the HSLA/AKDQ weld zone, but still many times larger than the laser weld zone.

Figures 80 and 81 are the plots for the mash seam planished welds. As mentioned before, planishing is a process where the weld is plastically deformed directly after the welding has taken place to improve the surface condition of the weld. The drawback of this process is a large amount of cold work is supposedly being put into the weld, therefore reducing the ductility of the weld significantly. Also, the hardness of this weld would be expected to be reduced dramatically. This did hold true for the 0.8/1.8 weld. The peak measured hardness of this

weld is 204 Vickers compared to 160 Vickers for a not planished sample. This was not the case for the HSLA/AKDQ welds though. The peak hardness of the cold planished sample was 227 Vickers, while it was 243 Vickers for the weld only sample. This is a very suprising result. It will require investigation of the microstructure of the material to truly understand why this occurred. The dimensions of the heat affected zone for the planished samples are comparable to that of the of the weld only sample. For the HSLA/AKDQ weld, the width across the heat affected zone is about 7.5 mm, while it is about 7 mm for the 0.8/1.8 weld. This is very comparable to the weld zone dimensions for the weld only 0.8/1.8.

The last type of mash seam weld is the hot planished weld. The hot planishing, as mentioned before, is a heat treatment of the weld that is meant to relieve the work hardening that was put into the weld through the planishing step. Therefore, the microhardness values for these welds would be expected to be significantly lower than that of the planished welds. Figures 82 and 83 show the microhardness plots for both material and thickness combinations. In Figure 82, the microhardness plot shows a significantly lower microhardness for the hot planished HSLA/AKDQ weld as opposed to the planished HSLA/AKDQ weld (175 Vickers for hot planished and 227 Vickers for cold planished). A similar result was found for the 0.8/1.8 welds, but not to the same extent as was found for the HSLA/AKDQ welds (181 Vickers for hot planished, 207 Vickers for cold planished). The weld zones are also similar compared to the other mash seam welds. For the HSLA/AKDQ weld, the weld zone is approximately 8 mm while the 0.8/1.8 weld is about 5 mm. Again, it is very difficult to determine the actual weld size in the mash seam welds because of the gradual increase in hardness

(corresponding to slowly changing microstructure) as opposed to the laser welds, where a change in microstructure occurs almost instantly.

2. Micro structural evaluation

With such a difference in the microhardness of the weld material, an investigation of the microstructure of the weld material was necessary. A knowledge of the structure of the weld would give the information needed to determine the reason for the microhardness behavior. As for the microhardness samples, the samples for microstructural evaluation were sectioned out of the weld and hot-press mounted in either black or red phenolic. The surface of the samples were polished with 240,320,400 and 600 grit silicon carbide paper. They were polished with 0.3 micron diamond paste and then finished with 0.015 micron diamond paste on a Buehler polishing wheel. The sample was then etched with an 0.2% nital solution for 10 seconds, and then observed and photographed with a Nikon optical microscope.

Figure 84 shows the overall microstructure of the CO_2 laser weld for the HSLA/AKDQ. There is an obvious difference in microstructure between the HSLA and AKDQ; the AKDQ has a much larger grain size than the HSLA. The weld zone is also obvious in the microstructure; the weld structure is martensitic and there is a definite transition line between the weld metal and the base metal, especially on the HSLA side. There is a slight change in grain size of the HSLA right near the planar interface, but it is a very small region. On the AKDQ side, there is a significant change in structure, but there appears to be a small amount of transitional martensitic phase dispersed throughout the ferritic grain structure close to the weld metal.

Figure 85 shows the CO_2 laser weld for the 0.8/1.8 combination. Again the weld metal structure is martensite. The interface between the weld metal and 1.8 mm material is nearly planar; there appears to be no transitional phases. However, on the 0.8 mm side, there seems to be islands of martensite scattered throughout the ferrite, just as on the AKDQ side of the HSLA/AKDQ weld.

The structure of the 0.8/1.8 YAG weld is shown in Figure 86. The structure is very similar to that of the CO_2 laser weld, except the weld region is slightly larger in the YAG, as shown in the microhardness tests. Also, the martensitic structure seems to be coarser in the YAG. Coarser martensite would mean the plates of the martensite is spread further apart. A coarser martensitic structure would result in a lower hardness, which is observed for the YAG.

The AKDQ/HSLA weld microstructure for the YAG is also very similar to the structure of the HSLA/AKDQ CO_2 weld material. In Figure 87, the YAG weld is observed to have a martensitic structure in the center of the weld region. On the HSLA side, there is a two phase transition region between the HSLA base material and the weld zone. This region and the actual solidification region itself in the YAG weld is much larger than in the CO_2 weld. Also, on the AKDQ side, the islands of martensite scattered in the ferrite adjacent to the weld zone are observed in the YAG weld also.

Figures 88 through 93 show the microstructure of the mash seam welds. With the three different types of processing on the mash seam welds, there should be a wide range of microstructures that will hopefully explain the microhardness results.

The microstructure for the mash seam weld only, 0.8/1.8 combination is shown in Figure 88. At a first glance, the microstructure is remarkably different between the mash seam welds and the laser welds. First, there is not the well

defined weld zone region as there was for the laser welds. In fact, there seems to be almost no solidification region at all. The microstructure seems to be almost all ferrite, with about the same grain size as the base material. The only difference is there is a definite line that angles through the weld region, which was probably the original interface between the two sheets. It is believed that this line is a result of overheating [6].

Figure 89 shows the microstructure of mash seam, cold planished weld for the 0.8/1.8 combination. It is a much more complex structure than that of the mash seam weld only. This microstructure was much different than what would have been suspected. Similar to the mash seam weld only, the planished weld did have the same diagonal line dividing the two different original sheets. This time, however, there was a definite difference in the microstructure dividing the two different sheets. On the 0.8 mm side, the structure starts out as coarse ferrite, and as it approaches the weld region, the grain size reduces. At this dividing line, the ferrite immediately changed from the fine structure to a more coarse, blocky morphology. At the surface of the 1.8 mm AKDQ, the ferrite grains were very large. At distances further from the weld, the islands of martensite as observed in the laser welds appear in the blocky ferrite. At a certain point, there seems almost to be another definite planar interface between structures. The blocky ferrite immediately changes to the base 1.8 mm microstructure.

As mentioned before, this microstructure is much different than what would have been expected. As described earlier, the planishing step of the processing is when the weld bead, immediately after welding, is compressed between two rollers to smooth the surface of the weld. With this plastic deformation, a cold worked microstructure would have been expected in the weld region, i.e. a much finer grain size. Instead, on the 1.8 mm side, there is a

large, blocky structure. One possible explanation for this is that there is dynamic recrystallization taking place. Dynamic recrystallization is when the combination of temperature and deformation effects cause the microstructure to recrystallize. If the rollers are immediately after the weld, there might be enough heat energy when the deformation occurs to instigate recrystallization.

Figure 90 shows the mash seam hot planished microstructure for the 0.8/1.8 combination. This structure is very different than that of the cold planished sample. The grain structure is much more uniform and equiaxed. It fades from a coarse, equiaxed structure in the base material on both sides to a real fine microstructure through the central region of the weld. There is still a definite line as a result of the overheating in the center of the weld. Since hot planishing is simply a heat treatment of the weld region after the planishing, it is possible that this heat treatment caused the real fine, equiaxed microstructure in the weld region.

Figure 91 shows the weld only microstructure for the HSLA/AKDQ material. The HSLA/AKDQ structure is quite a bit different than the 0.8/1.8 structure. The 0.8/1.8 structure was mostly ferrite, but the HSLA/AKDQ structure is a mixture of a number of things. The interface line is still visible, but not to the same extent as in the 0.8/1.8 samples. The structure in the center of the weld region is a martensitic structure with some acicular ferrite. The structure is more martensite in the HSLA side and changes gradually to the HSLA microstructure. On the AKDQ side, the structure was mostly acicular ferrite. As you get further from the weld, the islands of martensite reappear and you have a two phase transitional region before entering the base AKDQ coarse ferrite.

The mash seam planished microstructure is similar to that of the mash seam weld only (Figure 92). There again is a discontinuity in microstructure,

right along the common line of overheating at the interface. On the HSLA side of the line, the structure is primarily acicular ferrite. It transforms into a very fine equiaxed ferrite structure that coarses out in the base HSLA. The AKDQ side right near the divisional line is a mixture of ferrite and martensite. Moving away from the weld, the structure turns to primarily ferrite with the islands of martensite dispersed throughout the structure. The structure eventually evolves into the coarse ferrite structure of the base AKDQ.

The mash seam hot planished microstructure is shown in Figure 93. Like the 0.8/1.8 combination, the hot planishing causes the microstructure to become more uniform and equiaxed throughout the entire weld region. Again, the diagonal line in present across the weld. The structure in the weld region is a very fine ferrite structure. Out toward the base AKDQ, the ferrite slowly becomes more coarse, until it reaches the grain size of the base AKDQ. On the HSLA side, the fine ferrite slowly evolves as a function of position to the grain size of the base HSLA.

The microstructural evaluation of the welds has explained a lot about the different welding procedures, but did not give all of the important information in terms of explaining the formability of each weld type. From the laser welds, the affected area from the welding process was very small (less than 1 mm). The structure was all martensitic, as a result of a high cooling rate. Therefore, the laser welding process involves an intense, concentrated heat source in the material that only affects a small region, and then dissipates the heat rather fast. From the structure and the hardness, the CO_2 laser seems to have a more focused beam (smaller weld zone) and dissipates the heat away quicker (much higher hardness).

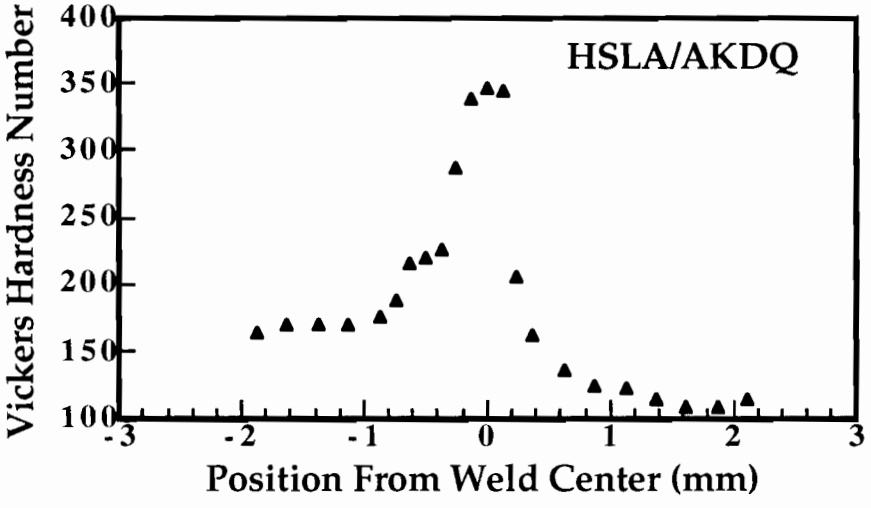

Figure 74. Microhardness plot of the weld material for the HSLA/AKDQ CO_2 laser weld.

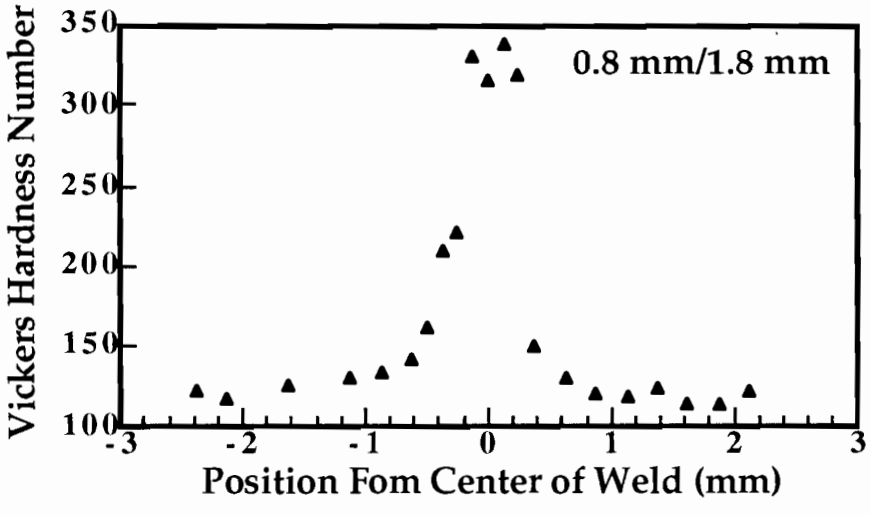

Figure 75. Microhardness plot of the weld material for the 0.8 mm/1.8 mm CO_2 laser weld.

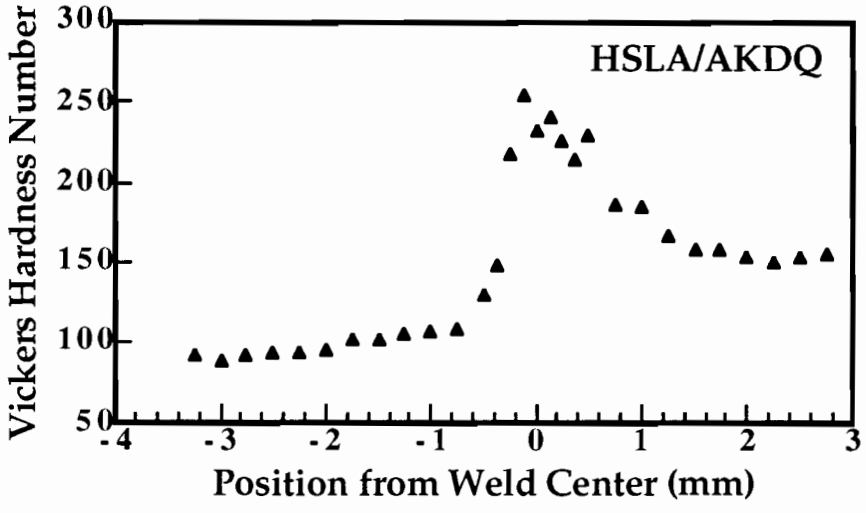

Figure 76. Microhardness plot of the weld metal for the HSLA/AKDQ YAG laser weld.

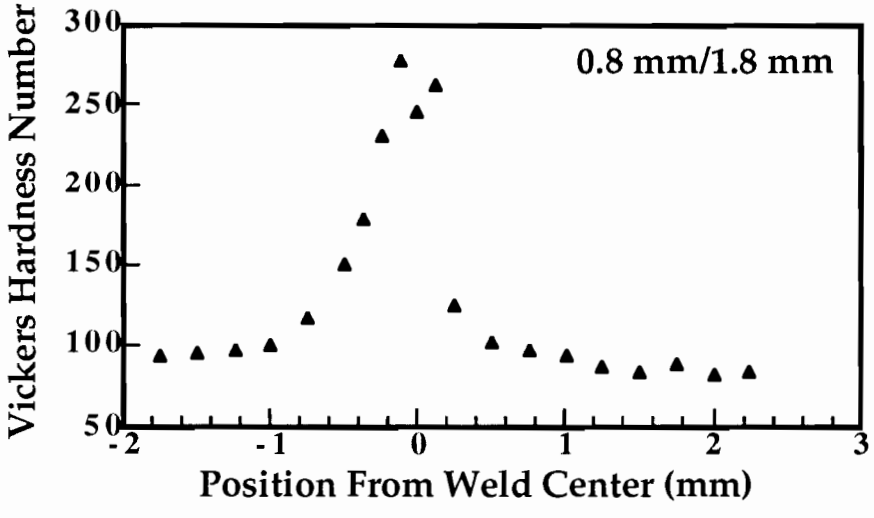

Figure 77. Microhardness plots of the weld metal for the 0.8 mm/1.8 mm YAG laser weld.

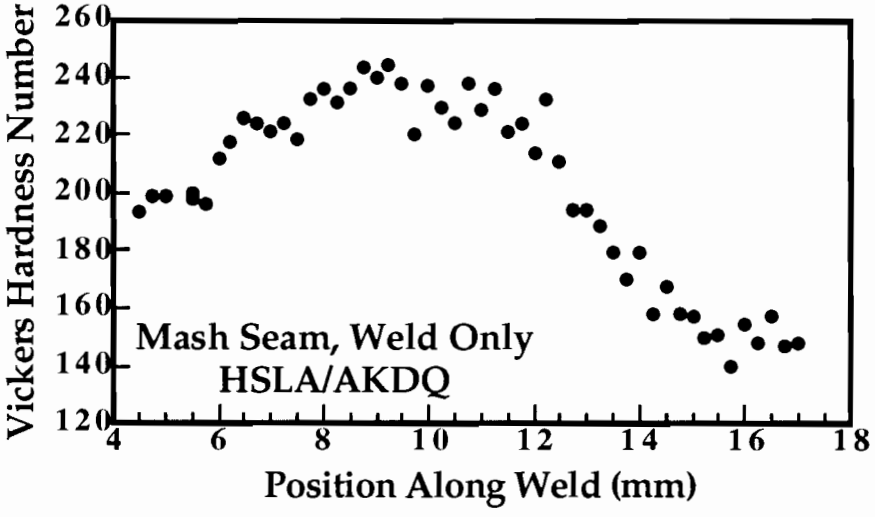

Figure 78. Microhardness plots of the weld metal for the HSLA/AKDQ mash seam weld only.

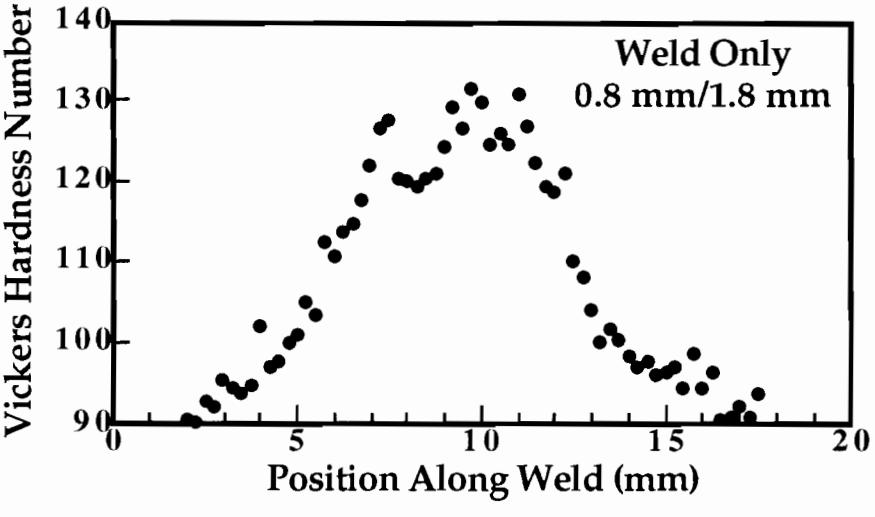

Figure 79. Microhardness plots of the weld metal for the 0.8 mm/1.8 mm mash seam weld only.

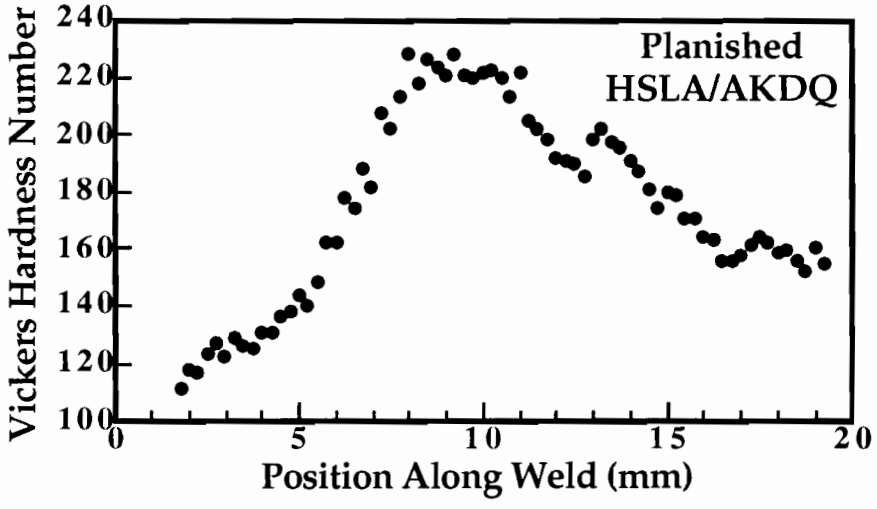

Figure 80. Microhardness plot of the weld metal for the HSLA/AKDQ mash seam planished weld.

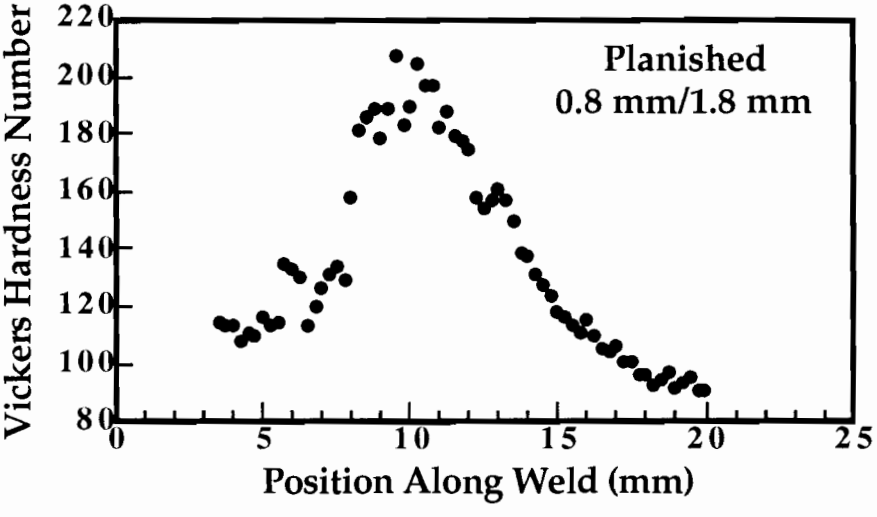

Figure 81. Microhardness plot of the weld metal for the 0.8 mm/1.8 mm mash seam planished weld.

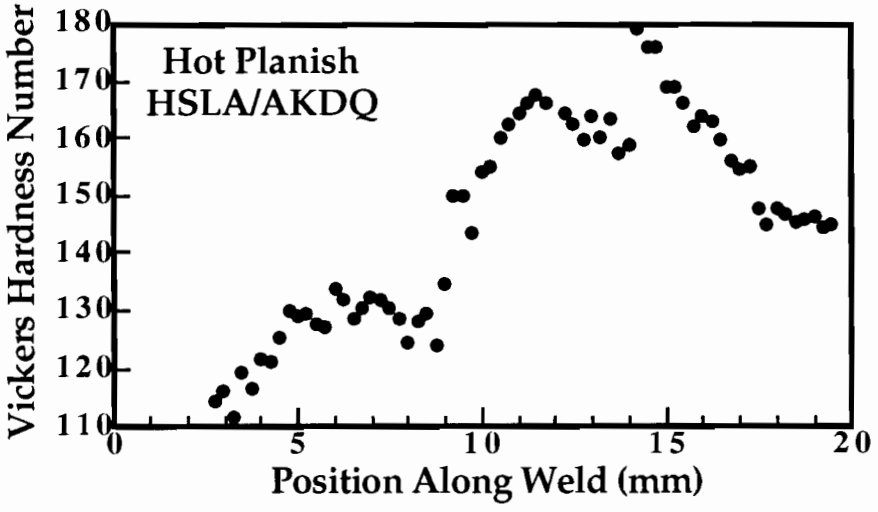

Figure 82. Microhardness plot for the weld metal across the HSLA/AKDQ mash seam hot planished weld.

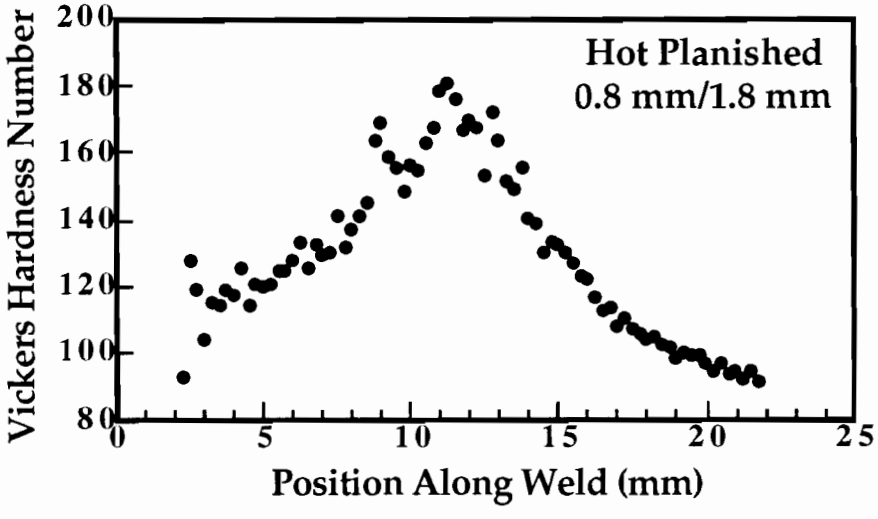

Figure 83. Microhardness plot for the weld metal across the 0.8 mm/1.8 mm mash seam hot planished weld.

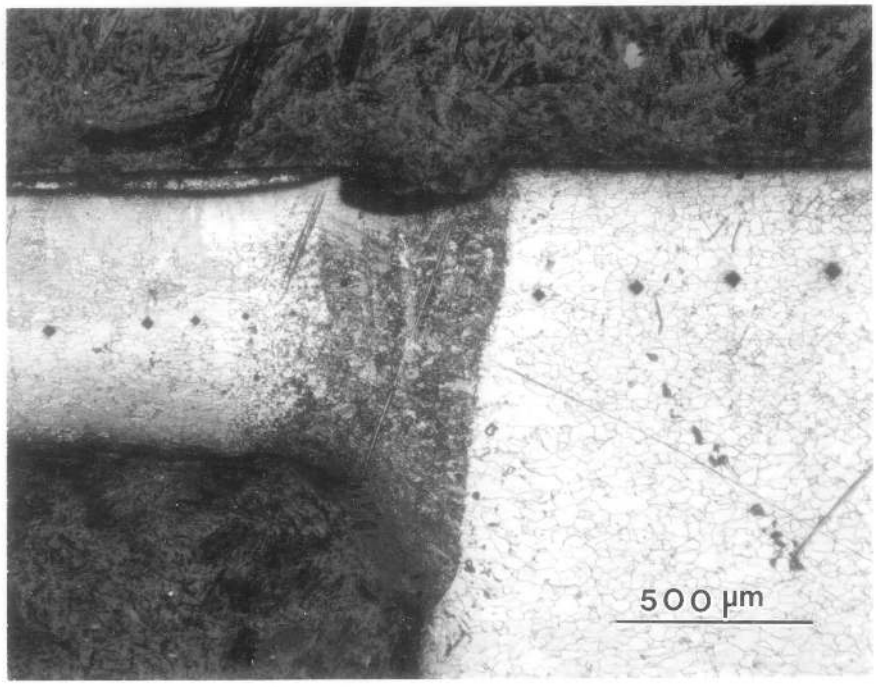

Figure 84. The microstructure for the weld bead of the CO_2 laser AK0.8/AK1.8 blank.

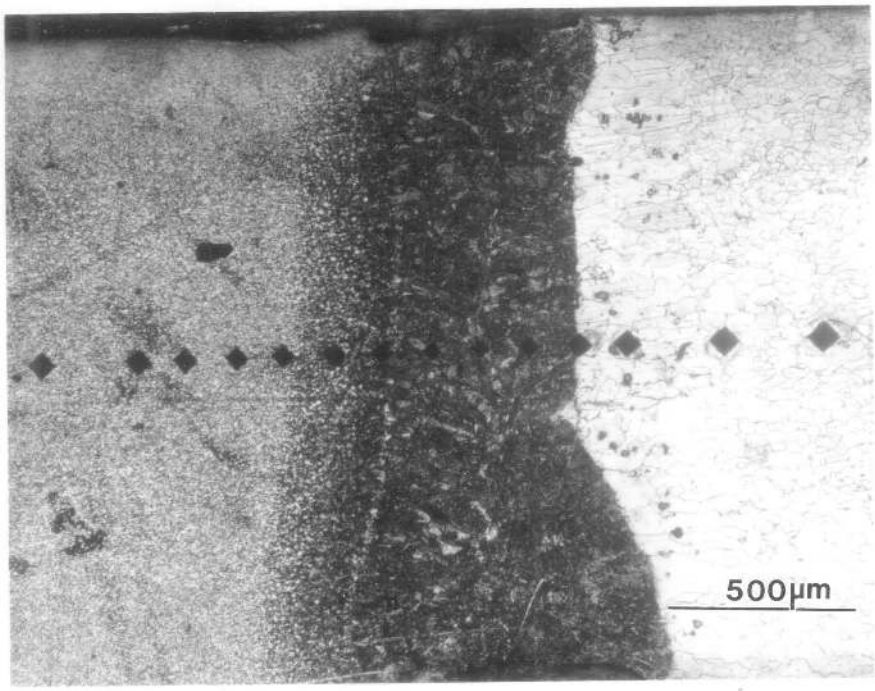

Figure 85. The microstructure for the weld bead of the CO_2 laser HS2.1/AK1.8 blank.

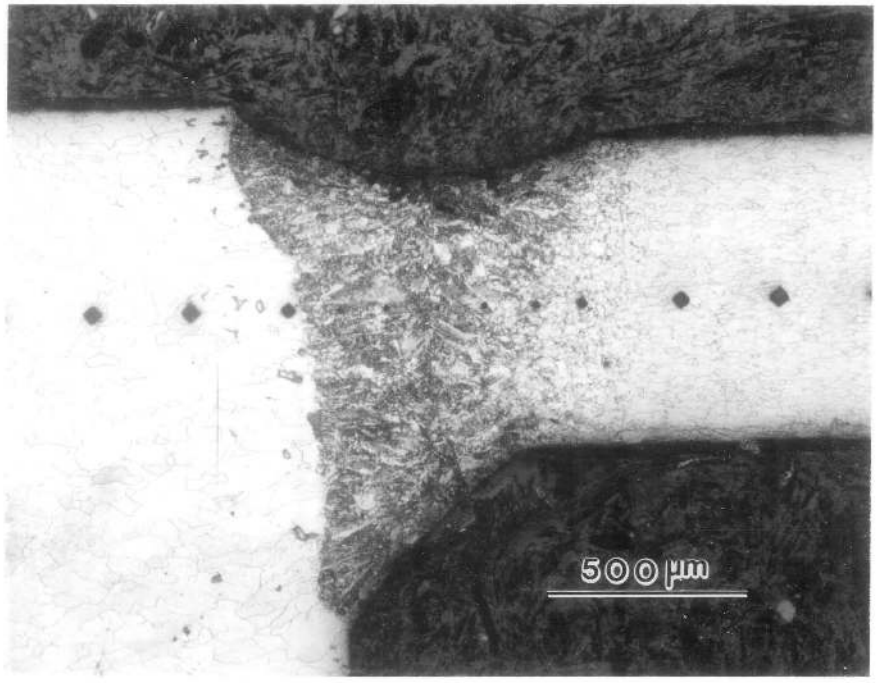

Figure 86. The microstructure for the weld bead of the YAG laser AK0.8/AK1.8 blank.

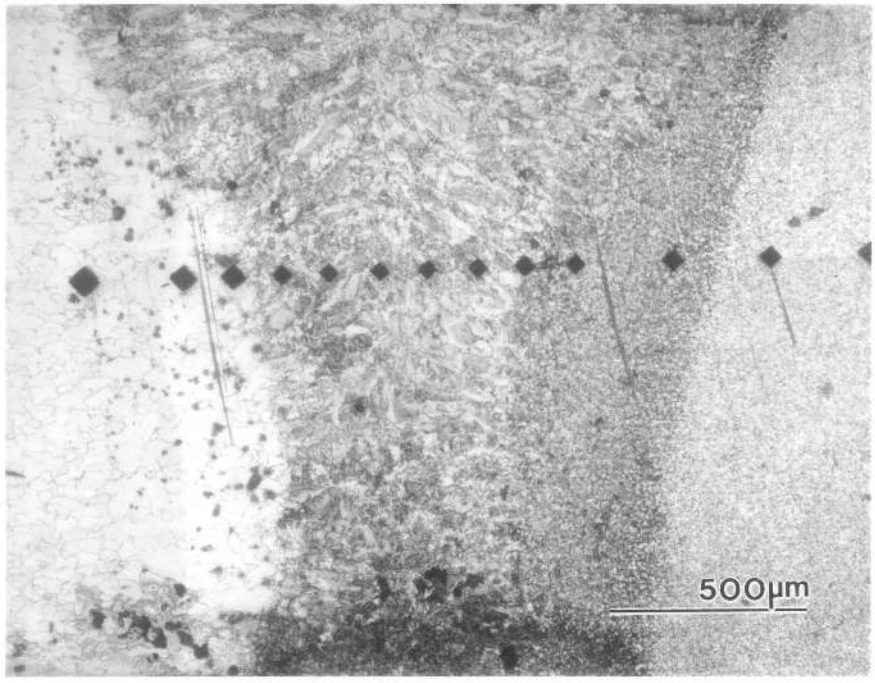

Figure 87. The microstructure for the weld bead of the YAG laser HS2.1/AK1.8 blank.

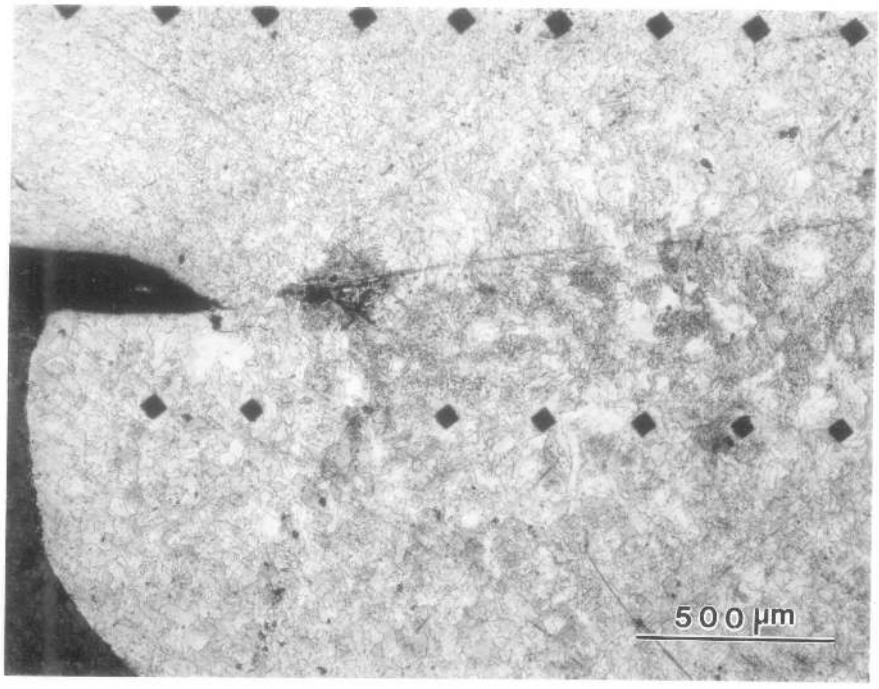

Figure 88. The microstructure for the weld bead of the unplanished mash seam AK0.8/AK1.8 blank.

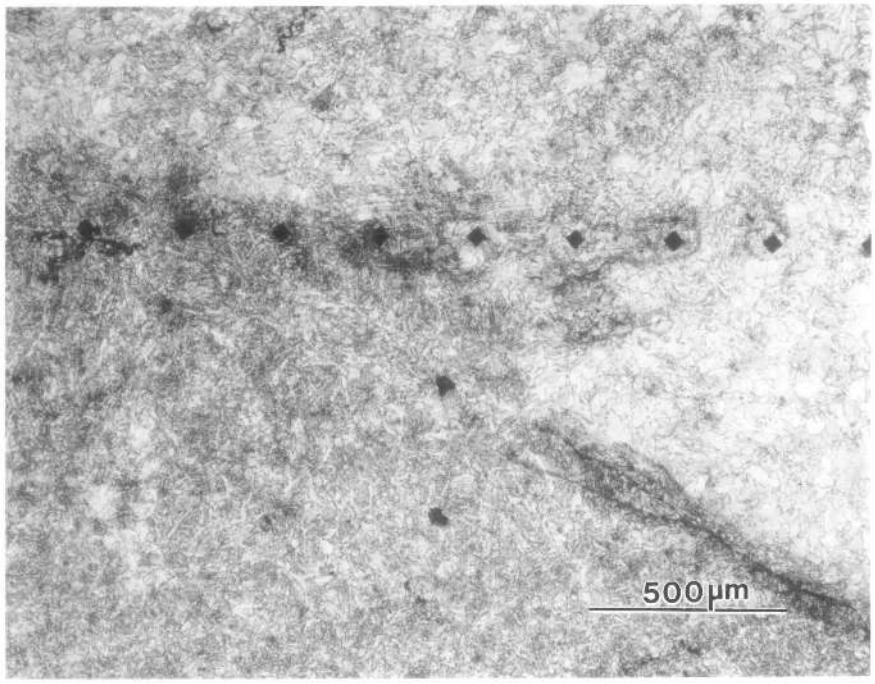

Figure 89. The microstructure for the weld bead of the unplanished mash seam HS2.1/AK1.8 blank.

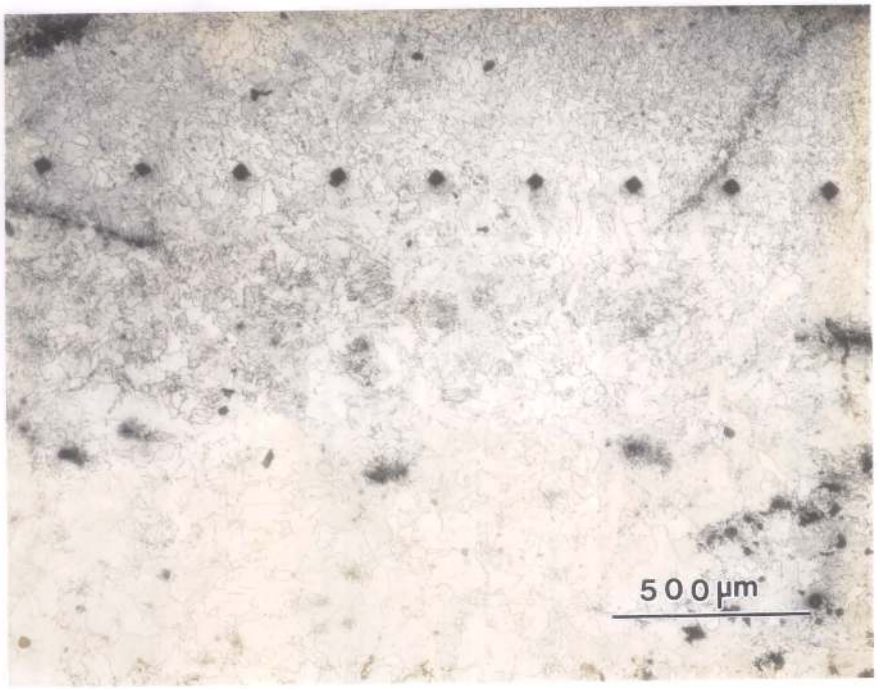

Figure 90. The microstructure for the weld bead of the planished mash seam AK0.8/AK1.8 blank.

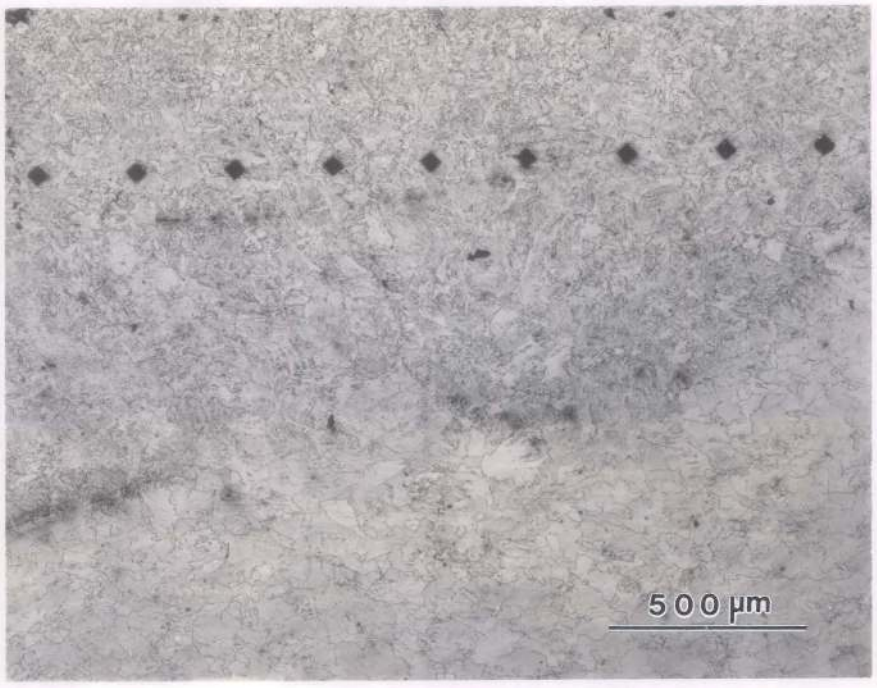

Figure 91. The microstructure for the weld bead of the planished mash seam HS2.1/AK1.8 blank.

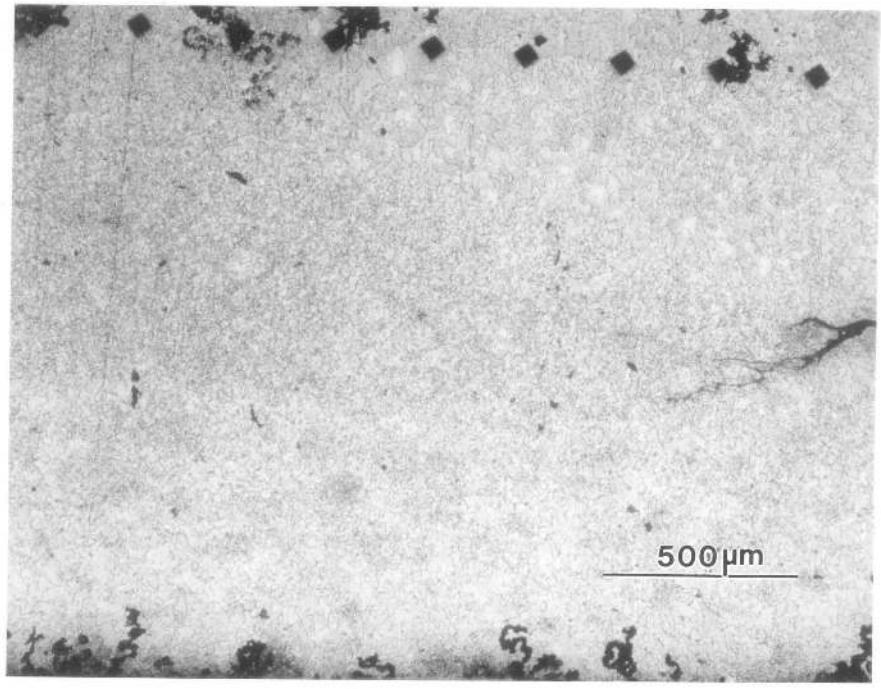

Figure 92. The microstructure for the weld bead of the hot planished mash seam AK0.8/AK1.8 blank.

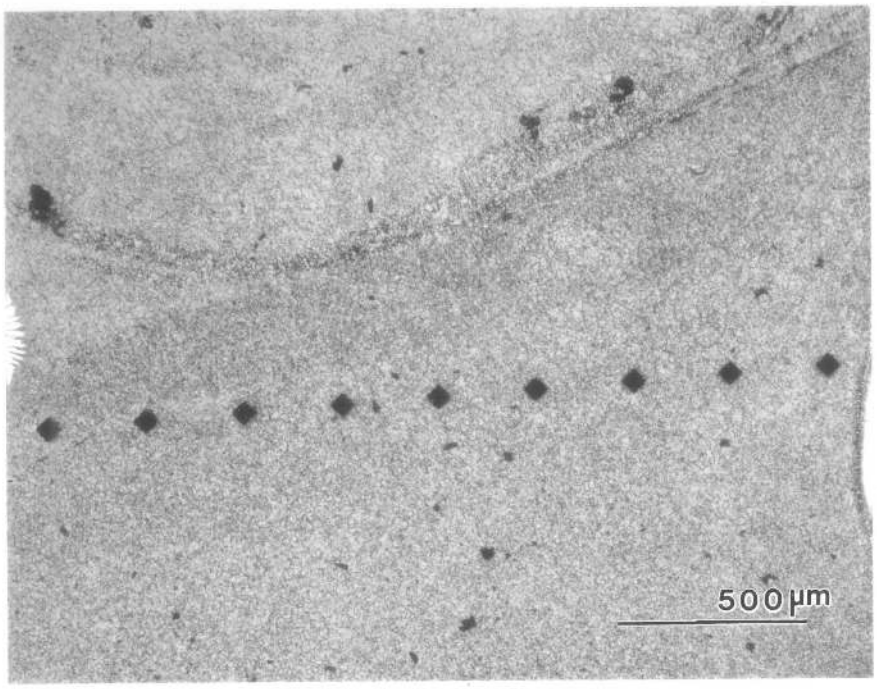

Figure 93. The microstructure for the weld bead of the hot planished mash seam HS2.1/AK1.8 blank.

APPENDIX B

ANALYTICAL METHOD FOR DETERMINING LASER WELD BEAD HARDENING LAW

The hardening laws were calculated from the measured load displacement data from the subsized tensile specimens for the laser welded blanks, as described in Chapter 5. The orientation of the weld is such that it lies parallel to the stretching direction, as shown in Figure 10 in the text.

An isostrain model is assumed, i.e. the strain in the major stretching direction is the same in base material A and base material B (we will refer to the base materials as A and B for simplicity). Therefore,

$$\varepsilon_{1,A} = \varepsilon_{1,weld} = \varepsilon_{1,B} \tag{11}$$

We also assume that all three areas are in uniaxial tension, so therefore the effective strain is be represented by the strain in the major stretching direction:

$$\bar{\varepsilon} = \varepsilon_1 \tag{12}$$

So therefore the effective strain is equal in all three regions at a given time step.

$$\bar{\varepsilon}_1 = \bar{\varepsilon}_2 = \bar{\varepsilon}_3 \tag{13}$$

We get the effective stress supported by the base materials from the hardening laws:

$$\bar{\sigma}_i = f(\bar{\varepsilon}_i) \tag{14}$$

The loads supported by these areas is backed out by knowing the initial area and the current strain, resulting in the current area. These two loads can be subtracted from the current load measured by the load cell, giving the theoretical load supported by the weld bead:

$$P_{weld} = P_{total} - (P_A + P_B) \tag{15}$$

This gives the load at a given effective strain. Knowing the original area of the weldbead from microstructure and optical microscopy and the current strain gives the current area. Thus, the effective stress is calculated at a given strain, producing your effective stress-strain relationship for the weld material.

APPENDIX C

CALCULATIONS OF BLANK BOUNDARY FORCES

I. ASSUME CONSTANT PRESSURE AROUND BLANK

The first calculation assumes that blankholder force is contacting all points of the blank equally, and this force is directly proportional to the restraining force through the friction coefficient. To do the calculation, first the load is converted to load per unit length around the circumference of the blank. For example, the blankholder force is 20,000 lbs.-f. The circumference of the blank is 62 inches. Therefore, the force per unit length around the circumference of the blank is 332 lbs/in. The program works in SI units, so these values must be converted, which gives a value of 56.5 N/mm. The node spacing on the 356 mm (14") dimension is 17.5 mm, while the node spacing on the 432 mm (17") dimension is 21.6 mm . Therefore, the force per node on the 356 mm sides is 988.75 N while the force per node on the 432 mm sides is 1220.4 N. However, this force must be translated into the forces in the direction of the blank. This is done by assuming the normal force is proportional to the tangential force through the coefficient of friction. Therefore, the normal force is multiplied by the coefficient of friction, which is 0.25, and then multiplied by 2 (two sides of the blank). This gave resistance forces of 494 N for the 356 mm direction and 619,2 N for the 432 mm direction. This produced a final weld position shown in Figure 43.

II. ASSUME FORCE IS PROPORTIONAL TO THE AMOUNT OF CONTACT

In this case the boundary forces are assumed to be proportional to the area of contact. The assumptions about contact are that the AKDQ only contacts in the region of the drawbead, and all of the HSLA contacts at all points because of the difference in thickness. There is no assumption made about the resistance

force of the drawbead, however. The area of contact for the HSLA is calculated, and the area of contact of the AKDQ in the drawbead is calculated. The blankholder force is divided by this entire area. The blankholder force is 20,000 lbs-f, and the entire area 92.25 in^2, giving at total pressure of 216 psi. The area of the HSLA region is 63 in^2, which gives a total force of 13,608 lbs-f acting in that area. For the drawbeads on the 432 mm side, the area was 9.35 $_{in}2$, giving a total force for each side in the AKDQ of 2025 lbs-f. At the end, the AKDQ was in contact with the drawbead for 10.5 $_{in}2$, giving a total force for that region of 2268 lbs-f. These forces were again split up into a force per unit length and distributed along the nodes. The force per node in the HSLA was 2632 N, the 356 mm side with AKDQ had 721 N and the 432 mm side with AKDQ had 721 N per node as well. Converting to resistance force, as in the previous section, gives 1316 N per node resistance force in the HSLA region, and 360.5 N per node resistance force in the AKDQ region. These values would not even produce convergence.

III. STOUGHTON [56] BOUNDARY FORCE MODEL

The following model was proposed by Stoughton [56] for a description of the restraining force on a drawbead. Stoughton's model is expressed in terms of material properties, the drawbead geometry and the coefficient of friction. It allows for the partially penetrated bead by reducing the contact area and the curvature of the sheet over the bead. The forces are calculated by equating the work required to pull the sheet through the drawbead to the work required to bend and straighten the sheet and overcome the frictional forces in sliding over the bead radii [56].

First, Stoughton establishes that the material follows a Holloman type hardening law with strain rate sensitivity:

$$\sigma = K\varepsilon^{n} f(\dot{\varepsilon}, \dot{\varepsilon}_0, m) \tag{16}$$

where

$$f(\dot{\varepsilon}, \dot{\varepsilon}_0, m) = \left(\frac{\dot{\varepsilon}}{\dot{\varepsilon}_0}\right)^{m} \tag{17}$$

In order to calculate the forces you must know the contact angle. The contact angle in Figure 94 is given by:

$$\theta = \tan^{-1}\left(\frac{p(2-p)}{2(1-p)}\left(1-\varepsilon\frac{p(2-p)}{2(1-p)}\right)\right) \tag{18}$$

where:

$$p = {}^{d}\!/\!_{(2R+t)} \tag{19}$$

where d is the bead depth, R is the bead radius, at is the thickness of the sheet. When there isn't full bead penetration, the effective curvature is defined as

$$\frac{1}{R_{eff}} = \frac{\sin(\theta)}{R} \tag{20}$$

The effective strain on the outer fiber must also be defined:

$$\varepsilon_m = \frac{1+r}{\sqrt{1+2r}}\log\left(\frac{1+t/R_{eff}}{1+t/2R_{eff}}\right) \tag{21}$$

For calculating the work of bending a sheet specimen, Stoughton assumed the principle of equipartition of energy, so the work required to stretch the outer fibers equally the force to compress the inner fibers. Therefore, by simply doubling the work done on the outer fibers, the force to pull a sheet through a bend is [56]:

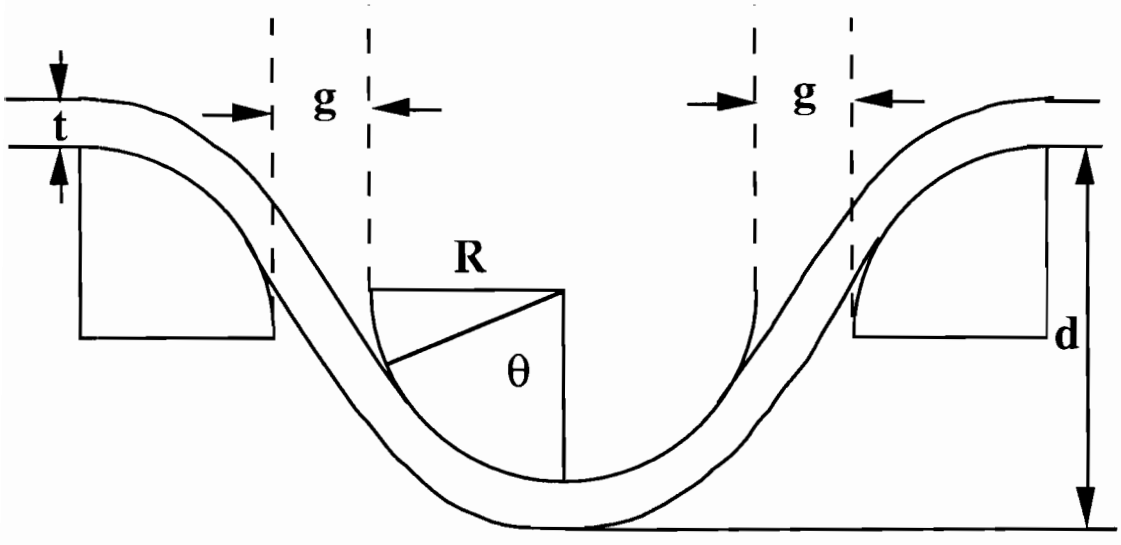

Figure 94. Schematic of drawbead geometry [56].

$$F_i = 2w\int_{t_i/2}^{t_i} dy \int_{\varepsilon_i}^{\varepsilon(y)} \sigma d\varepsilon \tag{22}$$

The strain at a distance y from the center of the sheet can be defined by:

$$\varepsilon(y) = \varepsilon_i + \frac{1+r}{\sqrt{1+2r}} \log\left(\frac{1+y/R_{eff}}{1+t_i/2R_{eff}}\right) \tag{23}$$

The strain rate at a distance y from the center of the sheet is:

$$\dot{\varepsilon}(y) = \varepsilon(y)\frac{v}{t_i}\left(\frac{1+y/R_{eff}}{1+t_i/2R_{eff}}\right) \tag{24}$$

combining and integrating Eqs. 16, 17, 21, 22 and 23 results in a force to bend the material defined as:

$$\begin{aligned} F_i = {} & \frac{wt_iK}{1+n}\left(1+\frac{2R_{eff}}{t_i}\right)\left(\frac{1+2r}{(1+r)^2}\right) \\ & \frac{1}{2+n}\left(a\frac{1+r}{\sqrt{1+2r}} - b\varepsilon_i\right)\left((\varepsilon_i+\varepsilon_m)^{2+n} - \varepsilon_i^{2+n}\right) \\ & + \frac{1}{3+n}b\left((\varepsilon_i+\varepsilon_m)^{3+n} - \varepsilon_i^{3+n}\right) \\ & - \left(a\frac{1+r}{\sqrt{1+2r}} + \frac{1}{2}b\varepsilon_m\right)\varepsilon_m\varepsilon_i^{1+n} \end{aligned} \tag{25}$$

To calculate the restraining force, the following procedure was developed [56]. First, referring to Figure 94, the unstrained material of thickness t is bent to an effective radius of R_{eff}. The resulting force for this operation is F_1 (calculated from the bending equation, 18). The force is increased because of the friction. It is enhanced by a factor $e^{\mu\theta}$.

There is an additional friction force from elastic displacement defined by:

$$F_e = \frac{2Ew\delta t^3}{(2R+g)^3} \tag{26}$$

where δ is the displacement of the bead needed to yield the material and g is the gap between the bead and the blank. This results in an addition force of μF_e.

The thickness and strain after the bend is defined as:

$$\varepsilon_{i+1} = \varepsilon_i + \gamma\varepsilon_m \tag{27}$$

$$t_{i+1} = t_i e^{-\gamma\varepsilon_m} \tag{28}$$

Stoughton [56] suggests using a value of 0.25 for γ. The additional forces to unbend and then rebend, F_2 and F_3, can be calculated with current strain and thickness in equation 25. All the forces up to this point must be increased again by a factor of $e^{2\mu\theta}$ for sliding over the center bead radius. There is also another elastic force addition at the last point of contact.

The material is unbent and rebent again, giving F_4 and F_5, using equation 18 again with current thickness and strain. An additional contribution from the initial elastic displacement occurs at the first point of contact with the exit bead

radius followed by a frictional factor $e^{\mu\theta}$. Finally, another unbending force, F_6, is added.

The drawbead restraining force is given by:

$$DBRF = \left(\left(F_1 e^{\mu\theta} + \mu F_e + F_2 + F_3\right)e^{2\mu\theta} + \mu F_e + F_4 + F_5\right)e^{\mu\theta} + F_6 \qquad (29)$$

In the current study eqs. 25 through 29 were implemented in a computer code to calculate the drawbead restraining forces. The following constants were used in the calculation:

Friction Coefficient = 0.25 (dry), 0.10 (lubricated)

K = 500 MPa (AKDQ), 585 MPa (HSLA)

n = 0.20 (AKDQ), 0.00 (HSLA)

t = 1.8 mm (AKDQ), 21.4 mm (HSLA)

w = 21.5 mm or 17.5 mm, depending on node spacing

$\gamma = 0.25$

The penetration of the bead was measured to be 3.0 mm for AKDQ and 3.4 mm for HSLA.

For no lubrication, the drawbead restraining force for HSLA was calculated to be 2100 N per node, while for lubricated conditions it was 1400 N per node. The drawbead restraining force for AKDQ was 1410 N per node without lubrication, while the restraining force for lubricated conditions were 790 N per node.

In addition to the drawbead restraining forces, a force as the result of the contact of the binder on the HSLA was also added. This was calculated in the similar fashion as in the first two sections. The force per node in the HSLA

region for dry conditions was found to be 2400 N per node, while force per node under lubricated conditions was 710 N. These were added all around the HSLA perimeter.

The simulations using these restraining forces calculated using this method resulted in the final weld positions presented in Figures 57 through 60.